University of Alberta

Experiment and Modeling of Passively Q-Switched Ytterbium Doped
Double-Clad Fiber Lasers

by

Lei Pan

A thesis submitted to the Faculty of Graduate Studies and Research
in partial fulfillment of the requirements for the degree of

Doctor of Philosophy

in

Photonics and Plasmas

Department of Electrical & Computer Engineering

Examining Committee

Robert Fedosejevs, Electrical & Computer Engineering

Ying Tsui, Electrical & Computer Engineering

Roger Zemp, Electrical & Computer Engineering

James McMullin, Electrical & Computer Engineering

Frank Hegmann, Physics

Harold Haugen, Engineering Physics, McMaster University

To my parents and my wife Kai
for their endless love and encouragement throughout the years

Abstract

High power passively Q-switched fiber lasers have been demonstrated with different ytterbium doped double-clad fibers by using Cr^{4+}:YAG saturable absorber. With small (5.4 μm) and medium (10 μm) core fibers, single mode outputs have been obtained with pulse energy of tens of μJ, pulse duration of the order of a hundred nanoseconds and pulse-repetition-rate of up to 300 kHz. A theoretical model is developed to predict the laser spectrum and numerically simulate the output characteristics versus pump power. The focused beam in the Cr^{4+}:YAG crystal is assumed to have a Gaussian profile and is analyzed using traveling wave rate equations. The effect of amplified spontaneous emission is also investigated in the simulation, which shows reasonable agreement with experimental observations. With large-mode-area (25 μm) polarization maintaining ytterbium doped fiber, the Q-switched output shows stimulated Brillouin scattering. Linearly polarized output with >300 kW peak power and a pulse duration as short as 490 ps have been obtained. A theoretical model is developed to simulate passive Q-switching with the stimulated Brillouin scattering, which shows good agreement with the experiment.

A high power two-wavelength passively Q-switched Yb doped fiber laser has been achieved with a very simple cavity configuration. Single transverse mode output at 1040 nm and 1070 nm was obtained with tens of μJ pulse energies and hundred nanosecond pulse durations. Modeling of the transient build up of the free-running laser shows the two-wavelength behavior can be attributed to the existence of two gain peaks of Yb-doped fiber under intermediate pump conditions. A theoretical simulation model qualitatively explains

the dynamics of the two-wavelength Q-switching behavior observed in the experiment indicating that longer fibers and higher pump powers favor 1070 nm laser output and reproduces the pulse pattern where two wavelength pulses alternate at an intermediate pump power.

A compact, adjustment free self Q-switched ytterbium doped fiber laser has been demonstrated with fiber ring mirror, in which cooperative Rayleigh-Brillouin scattering was employed as a gain switching mechanism. As short as 600 ps pulses have been obtained at both stimulated Brillouin and Raman frequencies, with peak powers estimated to be up to 26 kW and 5 kW, respectively.

Acknowledgements

It is a great honor that I will complete my PhD study in Laser Physics and Technology at its 50th anniversary. At this time, I would like to thank many people who have made this thesis possible.

I owe a special thank to my parents. As the only child, I study in a place thousands miles away and I have little opportunities staying with them. They have offered me infinite love, support, and understanding.

At last I would like to thank my wife Kai, her coming gives me a warm and happy family in Edmonton.

Table of Contents

List of Figures

List of Tables

List of Symbols

SA	Saturable absorber
DC	Double clad
HR	High reflection
PM	Polarization maintaining
FBG	Fiber Bragg grating
SBS	Stimulated Brillouin scattering
SRS	Stimulated Raman scattering
RS	Rayleigh scattering
XPM	Cross phase modulation
SPM	Self phase modulation
GVD	Group velocity dispersion
LMA	Large mode area
AOM	Acoustic optic modulator
ASE	Amplified spontaneous emission
PMD	Polarization mode dispersion
FWHM	Full width at half maximum
α	Loss coefficient in fiber
NA	Numerical aperture
Γ	Overlap factor in fiber
g_B	Brillouin gain coefficient in fiber
τ_B	Acoustic wave relaxation time in fiber

n	Refractive index
N	Population number in gain medium
N^{sa}	Population number in saturable absorber
τ	Excited state lifetime of gain medium
τ_{sa}	Excited state lifetime of saturable absorber
σ_α	Absorption cross section of gain medium
σ_e	Emission cross section of gain medium
σ_{gsa}	Ground state absorption cross section of saturable absorber
σ_{esa}	Excited state absorption cross section of saturable absorber

Chapter 1

Introduction

1.1 Motivation

Compared with conventional bulk solid-sate lasers, fiber lasers have some intrinsic merits and have seen a tremendous growth in both industrial and research markets. Fiber lasers have excellent thermal properties. Their high surface area to volume ratios allow efficient thermal dissipation and usually they do not need active cooling. In addition, the fiber's waveguiding properties tend to reduce thermal distortion of the beam and achieves superior beam quality. Fiber lasers can be fabricated robustly with long lifetime stability and reliability. The cladding pump scheme has enabled the coupling of higher pump powers into the fiber lasers. High power Q-switched fiber lasers with nanosecond pulse durations are of great interests in applications such as laser micromachining, material processing, nonlinear optics and laser sensing.

Recently there has been considerable interest in studying Yb doped fiber lasers because of their beneficial properties for a number of applications. With a small quantum defect (difference in the energy of the pump photons and the emitted photons), Yb doped fiber lasers are suitable for high power operation with reduced thermal loading. The relatively long upper-state lifetime of Yb

enables more efficient pumping from a given diode pump source and storage of a large amount of energy which is of benefit for Q-switching operation. Many actively and passively Q-switched DC Yb fiber lasers have been reported to date [12–17]. The emission spectrum of Yb is also broad which allows wide wavelength tuning or multi-wavelength lasing. Recently a few multi- or two-wavelength Yb doped fiber lasers have been demonstrated, with different configurations for the wavelength selection and stabilization [18–21].

The use of crystal saturable absorbers (SA) as passive Q-switches is very common and well studied in solid-state lasers. Recently such crystal saturable absorbers have also been applied to fiber lasers. For example, passively Q-switched Er doped fiber lasers using Co^{2+}:ZnSe [22, 23], Er-Yb co-doped fiber lasers using Co^{2+}:ZnS [24], Cr^{2+}:ZnSe [25] or Co^{2+}:MgAl$_2$O$_4$ [25] saturable absorber crystals at an eye safe wavelength of 1.5 μm have been demonstrated. Also Tm doped fiber laser using Co^{2+}:ZnSe [26] near 2 μm and Nd [27] doped fiber lasers using saturable absorber at 1.06 μm have been reported. Compared with active Q-switching, passively Q-switched fiber lasers have the advantages of high efficiency, simplicity, compactness, and potentially lower cost. In addition the passively Q-switched fiber lasers eventually might be possible in a all-fiber design, for example, by splicing Yb double clad fiber to a piece of fiber doped with SA materials such as Cr^{4+}:YAG [28, 29] or Sm [30] doped fiber, and using a fiber Bragg grating as a rear mirror.

Cr^{4+}:YAG is an ideal saturable absorber at 1μm with large absorption cross section, low saturation intensity, high thermal conductivity, high damage threshold and good chemical and photochemical stability. Passively Q-switched Yb doped double-clad fiber lasers with Cr^{4+}:YAG as a saturable absorber (SA) have been intensively studied with varied experimental setup

schemes and output characteristics [15–17]. However no detailed quantitative modeling has been presented before this work for such passively Q-switched fiber lasers to the best of our knowledge. In addition, due to the tight confinement and long interaction length, nonlinear effects can easily occur in pulsed fiber lasers; among which stimulated Brillouin Scattering (SBS) has the lowest threshold for narrow linewidth systems [31]. The SBS process can work like a fast Q-switch and provide strong feedback to the cavity and can generate very short (up to <1 ns) pulses. For Q-switched fiber lasers operating with SBS pulse shortening, while higher peak power can be achieved, the pulse properties are determined by SBS effects rather than the SA; due to the stochastic nature of the SBS process in a fiber, the pulse stability is generally poor. So there is a trade-off between operating with or without SBS, which depends on the specific application requirements: higher output stability or higher output peak power. Therefore, it is interesting and significant to comparatively study both cases with and without using SBS for passively Q-switched Yb doped fiber lasers. In addition, detailed modeling is necessary to understand and optimize the laser operations under the different configurations and regimes.

1.2 Outline

The fundamental background of fiber optics is outlined in chapter 2, which includes four sections: fiber fabrication and losses; fiber modes; fiber dispersion and fiber nonlinearity. In the fiber nonlinearity section, nonlinear refraction and the other two important elastic scattering effects, stimulated Raman scattering (SRS) and stimulated Brillouin scattering (SBS) are discussed.

In chapter 3, the theoretical background of Q-switched lasers is investigated. Rate equations to describe active and passive Q-switched lasers, the

3

characteristics of Yb doped gain medium and Cr^{4+}:YAG saturable absorber are discussed.

Two high power and high repetition rate passively Q-switched Yb doped fiber lasers are demonstrated in chapter 4. A detailed theoretical model is developed to predict the laser spectrum and numerically simulate the output characteristics versus pump power.

A dual-wavelength Yb doped fiber laser is demonstrated in chapter 5. Outputs of the two wavelengths exhibit sustained relaxation oscillation with anti-correlated dynamics. Modeling of the transient build up of the free-running laser shows the two-wavelength behavior can be attributed to the existence of two gain peaks of Yb-doped fiber under intermediate pump conditions.

Chapter 6 reports a high power dual-wavelength passively Q-switched ytterbium doped fiber laser with a Cr^{4+}:YAG saturable absorber. Two-wavelength Q-switched pulses are generated directly from the cladding pumped Yb doped fiber laser. A theoretical model is developed to simulate the two-wavelength Q-switching dynamics, which could explain the experimental observations qualitatively.

Chapter 7 reports a high peak power passively Q-switched ytterbium doped fiber laser with SBS. Sub-nanosecond pulses with peak power of $\sim$375 kW have been obtained. A theoretical model is developed to simulate passive Q-switching together with SBS.

In chapter 8, the cooperative Rayleigh-Brillouin scattering as passive Q-switching mechanism was investigated. A self-Q switched Yb fiber laser was realized by using a fiber loop as a cavity mirror. Nanosecond to subnanosecond outputs have been observed at both ends of the laser cavity with a pulse repetition rate up to 22 kHz. Since the fiber is relatively long, significant SBS

4

output is further transferred to Raman frequencies. Raman pulses as short as 600 ps have been generated with peak power up to a few kW.

Chapter 9 is the summary of the whole thesis. The remaining issues that might be interesting for future investigation are also discussed.

Chapter 2

Fundamentals of fiber lasers

2.1 Fiber fabrication and losses

Total internal reflection is the basic phenomenon responsible for guiding of light in optical fibers, which has been known since the nineteenth century. In its simplest form, an optical fiber consists of a central glass core surrounded by a cladding layer whose refractive index n_2 is slightly lower than the core index n_1. Such fibers are generally referred to as step-index fibers to distinguish them from graded index fibers, in which the refractive index of the core decreases gradually from center to core boundary. Figure 2.1 schematically shows the cross section of a step-index fiber. Two important fiber parameters are fiber numerical aperture NA and fiber V number which are defined by

$$NA = (n_1^2 - n_2^2)^{1/2} \approx n_1(2\Delta)^{1/2} \tag{2.1}$$

$$V = ak_0 NA \tag{2.2}$$

where $\Delta = (n_1 - n_2)/n_1$, is the fractional refractive index change and $k_0 = 2\pi/\lambda_0$, a is the core radius, λ_0 is the wavelength of light. $\theta_a = sin^{-1}NA$ is the acceptance angle of the fiber. The V parameter determines the number of modes supported by the fiber. A step-index fiber supports a single mode if V < 2.405, which will be discussed in Section 2.2.
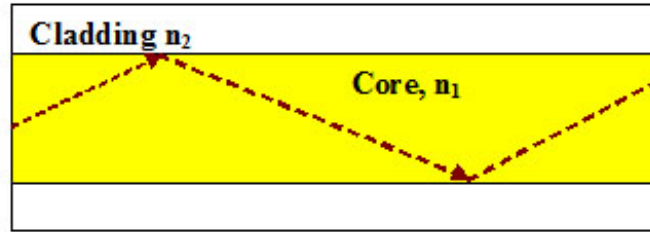
Figure 2.1: Cross section and refractive-index profile of a step-index fiber.

The material of choice for low-loss optical fibers is pure silica glass synthe-sized by fusing SiO_2 molecules. The refractive-index difference between the core and the cladding is realized by the selective use of dopants during the fabrication process. Dopants such as GeO_2 and P_2O_5 increase the refractive index of pure silica and are suitable for the core, while materials such as boron and fluorine are used for the cladding because they decrease the refractive in-dex of silica. The fabrication of optical fibers involves two stages. In the first stage, a vapor deposition method is used to make a cylindrical preform with the desired refractive index profile and the relative core-cladding dimensions. A typical preform is 1-m long with a 2-cm diameter. Several methods can be used for making a preform. The three commonly used methods are modified chemical vapor deposition (MCVD), outside vapor deposition and vapor-phase axial deposition. In the second stage, the preform is drawn into a fiber us-ing a precision-feed mechanism that feeds it into a furnace at a proper speed. During this process, the relative core-cladding dimensions are preserved.

Two dominant factors causing losses in optical fiber are material absorp-tion and Rayleigh scattering. Other factors that may contribute to losses are bending of fiber and scattering of light at the core-cladding interface. The loss in fiber can be described by equation

$$P_T = P_0 e^{(-\alpha L)} \tag{2.3}$$

7
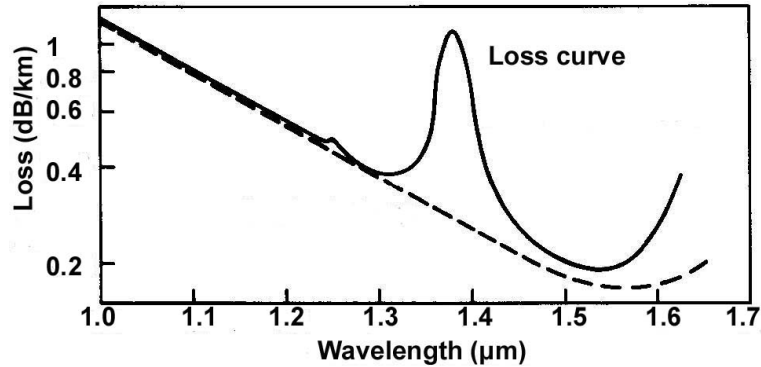
Figure 2.2: Measured loss spectrum of a single-mode silica fiber. Dashed curve shows the contribution resulting from Rayleigh scattering [1,2].

where P_0 is the power launched at the input of a fiber of length L, P_T the transmitted power, and α is the the attenuation constant. α is a measure of total fiber losses from all sources. α can be expressed in units of dB/km using the relation:

$$\alpha_{dB} = -\frac{10}{L} log \frac{P_T}{P_0} = 4.343\alpha \qquad (2.4)$$

Fiber losses depend on the wavelength of light. Figure 2.2 shows the loss spectrum of a silica fiber made by the MCVD process. This fiber exhibits a minimum loss of about 0.2 dB/km near 1.55μm. Losses are considerably higher at shorter wavelengths, reaching a level of a few dB/km in the visible region.

The fiber absorption loss is due to impurities and even a relatively small amount of impurity can lead to significant absorption. The most important impurity affecting fiber loss is the OH ion, which has a fundamental vibrational absorption peak at $\approx 2.73\mu$m. The OH-absorption peak is responsible for the dominant peak seen near 1.4 μm and a smaller peak near 1.23 μm. The OH-ion level can be reduced to less than one part in one hundred million by special precautions taken during the fiber-fabrication process. Rayleigh scattering is

8

a fundamental loss mechanism arising from density fluctuations frozen into the fused silica during manufacturing. The induced local fluctuations in the refractive index scatter light in all directions. The Rayleigh-scattering loss varies as λ^{-4} and is dominant at short wavelengths. Rayleigh loss is intrinsic to the fiber and sets the ultimate limit on fiber loss.

2.2 Fiber modes

Each of the components of the electric and magnetic fields must satisfy the Helmholtz equation

$$\nabla^2 U + n^2 k_0^2 U = 0 \tag{2.5}$$

In a cylindrical coordinate system the Helmholtz equation is

$$\frac{\partial^2 U}{\partial r^2} + \frac{\partial U}{r \partial r} + \frac{\partial^2 U}{r^2 \partial \phi^2} + \frac{\partial^2 U}{\partial z^2} + n^2 k_0^2 U = 0 \tag{2.6}$$

where the complex amplitude U=U(r,ϕ,z) represents any of the Cartesian components of the electric or magnetic fields or axial components. By using the method of separation of variables and substituting

$$U(r, \phi, z) = u(r) e^{-jl\phi} e^{-j\beta z} \quad l = 0, \pm 1, \pm 2, \cdots\cdots \tag{2.7}$$

into Equation 2.6, an ordinary differential equation for u(r) is obtained

$$\frac{d^2 u}{dr^2} + \frac{du}{rdr} + (n^2 k_0^2 - \beta^2 - \frac{l^2}{r^2})u = 0 \tag{2.8}$$

The wave is guided if the propagation constant is smaller than the wavenumber in the core ($\beta < n_1 k_0$) and greater than the wavenumber in the cladding ($\beta > n_2 k_0$). It is convenient to define

$$k_t^2 = n_1^2 k_0^2 - \beta^2 \tag{2.9}$$

$$\gamma^2 = \beta^2 - n_2^2 k_0^2 \tag{2.10}$$

The equation may then be written in the core and cladding separately

$$\frac{d^2u}{dr^2} + \frac{du}{rdr} + (k_t^2 - \frac{l^2}{r^2})u = 0 \tag{2.11}$$

$$\frac{d^2u}{dr^2} + \frac{du}{rdr} - (\gamma^2 + \frac{l^2}{r^2})u = 0 \tag{2.12}$$

The above equations have the solutions of family of Bessel functions as follows

$$u(r) = \begin{cases} J_l(k_T, r) & r < a \quad (core) \\ K_l(\gamma, r) & r < a \quad (cladding) \end{cases} \tag{2.13}$$

where $J_l(x)$ is the Bessel function of the first kind with order l, and $k_l(x)$ is the modified Bessel function of the second kind an order l. The function $J_l(x)$ oscillates like the sine or cosine functions but with decaying amplitude. The parameters k_T and γ determine the rate of change of u(r) in the core and in the cladding, respectively. A large value of k_T means faster oscillation of the radial distribution in the core. A large value of γ indicates faster decay and smaller penetration of the wave into the cladding. The sum of the squares of k_T and γ is a constant

$$k_T^2 + \gamma^2 = (n_1^2 - n_2^2)k_0^2 = NA^2k_0^2 = \frac{V^2}{a^2} \tag{2.14}$$

So that as k_T increases, γ decreases and the field penetrates deeper into the cladding. If k_T exceeds V/a, γ becomes imaginary and the wave ceases to be bound to the core. If we define $X = k_T a, Y = \gamma a$, the equation 2.14 simplifies to

$$X^2 + Y^2 = V^2 \tag{2.15}$$

The condition to determine the propagation constant of fiber modes is called the characteristic equation. By using the normalized parameters $X = k_T a, Y = \gamma a$, the characteristic equation can be simplified to

$$X\frac{J_{l\pm1}(X)}{J_l(X)} = \pm Y\frac{K_{l\pm1}(Y)}{K_l(Y)} \tag{2.16}$$
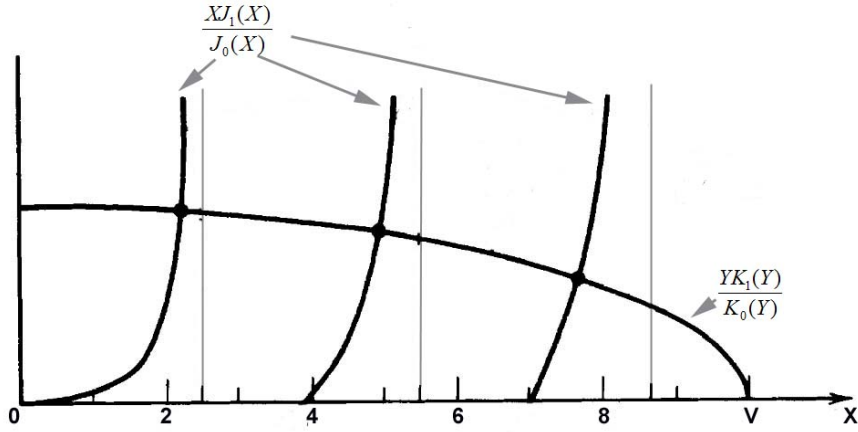
Figure 2.3: Graphical construction for solving the characteristic equation $l=0$, $V=10$ [3].

For each azimuthal l, the characteristic equation has multiple solutions yielding discrete propagation constants $\beta_{lm}, m = 1, 2, ...$, each solution representing a mode. $l = 0$ corresponds to meridional rays. The characteristic equation can be solved by plotting the right and left hand sides versus X and finding the intersections, as shown in Figure 2.3 for $l=0$, $V=10$. It is evident from the figure that when V increases, the number of intersections increases since the right hand side moves to the right as V increases. The number of modes M_l is equal to the number of roots of $J_{l-1}(X)$ that are smaller than V. When $V < 2.405$, all modes except for the fundamental LP_{01} mode are cut off.

Table 2.1 shows some of the roots values. For fiber lasers with large V parameters, the number of modes can be estimated by

$$M \approx \frac{4}{\pi^2}V^2 \tag{2.17}$$

The propagation constant with large V number can be approximated by

$$\beta_{lm} \approx n_1 k_0[1 - \frac{(l + 2m)^2}{M}\Delta] \tag{2.18}$$

11

in which $l = 0, 1, \cdots, M^{1/2}, m = 1, 2, \cdots (M^{1/2} - l))$.

Table 2.1: Cutoff parameter for LP_{0m} and LP_{1m} modes

l m :	1	2	3
0	0	3.832	7.016
1	2.405	5.520	8.654

For a single mode fiber, the effective mode radius ω_s can be expressed as

$$\omega_s = a(0.65 + 1.619 V^{-1.5} + 2.876 V^{-6}) \tag{2.19}$$

The overlap factor between the fiber core and signal is

$$\Gamma_s = 1 - exp(\frac{-2a^2}{\omega_s^2}) \tag{2.20}$$

2.3 Fiber dispersion

When a short pulse of light travels through an optical fiber its power is dispersed in time so that the pulse spreads into a wider time interval. There are various different types of dispersion, which includes chromatic dispersion, intermodal dispersion and polarization mode dispersion.

2.3.1 Chromatic dispersion

When an electromagnetic wave interacts with the bound electrons of a dielectric, the medium response depends on the optical frequency ω, which is referred to as chromatic dispersion. When the optical frequency is far from the medium resonances, the refractive index is well approximated by the Sellmeier equation

$$n^2(\omega) = 1 + \sum_{j=1}^{q} \frac{B_j \omega_j^2}{\omega_j^2 - \omega^2} \tag{2.21}$$
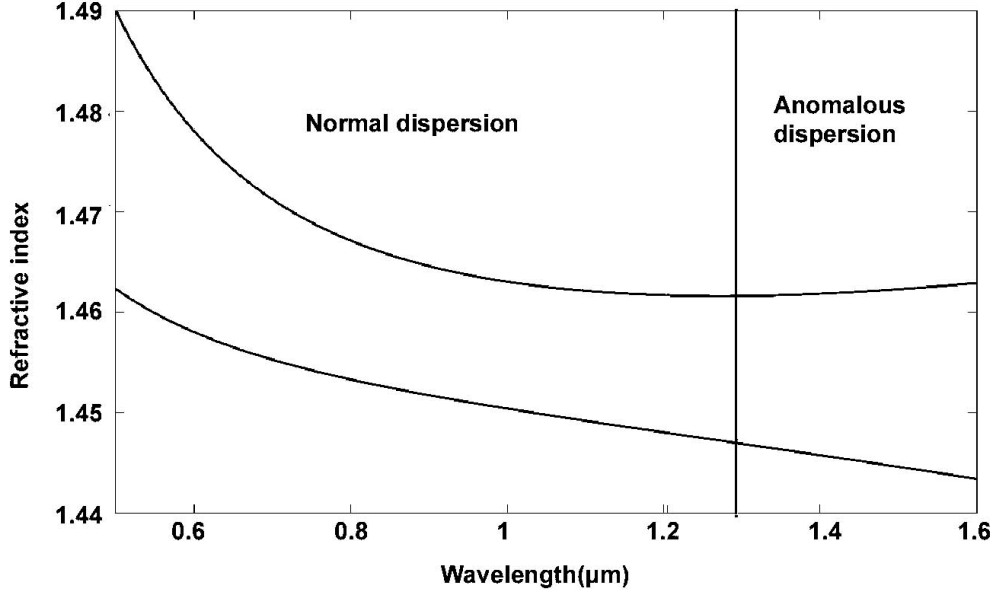
Figure 2.4: Variation of refractive index n and group index n_g with wavelength for fused silica; the dashed line marks the zero group velocity dispersion wavelength [1].

where ω_j is the resonance frequency and B_j is the strength of j_{th} resonance. The sum in the above equation extends over all material resonances that contribute to the frequency range of interest. In the case of optical fibers, the parameters B_j and ω_j are obtained experimentally by fitting the measured dispersion curves to the above equation with $q = 3$ and depend on the core constituents. For bulk-fused silica, these parameters are found to be B_1=0.6961663, B_2=0.4079426, B_3=0.8974794, λ_1=0.0684043 μm, λ_2=0.1162414 μm, and λ_3=9.896161 μm, where $\lambda_j = 2\pi c/\omega_j$ and c is the speed of light in vacuum. Figure 2.4 displays how n varies with wavelength for fused silica.

Chromatic dispersion can be described by expanding the mode-propagation constant β in a Taylor series about the frequency ω_0 at which the pulse spectrum is centered

$$\beta(\omega) = n(\omega)\frac{\omega}{c} = \beta_0 + \beta_1(\omega - \omega_0) + \frac{1}{2}\beta_2(\omega - \omega_0)^2 + ..., \qquad (2.22)$$

13

where

$$\beta_m = (\frac{d^m\beta}{d\omega^m})_{\omega=\omega_0} \tag{2.23}$$

The parameters β_1 and β_2 are related to the refractive index $n(\omega)$ and its derivatives through the relations

$$\beta_1 = \frac{1}{v_g} = \frac{n_g}{c} = \frac{1}{c}(n + \omega\frac{dn}{d\omega}) \tag{2.24}$$

$$\beta_2 = \frac{1}{c}(2\frac{dn}{d\omega} + \omega\frac{d^2n}{d\omega^2}) \tag{2.25}$$

where n_g is the group index and v_g is the group velocity. The envelope of an optical pulse moves at the group velocity; and the parameter β_2 represents dispersion of the group velocity and is responsible for pulse broadening, which is known as the group-velocity dispersion (GVD), and β_2 is the GVD parameter. The dispersion parameter D is defined as

$$D = \frac{d\beta_1}{d\lambda} = -\frac{2\pi c}{\lambda^2}\beta_2 = \frac{\lambda}{c}\frac{d^2n}{d\lambda^2} \tag{2.26}$$

A walk-off parameter d_{12} for two pulses transmitted in fiber is defined as

$$d_{12} = \beta_1(\lambda_1) - \beta_1(\lambda_2) = v_g^{-1}(\lambda_1) - v_g^{-1}(\lambda_2) \tag{2.27}$$

where λ_1 and λ_2 are the center wavelengths of the two pulses.

Figure 2.5 shows how β_2 and D vary with wavelength λ for fused silica. As can be seen in the figure that both β_2 and D vanish at a wavelength of 1.27μm and change sign for longer wavelengths. This wavelength is referred to as the zero-dispersion wavelength (λ_D). However, the dispersive effects do not disappear completely at $\lambda = \lambda_D$ due to the third-order dispersion (TOD) coefficient β_3, which can distort ultrashort optical pulses both in the linear and nonlinear regimes. Therefore inclusion of third-order dispersion is necessary
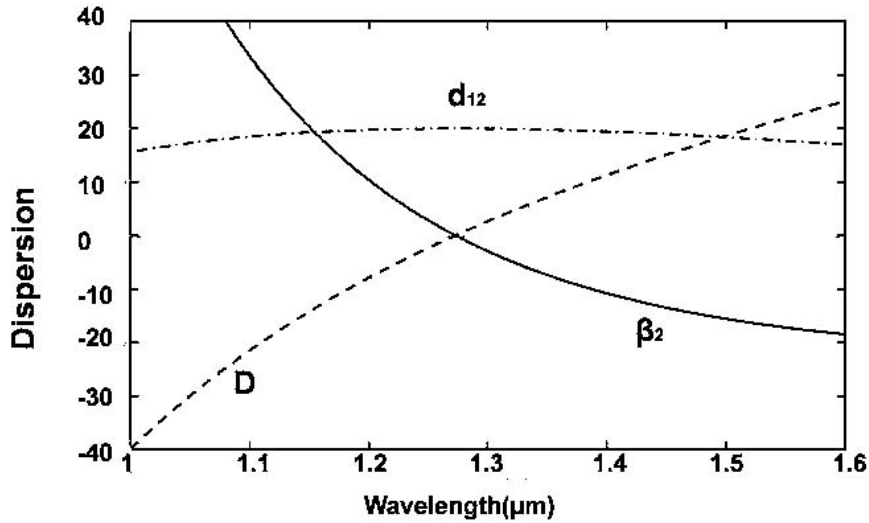
Figure 2.5: Variation of $\beta_2(ps^2/km)$ and $D[ps/(km.nm)]$ as a function of wavelength and $d_{12}(ps/m)$ for a wavelength of λ_2 of $0.8\mu m$ and λ_1 as plotted for fused silica [1].

for ultrashort optical pulses, or when the input wavelength λ approaches λ_D to within a few nanometers.

The discussion above is based on the assumption of plane waves. In practice, deviations from this situation can occur due to dielectric waveguiding, in which the effective mode index is slightly lower than the material index of the core. This results in a waveguide contribution that must be added to the material contribution to obtain the total dispersion. In general, the waveguide contribution to β_2 is relatively small except near the zero-dispersion wavelength λ_D where the two become comparable. The main effect of the waveguide contribution is to shift λ_D slightly toward longer wavelengths; $\lambda_D \approx 1.31\mu m$ for standard fibers.

The contribution of waveguide dispersion to D (or β_2) depends on fiber parameters such as core diameter a and core-cladding index difference. This feature can be used to shift the zero-dispersion wavelength λ_D to around 1.55

15
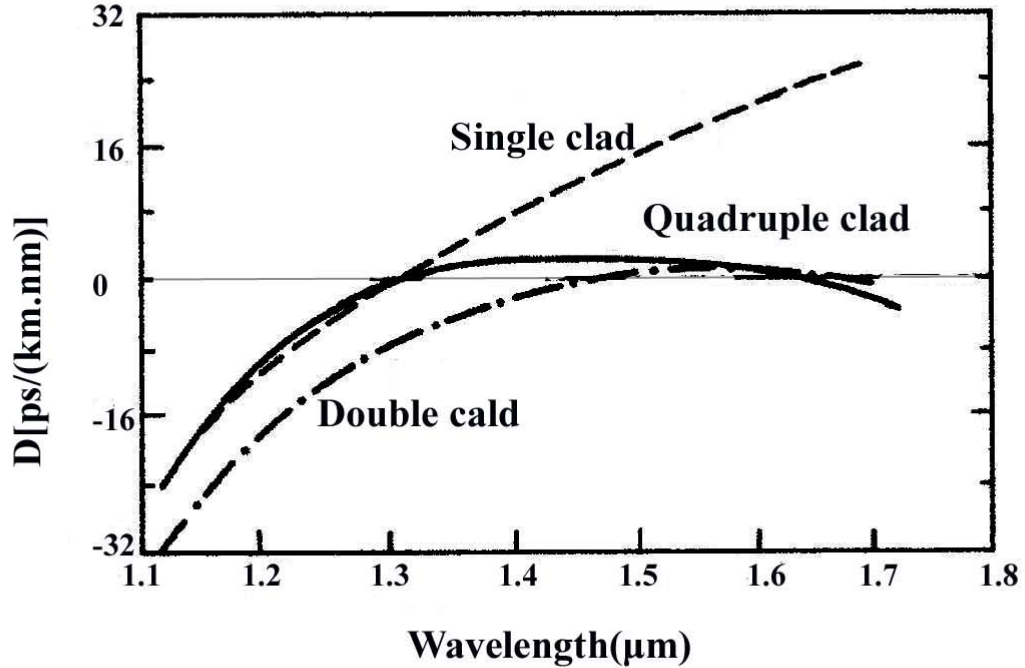
Figure 2.6: Variation of dispersion parameter D with wavelength for three kinds of fibers [4].

μm where the fiber loss is minimum, which is called dispersion-shifted fiber. It is also possible to design dispersion-flattened fibers with low dispersion over a relatively large wavelength range of 1.3-1.6 μm by using multiple cladding layers. Figure 2.6 shows the measured dispersion spectra for two multiple-clad fibers with two and four cladding layers around the core. The dispersion of a single-clad fiber is also shown by a dashed line for comparison.

2.3.2 Intermodal and polarization mode dispersion

When light propagates in a multimode fiber, the dispersion depends not only on the optical frequency but also on the propagation mode involved. If v_{min} and v_{max} are the smallest and largest group velocities, the transmitted pulse spreads in time after propagation over a fiber length of L by $L/v_{min} - L/v_{max}$. Since the modes are generally not excited equally, the overall shape of the pulse

16

after the fiber is a smooth profile. The overall root-mean-square (rms) pulse width is estimated as $\sigma_\tau = \frac{1}{2}(L/v_{min} - L/v_{max})$. This width represents the response time of the fiber. In a step-index fiber with large number of modes, $v_{min} \approx c_1(1 - \Delta)$ and $v_{max} \approx c_1$. With $(1 - \Delta)^{-1} \approx 1 + \Delta$, the response time is

$$\sigma_\tau \approx \frac{L}{c_1}\frac{\Delta}{2} \tag{2.28}$$

where $\Delta = (n_1 - n_2)/n_1$ and it is a fraction of $\Delta/2$ of the delay time L/c_1.

In single mode fibers, the dispersion can happen between two degenerate modes with orthogonal polarizations. In real fibers, there is small deviation from cylindrical symmetry because of random variations in core shape and stress induced anisotropy, which result in mixing of the two polarization states by breaking the mode degeneracy. The mode propagation constant β becomes slightly different for the modes polarized in the x and y directions. If an input pulse excites both polarization components, the two components travel along the fiber at different speeds because of their different group velocities. The pulse becomes broader at the output end because group velocities change randomly due to the random changes in fiber birefringence, which is referred as polarization-mode dispersion (PMD). The strength of modal birefringence is defined as

$$B_m = \frac{|\beta_x - \beta_y|}{k_0} = |n_x - n_y| \tag{2.29}$$

where n_x and n_y are the modal refractive indices for the two orthogonally polarized states. The beat length L_B is defined as

$$L_B = \frac{2\pi}{|\beta_x - \beta_y|} = \frac{\lambda}{B_m} \tag{2.30}$$

The pulse broadening can be estimated from the time delay ΔT arising from the two polarization components after propagation through a fiber. For

a fiber of length L and constant birefringence B_m

$$\Delta T = |\frac{L}{v_{gx}} - \frac{L}{v_{gy}}| = L|\beta_{1x} - \beta_{1y}| = L(\Delta\beta_1) \qquad (2.31)$$

where $\Delta\beta_1$ is related to group-velocity mismatch. In fact, PMD is characterized by the rms value of ΔT obtained after averaging over random perturbations. The variance of ΔT is found to be

$$\sigma^2{}_T = \langle(\Delta T)^2\rangle = 2(\beta_1 l_c)^2[exp(-L/l_c) + L/l_c - 1] \qquad (2.32)$$

where $\beta_1 \equiv \Delta\tau/L$, $\Delta\tau$ is the differential group delay for the principal states of polarization, and l_c is the correlation length over which two polarization components remain correlated; typical values of l_c are of the order of 10 m. For $L > 0.1$ km, we can use $l_c \ll L$ to find that

$$\sigma_T \approx \Delta\beta_1\sqrt{2l_c L} \equiv D_p\sqrt{L} \qquad (2.33)$$

where D_p is the PMD parameter. For most fibers, values of D_p are in the range of 0.1 to 1 ps/$\sqrt{km}$. Because of its $\sqrt{L}$ dependence, PMD-induced pulse broadening is relatively small compared with the GVD effects. However, PMD becomes significant for high-speed communication systems designed to operate over long distances near the zero-dispersion wavelength of the fiber.

To avoid this difficulty, polarization-maintaining fibers can be employed, in which a large amount of birefringence is introduced to these fibers through design modifications. Therefore, their relatively small birefringence fluctuations are masked and do not affect the state of polarization significantly. One scheme is stress-induced birefringence which permits $B_m \sim 10^{-4}$. For example, two rods of borosilicate glass can be inserted to the opposite sides of the fiber core at the preform stage. The resulting birefringence depends on the location and the thickness of the stress-inducing elements. Figure 5 in reference [32] shows

how B_m varies with thickness d for different shapes of stress-inducing elements located at a distance of five times the core radius. Values of $B_m \sim 2 \times 10^{-4}$ can be realized for d in the range of 50-60 μm. Such fibers are often named after the shape of the stress-inducing element like "panda" or "bow-tie fiber". Before an optical signal can be launched into the fiber, the slow and fast axes of polarization-maintaining fibers should be identified. When the polarization direction of the linearly polarized light coincides with the slow or the fast axis, the state of polarization remains unchanged during propagation. However, if the polarization direction makes an angle with these axes, polarization changes continuously along the fiber in a periodic manner with a period equal to the beat length.

2.4   Fiber nonlinearity

Like any other dielectrics, the response of optical fibers to electromagnetic fields becomes nonlinear for light with high intensity. The origin of nonlinear response is related to anharmonic motion of bound electrons under the influence of an electromagnetic field. As a result, the total polarization P induced by electric dipoles is not linear with the electric field E, but satisfies the more general relation

$$P = \varepsilon_0(\chi^{(1)} \cdot E + \chi^{(2)} : EE + \chi^{(3)} \vdots EEE + ...) \tag{2.34}$$

where ε_0 is the vacuum permittivity and $\chi^{(j)}$ is j_{th} order susceptibility. In general, $\chi^{(j)}$ is a tensor of rank j+1. The linear susceptibility $\chi^{(1)}$ represents the dominant contribution to P. Its effects are included through the refractive index n and the attenuation coefficient α. The second-order susceptibility $\chi^{(2)}$ is responsible for nonlinear effects such as second-harmonic generation

and sum-frequency generation. However, as SiO_2 is a symmetric molecule, $\chi^{(2)}$ vanishes for silica glasses. Therefore, optical fibers usually do not exhibit second-order nonlinear effects. The lowest-order nonlinear effects in optical fibers originate from the third-order susceptibility $\chi^{(3)}$, which is responsible for third-harmonic generation, four-wave mixing, and nonlinear refraction.

The nonlinear effects governed by $\chi^{(3)}$ are elastic, in which no energy is exchanged between the electromagnetic field and the dielectric medium. A second class of nonlinear effect is stimulated inelastic scattering in which the optical field transfers part of its energy to the nonlinear medium. Stimulated Raman scattering (SRS) and stimulated Brillouin scattering (SBS) are two important inelastic nonlinear effects in optical fibers. Both of them are related to vibrational excitation modes of silica. The main difference between the two is that optical phonons participate in SRS while acoustic phonons participate in SBS.

2.4.1   Nonlinear refraction

Nonlinear refraction in a fiber is a phenomenon based on the intensity dependence of the refractive index. The nonlinear refractive index can be written

$$n = n_0 + n_2 \frac{|E|^2}{2} \tag{2.35}$$

where n_0 is the linear part of refractive index, E is the electric field amplitude. n_2 is the nonlinear-index coefficient related to $\chi^{(3)}$ by the relation

$$n_2 = \frac{3}{4n_0} Re(\chi^{(3)}) \tag{2.36}$$

where Re stands for the real part and the optical field is assumed to be linearly polarized so that only one component of the fourth-rank tensor contributes to the refractive index. $\chi^{(3)}$ is elastic in the sense that no energy is exchanged

between the electromagnetic field and the dielectric medium. The two best known effects induced by nonlinear refraction are self-phase modulation (SPM) and cross-phase modulation (XPM). XPM occurs because the effective refractive index seen by an optical beam in a nonlinear medium depends not only on the intensity of that beam but also on the intensity of other copropagating beams. SPM refers to the self-induced phase shift experienced by an optical field during its propagation in fibers. The intensity-dependent nonlinear phase shift

$$\phi_{NL} = n_2 k_0 |E|^2 L \tag{2.37}$$

where $k_0 = 2\pi/\lambda$ and L is the fiber length. SPM is responsible for spectral broadening of ultrashort pulses and formation of optical solitons in the anomalous-dispersion regime of fibers. The maximum phase shift ϕ_{max} occurs at the pulse center

$$\phi_{max} = L_{eff}/L_{NL} = \gamma_{NL} P_0 L_{eff} \tag{2.38}$$

where L_{eff} is the effective fiber length related to fiber loss α as

$$L_{eff} = [1 - exp(-\alpha L)]/\alpha \tag{2.39}$$

P_0 is the peak power and γ is related to the nonlinear-index coefficient n_2 by

$$\gamma(\omega_0) = \frac{n_2(\omega_0)}{c A_{eff}} \tag{2.40}$$

To simplify the expression, a normalized field amplitude $U(z,t)$ is defined by the expression

$$A(z,t) = \sqrt{P_0} exp(-\alpha z/2) U(z,t) \tag{2.41}$$

where P_0 is the peak power of the incident pulse, $A(z,t)$ is the slowly varying amplitude of the electric field E along z defined as

$$E(r,t) = \frac{1}{2}\hat{x}\{F(x,y)A(z,t)exp[i(\beta_0 z - \omega_0 t)] + c.c.\} \tag{2.42}$$

21

where $F(x, y)$ is the modal distribution.

The nonlinear length L_{NL} is effective propagation distance at which $\phi_{max} = 1$. Spectral changes induced by SPM are a direct consequence of the time dependence of

phi_{NL}. A temporally varying phase implies that the instantaneous optical frequency differs across the pulse from its central value ω_0. The difference $\delta\omega$ is given by

$$\delta\omega(t) = -\frac{\partial\phi_{NL}}{\partial t} = -(\frac{L_{eff}}{L_{NL}})\frac{\partial}{\partial t}|U(0, t)|^2 \qquad (2.43)$$

where $U(0, t)$ is the value of $U(z, t)$ when z=0. The time dependence of $\delta\omega$ is referred to as frequency chirping. New frequency components are generated continuously as the pulse propagates down the fiber, which broaden the spectrum over its initial width at z=0 for initially unchirped pulses. The qualitative features of frequency chirp depend on the pulse shape. Figure 2.7 shows variation of (a) the nonlinear phase shift φ_{NL} and (b) the induced frequency chirp $\delta\omega$ across the pulse at $L_{eff} = L_{NL}$ in the cases of a Gaussian pulse (m=1) and a super-Gaussian pulse (m=3).

2.4.2   Stimulated Raman scattering

Optical fields can transfer a small fraction (typically $\sim 10^{-6}$) of power to any molecular medium by spontaneous Raman scattering. Its frequency is downshifted by an amount determined by the vibrational modes of the medium and is called the Stokes wave. For intense optical pump fields, the Stokes wave can be amplified by the optical radiation and can grow rapidly inside the medium and most of the pump energy can transfer to it. The Raman gain coefficient g_R depends on the composition of the fiber core, as well as the relative polarization states of the pump and Stokes waves. Due to the

22
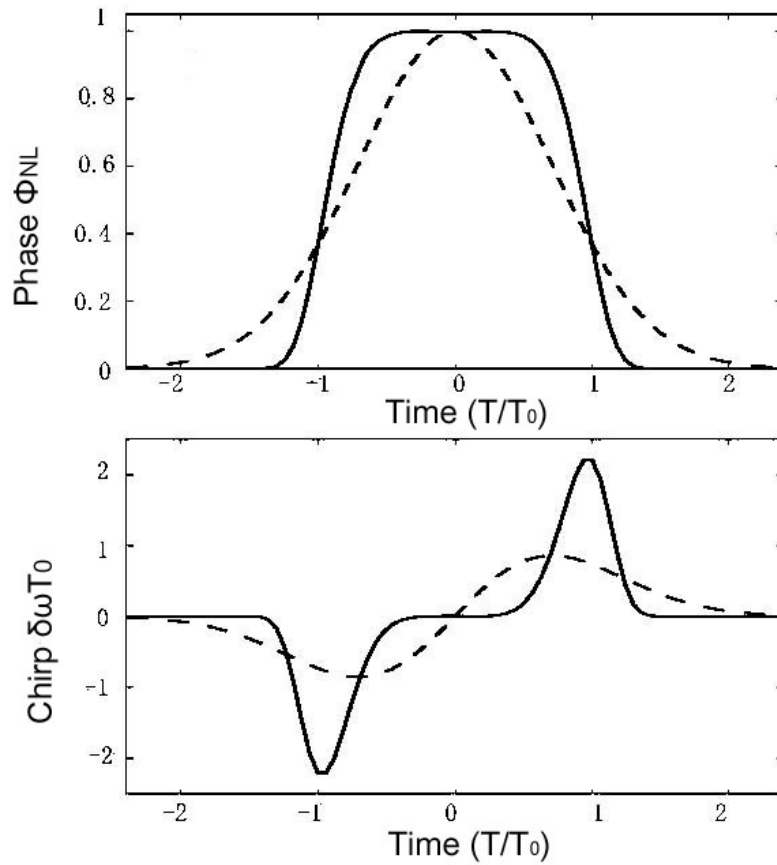
Figure 2.7: Temporal variation of SPM-induced (a) phase shift φ_{NL} and (b) frequency chirp $\delta\omega$ for Gaussian (dashed curve) and super-Gaussian (solid curve) pulses. In this case, the phase change is directly proportional to the intensity so that the pulse intensity has the same shape as the phase shift [1].

23
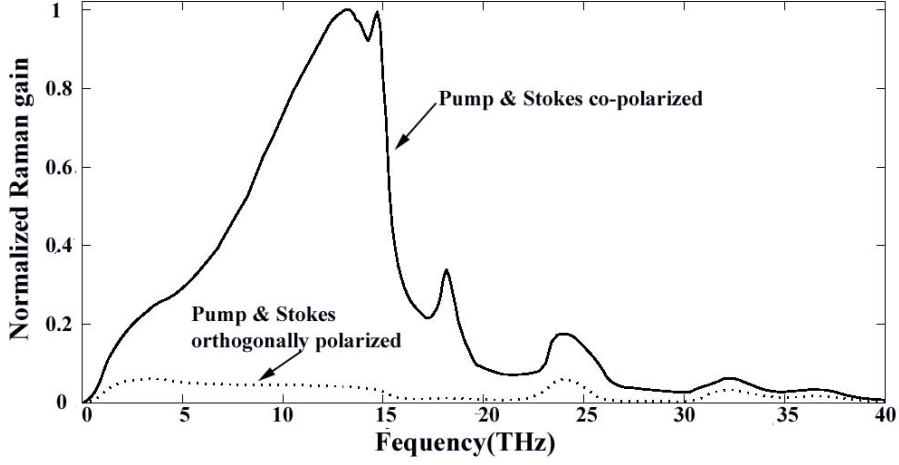
Figure 2.8: Normalized Raman gain for fused silica [1, 5].

noncrystalline nature of silica glass, the Raman gain in silica fibers covers a large frequency range (up to 40 THz) with a broad peak located near 13 THz, as shown in Figure 2.8. In amorphous materials such as fused silica, molecular vibrational frequencies spread out into bands that overlap and create a continuum. Because of this feature, optical fibers can act as broadband Raman amplifiers.

For the CW pump case, the SRS process can be described by two coupled equations:

$$\frac{dI_s}{dz} = g_R I_p I_s - \alpha_s I_s \tag{2.44}$$

$$\frac{dI_p}{dz} = -\frac{\omega_p}{\omega_s} g_R I_p I_p - \alpha_s I_p \tag{2.45}$$

where α_s and α_p account for fiber losses at the Stokes and pump frequencies, respectively. The Raman threshold is defined as the input pump power at which the Stokes power becomes equal to the pump power at the fiber output [33]. If we neglect the pump depletion, critical pump power for forward SRS is:

$$P_0^{CR} \approx \frac{16 A_{eff}}{g_R L_{eff}} \tag{2.46}$$

24

where A_{eff} is the effective core area of fiber and L_{eff} is the effective interaction length defined by:

$$L_{eff} = [1 - e^{-\alpha_p L}]/\alpha_p \qquad (2.47)$$

For backward SRS, the numerical factor 16 in Eq. 2.46 is replaced with 20.

The CW theory of SRS needs to be modified when SRS occurs with pulsed pumping. To simplify the dynamical equation, the medium has been assumed to respond instantaneously. The coupled amplitude equations including Raman gain, pump depletion, SPM, XPM as well as group velocity dispersion (GVD)are given by [1]

$$\frac{\partial A_p}{\partial z} + \frac{1}{v_{gp}}\frac{\partial A_p}{\partial t} + \frac{i\beta_{2p}}{2}\frac{\partial^2 A_p}{\partial t^2} + \frac{\alpha}{2}A_p = i\gamma_p(|A_p|^2 + (2-f_R)|A_s|^2)A_p - \frac{g_p}{2}|A_s|^2)A_p$$
$$(2.48)$$

$$\frac{\partial A_s}{\partial z} + \frac{1}{v_{gs}}\frac{\partial A_s}{\partial t} + \frac{i\beta_{2s}}{2}\frac{\partial^2 A_s}{\partial t^2} + \frac{\alpha}{2}A_s = i\gamma_s(|A_s|^2 + (2-f_R)|A_p|^2)A_s - \frac{g_s}{2}|A_p|^2)A_s$$
$$(2.49)$$

where v_{gj} is the group velocity, β_{2j} is the GVD coefficient, and γ_{NLj} is the nonlinear parameter and $(2 - f_R)$ is the XPM factor.

2.4.3 Stimulated Brillouin scattering

Compared with SRS, the stimulated Brillouin scattered (SBS) Stokes wave propagates only backwards when SBS occurs in a single-mode optical fiber. In narrow linewidth optical fiber lasers, SBS can occur at input power levels much lower than those needed for SRS. In a classical view, the process of SBS is a nonlinear interaction between the pump and Stokes fields through an acoustic wave. The pump field generates an acoustic wave through the process of electrostriction. The acoustic wave could in turn modulate the refractive index of the medium. In a quantum mechanical view, the scattering process

is an annihilation of a pump photon and creation of a Stokes photon and an acoustic phonon simultaneously. In the process, both the energy and the momentum should be conserved; the frequencies and the wave vectors of the three waves are related by

$$\Omega_B = \omega_p - \omega_s \qquad (2.50)$$

$$k_B = k_p - k_s \qquad (2.51)$$

where ω_p, ω_s and ω_B are the frequencies, and k_p, k_s and k_B are the wave vectors, of the pump, Stokes and acoustic waves, respectively. The Brillouin shift given by:

$$\Omega_B = v_B|k_B| \approx 2v_B|k_p|sin(\theta/2) \qquad (2.52)$$

where v_B is the speed of acoustic wave in fiber and θ is the angle between the pump and Stokes fields. In a single-mode optical fiber, SBS occurs only in the backward direction with the Brillouin shift given by

$$\nu_B = \Omega_B/2\pi = 2n_p v_B/\lambda_p \qquad (2.53)$$

where n_p is the effective mode index at the pump wavelength in vacuum λ_p. If we use $v_B = 5.96$ km/s and $n_p = 1.45$, silica fibers, $\nu_B \approx 16.3$ GHz at $\lambda_p = 1.06\mu m$. The SBS gain spectrum $[g_B(\Omega)]$ is very narrow ($\sim$10 MHz). When acoustic waves decay as $exp(-\Gamma_B t)$, the Brillouin gain has a Lorentzian spectrum of the form

$$g_B(\Omega) = \frac{g_p(\Gamma_B/2)^2}{(\Omega - \Omega_B)^2 + (\Gamma_B/2)^2} \qquad (2.54)$$

g_p is the the peak value of the Brillouin gain at $\Omega = \Omega_B$ which is given by

$$g_p \equiv g_B(\Omega_B) = \frac{8\pi^2\gamma_e^2}{n_p\lambda_p\rho_0 cv_A\Gamma_B} \qquad (2.55)$$

26
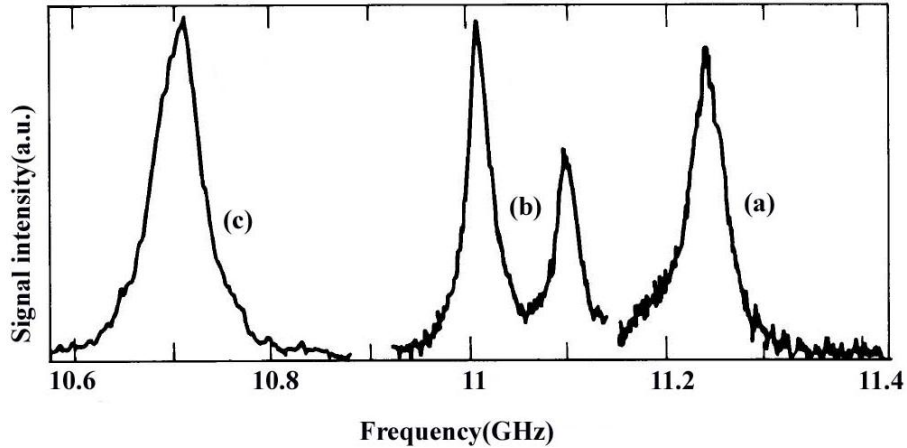
Figure 2.9: Brillouin gain spectra of three fibers for λ_p=1.525 μm: (a) silica-core fiber, (b) depressed-cladding fiber, and (c) dispersion-shifted fiber [6].

where $\gamma_e \approx 0.902$ (unitless) is the electrostrictive constant of silica and $\rho_0 \approx 2210 kg/m^3$ is its density. In the case of a pump laser with a Lorentzian spectral profile of width $\Delta\nu_p$, the gain spectrum is still given by Equation 2.54, but the peak value of Brillouin gain is reduced by a factor $1 + \Delta\nu_p/\Delta\nu_p$.

The Brillouin spectrum of silica fibers can be quite different from that of bulk silica due to the mode guiding nature. The Brillouin gain spectrum of a fiber also depends considerably on details of the fiber design and the presence of dopants in the fiber core. Figure 2.9 shows the gain spectra measured for three different fibers having different structures and different doping levels of germania (GeO_2) in their cores. The fiber (b) has a double-peak structure which was believed to be due to the inhomogeneous distribution of $GeO2$ within the core [6]. A three-peak gain spectrum was also observed and interpreted to result from different acoustic velocities in the core and cladding regions of the fiber [34].

Under CW or quasi-CW pump conditions, SBS can be described by two coupled equations similar to Equations 2.44 and 2.45, except that the Stokes

27

wave is counter propagated with respect to the pump wave. Since the value of the Brillouin shift is relatively small, we have assumed that $\omega_p \approx \omega_s, \alpha_p \approx \alpha_s = \alpha$, for the pump and Stokes waves.

$$-\frac{dI_s}{dz} = g_B I_p I_s - \alpha I_s \tag{2.56}$$

$$\frac{dI_p}{dz} = -g_B I_p I_s - \alpha I_p \tag{2.57}$$

By neglecting the pump depletion, the Brillouin threshold is found to occur at a critical pump power of [33]

$$P_0^{cr} = \frac{21 A_{eff}}{g_B(\Omega_B) L_{eff}} \tag{2.58}$$

where L_{eff} is the effective fiber length defined by 2.39, A_{eff} is the effective core area of the fiber. SBS threshold increases by 50% when the state of polarization of the pump field becomes completely scrambled because of birefringent fluctuations. The medium response in the SBS case is governed by the phonon lifetime T_B with a typical value of <10 ns in silica fibers. The quasi-CW regime is valid only for pump pulses of widths 100 ns or more. When the pulse width is of the order of 10 ns, it is necessary to consider the dynamics of the acoustic mode participating in the SBS process. The following set of three coupled amplitude equations are obtained [1]

$$\frac{\partial A_p}{\partial z} + \frac{1}{v_g}\frac{\partial A_p}{\partial t} + \frac{i\beta_2}{2}\frac{\partial^2 A_p}{\partial t^2} + \frac{\alpha}{2}A_p = i\gamma_p(|A_p|^2 + 2|A_s|^2)A_p - \frac{g_B}{2}A_s Q \tag{2.59}$$

$$-\frac{\partial A_s}{\partial z} + \frac{1}{v_g}\frac{\partial A_s}{\partial t} + \frac{i\beta_2}{2}\frac{\partial^2 A_s}{\partial t^2} + \frac{\alpha}{2}A_s = i\gamma_s(|A_s|^2 + 2|A_p|^2)A_s + \frac{g_B}{2}A_p Q \tag{2.60}$$

$$T_B\frac{\partial Q}{\partial t} + (1 + i\delta)Q = A_p A_s \tag{2.61}$$

where the effects of GVD, SPM, and XPM have been included. The material response to acoustic waves is described by Equation 2.61, where Q is related

28

to the amplitude of density oscillations. δ is the detuning parameter defined as $\delta = (\omega_p - \omega_s - \Omega_B)T_B$.

Chapter 3

Background of Q-switched lasers

3.1 Theory of traditional Q-switched lasers

Q-switching is a technique to generate energetic nanosecond pulses from a laser by modulating the cavity losses and thus the Q factor of the laser resonator. The Q-switched process can be described as follows. Initially, the energy stored and the gain in the active medium are high, but the cavity loss is also high, lasing action is prohibited, and the population inversion reaches a level far above the threshold for normal lasing action. Then, the losses are suddenly reduced to a small value, so that the power of the laser radiation builds up very quickly in the resonator, which typically starts with noise from spontaneous emission and then is amplified to macroscopic power levels after multiple resonator round trips. Once the temporally integrated intracavity power has reached the order of the saturation energy of the gain medium, the gain starts to be saturated. The peak of the pulse is reached when the gain reduces to a value equal to the remaining (low) resonator losses. The large intracavity power present at that time leads to further depletion of the stored energy during the period where the output pulse power decays. In many cases, the energy extracted after the pulse maximum is similar to that

before the pulse maximum. The pulse duration achieved with Q-switching is typically in the nanosecond range (corresponding to several cavity round trips), and usually well above the cavity round-trip time.

Q-switching can be realized in either an active or a passive way. Active Q-switching needs an active control element, such as an acousto-optic modulator (AOM), electro-optic modulator (EOM), or a mechanical element like a rotating mirror. The advantage of the active Q-switch is easy control of the pulse repetition rate and pulse width, whereas the disadvantage is the requirement of an optical modulator. For passive Q-switching, the losses are automatically modulated with a saturable absorber (SA). The pulse energy and duration of a passively Q-switched laser are relatively stable, and the pump power can only significantly affect the pulse repetition rate. Compared with active Q-switching, the advantages of the passive Q-switch include simplicity and cost-effectiveness, and suitablity for very high pulse repetition rates.

Numerical modeling with rate equations is important to investigate static and dynamic characteristics of a Q-switched laser and to optimize system configurations. The traditional modeling of Q-switched lasers generally uses the point model which is based on an assumption of a uniform gain along the laser cavity.

3.1.1 Rate equation and optimization for rapidly active Q-switching

In many instances, Q-switches are so fast that no significant change of population inversion takes place during the switching process. The rate equations can be described as [7]

$$\frac{d\phi}{dt} = \frac{\phi}{t_r}[2\sigma_{es}N_2L - ln(1/R) - L'] \tag{3.1}$$

$$\frac{dN_2}{dt} = -\gamma c_0 \sigma_{es} \phi N_2 \tag{3.2}$$

where ϕ is the intracavity photon density, N_2 is the excited state population density of the gain medium, σ_{es} is the emission cross section of the gain medium, L is the length of gain medium; R is the reflectivity of the output coupler, L' is the round trip dissipative loss, γ is the inversion reduction factor (γ=1, 2 for four level and three level systems, respectively); $t_r = 2L_c/c_0$ is the cavity round trip time, where L_c is the cavity optical length, c_0 is the speed of light in vacuum.

The expression for laser output pulse energy is derived as

$$E = \frac{h\upsilon A}{2\sigma_{es}\gamma} ln(\frac{1}{R}) ln(\frac{N_2^i}{N_2^f}) \tag{3.3}$$

where N_2^i and N_2^f are the initial and final the population inversion densities, A is the effective beam area. By the Lagrange multiplier method [35], the optimum reflectivity of the cavity is [7]

$$R_{opt} = exp[L'\frac{lnz + 1 - z}{lnz}] \tag{3.4}$$

where

$$z = \frac{2\sigma_{es}N_2^i L}{L'} = \frac{N_2^i}{N_2^f} \tag{3.5}$$

is the ratio of initial round trip gain of the cavity over the dissipative loss. The maximum output energy under the R_{opt} can be obtained as

$$E_{max} = \frac{Ah\upsilon L'}{2\sigma_{es}\gamma}(z - 1 - lnz) \tag{3.6}$$

The threshold inversion density for optimally coupled Q-switched laser is

$$N_t = \frac{L'}{2\sigma_{es}L}[\frac{z-1}{lnz}] \tag{3.7}$$

The analytic equations for the peak extracavity laser power can be expressed as

$$P_{max} = \frac{Ah\nu L'^2}{2\sigma_{es}\gamma t_r}[\frac{z-1-lnz}{lnz}]\{z - [\frac{z-1}{lnz}][1 + ln(\frac{zlnz}{z-1})]\} \tag{3.8}$$

and the full width at half magnitude (FWHM) pulse duration is

$$t_p = \frac{t_r}{L'}\{[\frac{lnz}{z}][\frac{1}{1 - (\frac{z-1}{lnz})[1 + ln(\frac{zlnz}{z-1})]}]\} \tag{3.9}$$

Figure 3.1 (a) and (b) show the peak power and FWHM pulse width under the optimally coupled condition. The peak power P_{max} is expressed in units of $P_{scale} = h\upsilon AL'^2/2\sigma_{es}\gamma t_r$. The FWHM pulse width is in units of t_r/L'.

3.1.2 Modeling of passively Q-switched lasers

A saturable absorber (SA) is usually employed in passive Q-switches. A saturable absorber is an optical component with a certain optical loss, which is reduced at high optical intensities. This can be a medium with absorbing dopant ions, when a strong optical intensity leads to depletion of the ground state of these ions. Similar effects can occur in semiconductors, where excitation of electrons from the valence band into the conduction band reduces the absorption for photon energies just above the band gap energy. The coupled rate equations for a passively Q-switched laser can be written as [36]

$$\frac{d\phi}{dt} = \frac{\phi}{t_r}[2\sigma_{es}N_2L - 2\sigma_{gsa}N_1^{sa}L_{sa} - 2\sigma_{esa}N_2^{sa} - ln(1/R) - L'] \tag{3.10}$$

$$\frac{dN_2}{dt} = -\gamma c_0\sigma_{es}\phi N_2 \tag{3.11}$$

$$\frac{dN_2^{sa}}{dt} = -\frac{A}{A_{sa}}c_0\sigma_{gsa}\phi N_2^{sa} \tag{3.12}$$
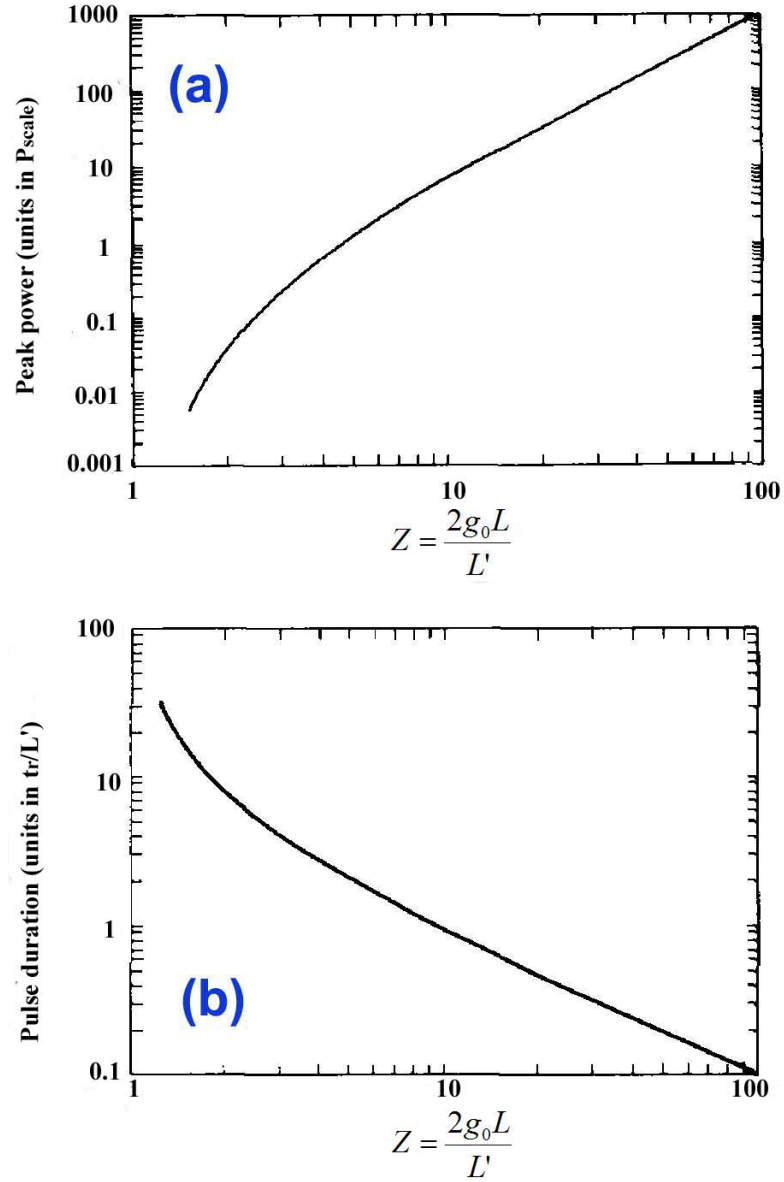
Figure 3.1: The peak power (a) and pulse duration (b) of the optimally coupled laser. The peak power P_{max} is expressed in units of $P_{scale} = hvAL'^2/2\sigma_{es}\gamma t_r$. The FWHM pulse width is in units of t_r/L' [7].

34

$$N^{sa} = N_1^{sa} + N_2^{sa} \tag{3.13}$$

where N_{sa} is the total ion doping, N_1^{sa} and N_2^{sa} are the ground and excited level number intensities; σ_{gsa}, σ_{esa} are the ground-state and excited-state-absorption cross sections of the SA, respectively, L_{sa} is the thickness of the SA, $A(A_{sa})$ is the effective beam area on the gain medium (SA), The threshold inversion density can be expressed as

$$N_t = \frac{ln\frac{1}{T_0^2} + ln\frac{1}{R} + L'}{2\sigma_{es}L} \tag{3.14}$$

where T_0 is the initial transmission of the SA:

$$T_0 = exp(-\sigma_{gsa}N_{sa}L_{sa}) \tag{3.15}$$

If we define

$$\alpha = \frac{\sigma_{gsa}A}{\gamma\sigma_{es}A_s} \tag{3.16}$$

$$\beta = \frac{\sigma_{esa}}{\sigma_{gsa}} \tag{3.17}$$

The criterion for Q-switching behavior is whether the second derivative of photon density ϕ with respective to N_2 at an initial inversion density has a positive value. A criterion to generate a giant pulse in a passively Q-switched laser is derived as [36]

$$\frac{ln(\frac{1}{T_0^2})}{ln(\frac{1}{T_0^2} + ln(\frac{1}{R}) + L'}\frac{\sigma_{gsa}}{\sigma_{es}}\frac{A}{A_{sa}} > \frac{\gamma}{1-\beta} \tag{3.18}$$

Therefore, the initial transmission of the SA has an upper limit $(T_0)_{up}$ for producing a pulse under a given cavity configurations

$$(T_0)_{up} = exp\{-\frac{ln\frac{1}{R} + L'}{2[\alpha(1-\beta) - 1]}\} \tag{3.19}$$

On the other hand, the reflectively of the output coupler has a lower limit $(R)_{low}$ which is given by

$$(R)_{low} = exp\{-[\alpha(1-\beta) - 1]ln(\frac{1}{T_0^2}) + L'\} \qquad (3.20)$$

The output pulse energy of a passively Q-switched laser is given by:

$$E = \frac{hvA}{2\sigma_{es}\gamma} \frac{1}{R} x \qquad (3.21)$$

The parameter x represents the extraction efficiency of the energy stored in the gain medium by the lasing process [37] and it can can be determined by the equation [36]

$$1 - e^{-x} - \frac{(1-\beta)ln(\frac{1}{T_0^2})}{ln(\frac{1}{T_0^2}) + ln(\frac{1}{R^2}) + L'} \frac{1 - e^{-\alpha x}}{\alpha} - \frac{\beta ln(\frac{1}{T_0^2}) + ln(\frac{1}{R^2}) + L'}{ln(\frac{1}{T_0^2}) + ln(\frac{1}{R^2}) + L'} x = 0 \quad (3.22)$$

3.2 Q-switched fiber lasers

Q-switched fiber lasers have been demonstrated with many rare earth doped fibers at different wavelengths, such as Nd at 1.06 μm [27, 38, 39], Er at ~1.5 μm [22, 40–43], Yb at 1-1.1 μm [12–16], Er/Yb ~1.5 μm [24, 44, 45], Pr at 1048 nm [46] and Tm at 1.9-2 μm [47, 48].

3.2.1 Modeling of Q-switched fiber lasers

To simulate Q-switched fiber lasers, a traveling wave model should be employed since the gain and intensity of radiation inside the laser cavity changes significantly as a function of fiber length. Figure 3.2 shows a simplified model of an actively Q-switched fiber laser cavity.

The rate equations for the simulations are given by [8]

$$\pm\frac{\partial J^{\pm}(z,t)}{\partial z} + \frac{1}{v}\frac{\partial J^{\pm}(z,t)}{\partial z} = [g(z,t) - \rho_m]J^{\pm}(z,t) \qquad (3.23)$$

$$\frac{dg(z,t)}{dt} = -\frac{g(z,t)[J^{+}(z,t) + J^{-}(z,t]}{E_s} \qquad (3.24)$$

36

where $J^{\pm}$ are photon fluxes circulating inside the optical cavity, $g(z,t) = N_2(z)\sigma_e$ is the gain coefficient of the medium, N_2 is the population inversion, σ_e is the emission cross section, ρ_m is the loss coefficient, v is the group velocity of light in fiber and $E_s = h\nu/\sigma_e$ is the saturation energy of the gain medium. The gain medium is modeled as a 4-level system and no signal absorption has been included.
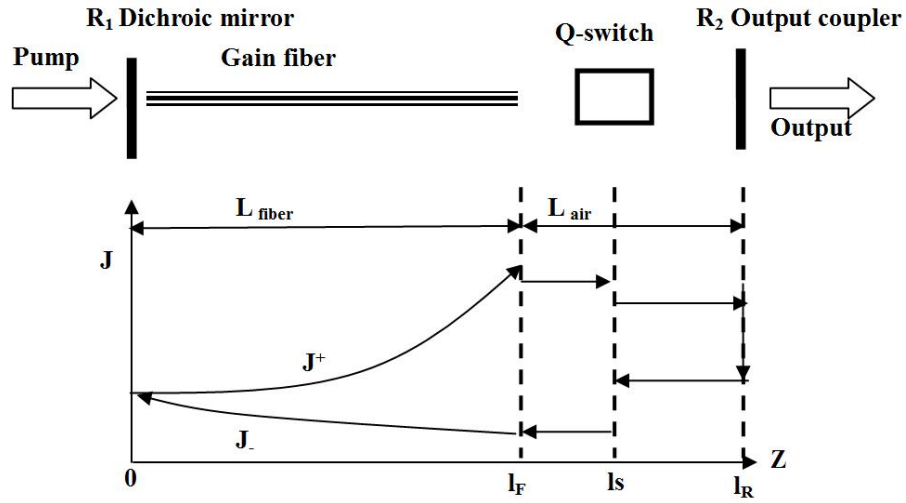
Figure 3.2: A simplified model for a Q-switched fiber laser, J is laser fluence [8].

The equations can be solved with suitable boundary conditions and the Q-switch can be included as

$$J^{\pm}(l_s, t) = T(t)J^{\pm}(l_s, t) \tag{3.25}$$

where $T(t)$ is the transmission characteristics of the active element such as electrooptic modulator. The photon flux escaping the laser cavity can be determined by

$$J_{out} = (1 - R_2)J^+(l_R, t) \tag{3.26}$$

where R_2 is the reflectivity of the output coupler.

3.2.2 Mechanisms of multi-peak pulses in Q-switched fiber lasers

For most of the applications, it is desirable to have a temporally smooth and modulation free single peak pulse with a well defined time interval. However, due to the long geometry and cavity round trip time of fiber lasers, the nonlinear mechanisms in fiber lasers are much more complicated than that in solid state lasers. The pulse shape can be perturbed by many fast dynamics in the cavity. In many cases, the output pulse of Q-switched fiber lasers breaks into a few peaks under a Q-switched envelope with intervals either equal or not equal to the cavity round-trip time. Such a multipeak phenomenon resembles mode locking and has been reported at different output energy levels [8, 13, 16, 40, 41, 49–51].

Some of them are believed to be induced by the active switching elements. Figure 6 in reference [52] shows a periodically modulated mode-locked resembling pulse shape. The separation between individual pulses within the Q-switched envelope is about 18-20 ns (pulse repetition frequency of about 50 MHz), which is much smaller than the 174 ns cavity round trip time (corresponding 5.75 MHz). The modulation is believed to be due to mode beating between the zero order and the first order (frequency shifted) diffracted beams from the AOM. If ω and Ω are the frequencies of the laser and RF modulation of the AO cell, respectively, the first order diffracted beam will have a frequency $\omega + 2\Omega$ after two passes through the AO cell in a round trip of the cavity. The RF wave applied to the Q-switch was 27.12 MHz, corresponding to 2Ω= 54.24 MHz, which matches with the observed beat frequency.

Another mechanism that may cause the pulse shape to break up is the fast switching of the modulator. Figure 7 in reference [49] shows the temporal

pulse shapes for two actively Q-switched Yb fiber lasers with different pump powers. Temporal spacing between two neighboring peaks in each envelope is approximately the round-trip time. The laser dynamics can be understood as follows. When a switching element is quickly switched on, part of the output ASE will be injected into the laser cavity in the form of a pulse, which forms a perturbation to the regular Q-switching, giving step function in circulating power, i.e. sharp rising edge. As a result, the output pulse shape is related to a complicated evolution of the switching induced perturbation in a Q-switching process, and multiple peaks may occur at the laser output. The multi-peak structures can be affected by many factors, such as the switching speed, distributions of the population inversion and ASE. These factors will depend on lasing and pumping wavelengths, pumping method, cavity length, fiber core diameter and dopant concentration, and cavity loss. The output of a single or split pulse depends on whether the switching-induced perturbation is eliminated or enhanced during its later evolution in a Q-switch. Pulse breaking will be eliminated with slow switching, for example, if the rise time of modulator is more than 5-10 times round-trip time. Therefore, being free from the perturbances of active elements is another advantage of passively Q-switched fiber lasers in addition to what we have discussed in Chapter 1.

The nonlinear effects such as SBS and SRS can also cause the Q-switched pulse to break up and form short peaks in fiber lasers, no matter whether the gain switching method is passive or active. Figure 3(c) in reference [50] shows the pulse shape of a Q-switched Yb doped fiber laser with pump power above the SBS threshold. The pulse exhibits fast transient dynamics with a period of 100 ns, which corresponds to the round-trip time of the cavity. The pulse duration is compressed to be less than a few nanoseconds, below the

resolution of the detection system in the experiment. Evidence of SBS is given by the spectra of the laser which is shown in Figure 4(b) in reference [50]. The frequency components are separated by 0.06 nm, which is corresponding to the SBS shift in fiber.

A passively Q-switched fiber laser that uses saturable Raman gain was reported in reference [51]. In the laser setup, a germanium doped fiber was spliced to Yb doped fiber to increase the Raman gain since germinate glass has one of the the highest Raman cross sections among the widely used vitreous Raman materials. Figure 4 and 2 in the reference [51] show the observed pulse shape and spectra, respectively. The fundamental and two orders of Stokes pulses have been obtained. Prior to the emission of the Q-switched first Stokes pulse, the fundamental emission comprises a number of small pulses was observed. The passive Q-switching process can be understood as follows. The fundamental field builds up as series of relaxation oscillations until one of the oscillations exceeds the SRS threshold. The first Stokes pulse builds up relatively quickly and reaches the threshold for the second Stokes and a Q-switched second Stokes pulse is formed. The Stokes pulses cease because of the depletion of stored energy in 1st Stokes pulse. This also allows the the fundamental pulse to grow to its peak power. Thus the residual fundamental emission is observed after the cessation of the Stokes pulses because of the reduced Stokes losses acting on the fundamental field.

3.3 Ytterbium doped gain medium

The Yb ion energy level is very simple, which consists of two-manifolds; the ground manifolds ($^2F_{7/2}$) and a well separated excited manifolds ($^2F_{5/2}$), which include four and three Stark shifted levels, respectively as shown in Figure 3.3.

There is no excited state absorption at either pump or laser wavelengths. The quantum defect is small potentially allowing for high efficiencies and reducing thermal effects in high-power operations. The gain bandwidth of the laser transitions is large due to the overlapping of Stark shifted levels which allows for wide wavelength tuning ranges (975 nm up to 1200 nm), or for generating ultrashort pulses in mode-locked lasers. The upper-state lifetimes are relatively long (typically of the order of 1 ms), which is beneficial for Q-switching.

The small quantum defect also has an unwanted consequence: the significant quasi-three-level behavior, particularly at short wavelengths. This requires such lasers to be operated with relatively high pump intensities and makes it more difficult to realize fully the potential for high power efficiency. Due to the strong broadening (both homogeneous and inhomogeneous) of Yb ions in glass at room temperature, the transitions between the sublevels are not fully resolved. Neither the exact energetic positions of the sublevels, nor the transition cross sections for all the combinations of different sublevels are known.
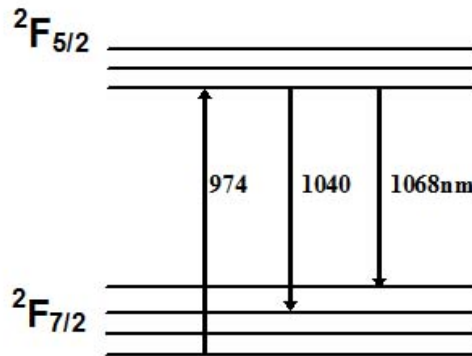
Figure 3.3: Yb energy levels; 974 nm represents pump absorption transition; 1040 nm and 1068 nm represent two lasing transitions in this experiment [9].

The concept of effective cross sections is very useful, particularly for me-

dia with strong spectral broadening. Effective cross sections incorporate both the occupation probabilities for different sublevels of both involved Stark level manifolds and the transition cross sections for all pairs of sublevels. Effective cross sections are usually directly obtained from absorption and emission measurements, and the knowledge of sublevel positions and cross sections for the contributing transitions is not required. The effective absorption and emission cross sections of Yb doped fibers fabricated by LIEKKI are shown in Figure 3.4. Actually, the details of absorption and emission spectra depend to some extent on the host glass composition; for example, with differing content of germanium, aluminum, and boron, typical deviations from the cross sections are up to about 30% [10].

An important fact is that the gain spectrum of a quasi-three-level laser medium depends on the excitation level, because this affects the balance between emission and reabsorption. As a consequence, the laser wavelength obtained depends on the resonator losses: high losses require a higher gain, and thus a higher excitation level, and consequently a shorter wavelength of maximum gain. Figure 3.5 shows the calculated gain spectrum of Yb-doped fiber versus different pump powers at 910 nm, with which nearly complete inversion can be obtained. Emission wavelengths around 975 nm exhibit strong three-level behavior. There is strong absorption when there is no pump, so that the length of an amplifying fiber for this wavelength should be carefully optimized to avoid absorption in an unpumped section. However, for long wavelengths ($\sim$1100 nm), almost pure four-level behavior is observed with the gain proportional to the overall inversion population, and reabsorption in an unpumped fiber is very weak. With 910 nm pump, very high gain in a short length can be achieved at 975 nm, due to the large emission cross section at

42
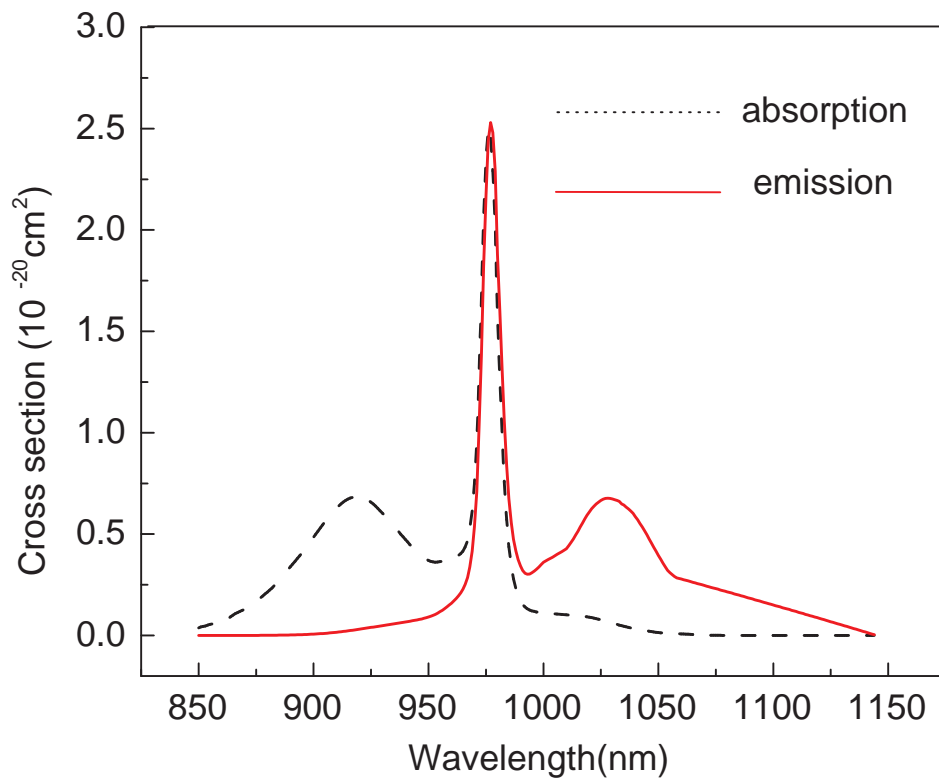
Figure 3.4: Absorption and emission cross sections of ytterbium-doped germanosilicate glass fiber, provided by the fiber manufacturer LIEKKI.
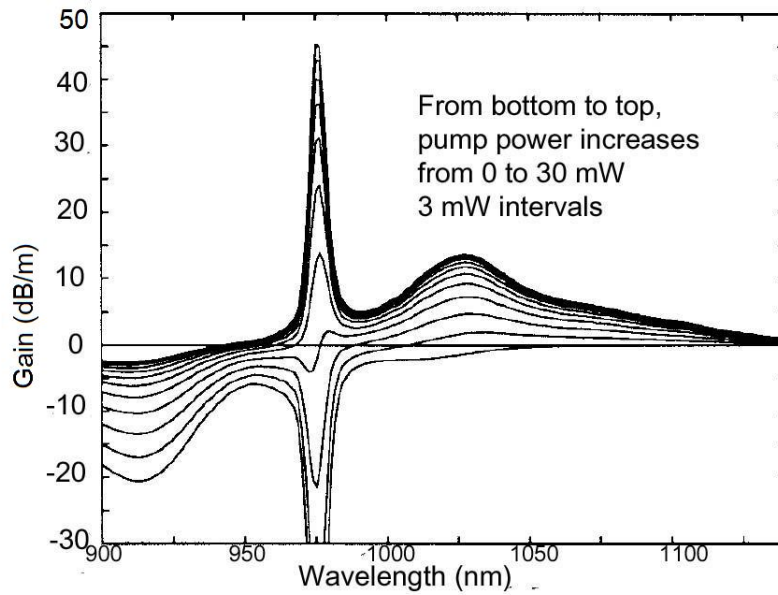
Figure 3.5: Calculated gain spectra for a Yb-doped germanosilicate fiber for different pump powers at 910 nm pump [10].

975 nm, plus the fact that pumping at 910 nm allows essentially all of the Yb population to be excited to the upper manifold. If the signal wavelength to be amplified is 1000-1150 nm, the ASE around 975 nm will limit the gain available at longer wavelengths. One way to get around this limitation is to pump at 975 nm. Figure 3.6 shows the gain spectra for a Yb-doped germanosilicate fiber with 910 nm and 975 nm pump wavelengths with a power high enough to saturate the whole length of fiber.

Although effective cross sections are in principle very simple to use, some important aspects must be considered. Effective cross sections are intrinsically temperature-dependent: temperature changes can affect not only the electronic sublevel positions, but also the relative occupation probabilities within the sublevels. Effective cross sections can be used only when the level population within each Stark level manifold can be assumed to be in thermal equilibrium.

44
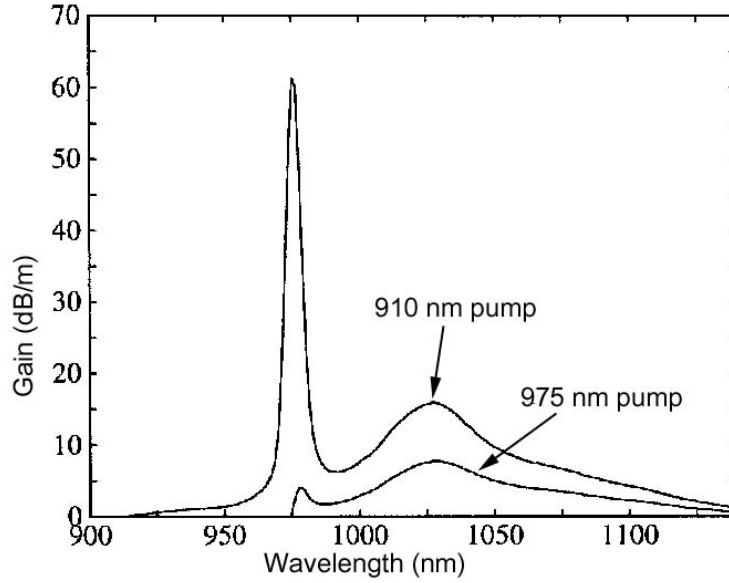
Figure 3.6: Calculated gain spectra for a Yb-doped germanosilicate fiber for 910 nm and 975 nm pumps with a power high enough to saturate the whole length of fiber [10].

3.4 Cr^{4+}:YAG saturable absorber

Cr^{4+}:YAG is an ideal saturable absorber at $1\mu m$ with large absorption cross section, low saturation intensity, high thermal conductivity and damage threshold and good chemical and photochemical stability. Figure 3.7 shows the measured transmission spectrum of a Cr^{4+}:YAG crystal with small signal transmission $T_0 = 50\%$ at 1060 nm.

Because the co-doping with Ca which is required to assure charge compensation, the details of the Cr ions' site symmetry and the resulting energy levels are not entirely known yet. A four-level energy model of Cr^{4+} ions is schematically shown in Figure 3.8. Level 1 is the ground state; optical absorption takes place to the level 3, which then immediately relaxes to the fluorescing state level 2. The lifetime (τ_{sa}) for the spontaneous decay from level 2 to level 1 is in the order of microseconds and the lifetime for the corresponding decay

45
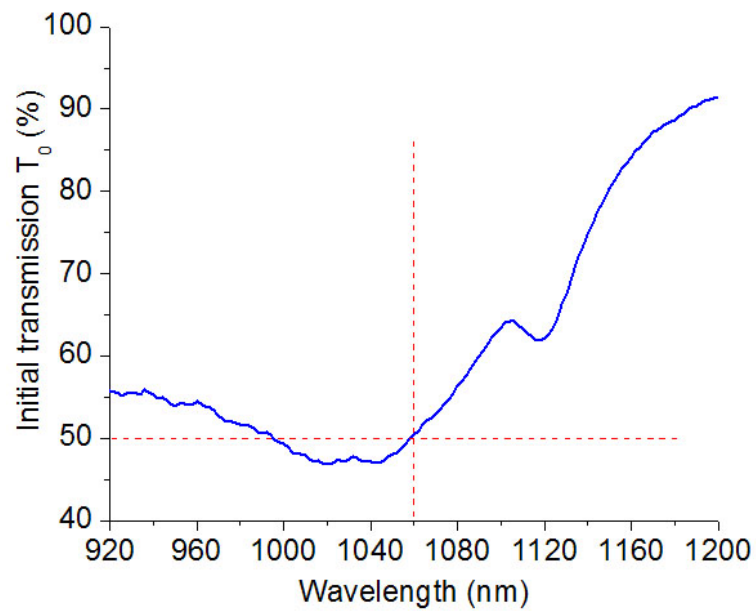
Figure 3.7: Measured crystalline Cr^{4+}:YAG small signal transmission spectrum, the dashed lines mark $T_0 = 50\%$ at 1060 nm. The crystal was fabricated by EKSMA and measured for a $< 111 >$ cut, thickness is $\sim$2.5 mm.
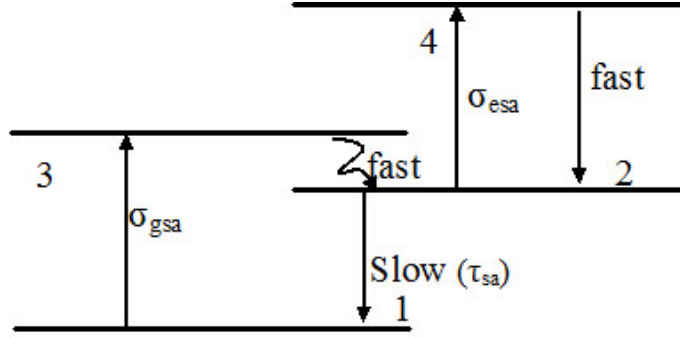
Figure 3.8: Four level model for Cr^{4+}:YAG

between levels 4 and 2 is on the order of picoseconds. The residual absorption is due to the excited-state absorption at the laser wavelength, as well as two-photon absorption of Cr^{4+} and non resonant absorption loss.

Despite the relatively long fluorescence lifetime, it is difficult to estimate the absorption cross section at 1.06 μm because the concentration of the Cr^{3+} is not known. In addition the derivation of these values included fitting procedures for both the cross section values and the concentration of the Cr^{3+} ions. The published cross sections for crystalline Cr^{4+}:YAG at 1.06 μm vary by more than one order of magnitude, which have been shown in Table 3.1. We have used $\sigma_{gsa} = 4.3 \times 10^{-18} cm^2$@1064 nm in this thesis, since it has been employed in many other relative simulations and analysis [53–58] and good agreement has been obtained with experiments.

Because both the radiative and nonradiative transition rates increase with temperature, the lifetime τ_{sa} of Cr^{4+}:YAG is strongly depend on the temperature, as shown in Figure 3.9. τ_{sa} decreased from $\sim$ 30 μs at 15 K to $\sim$ 2 μs at $\sim$360 K.

The transmission of Cr^{4+}:YAG also depends on the angular orientation of the polarization, as described in Figure 1 in reference [62] by Eiler. At low intensities the transmission is completely isotropic through full rotation. As

47

Table 3.1: Cr^{4+}:YAG cross sections at 1.06 μm published in literatures

Reference	σ_{gsa}	σ_{esa}	$\sigma_{gsa}/\sigma_{esa}$
[59]	$3.6 \times 10^{-19} cm^2$	NA	NA
[60]	$(8.7 \pm 0.8) \times 10^{-19} cm^2$	$(2.2 \pm 0.2) \times 10^{-19} cm^2$	4.0
[61]	$(1.9 \pm 0.5) \times 10^{-18} cm^2$	$(5 \pm 1) \times 10^{-19} cm^2$	3.8
[62]	$(5.7 \pm 0.2) \times 10^{-18} cm^2$	$(8 \pm 2) \times 10^{-19} cm^2$	7.1
[63]	$4.3 \times 10^{-18} cm^2$	$8.2 \times 10^{-19} cm^2$	5.2
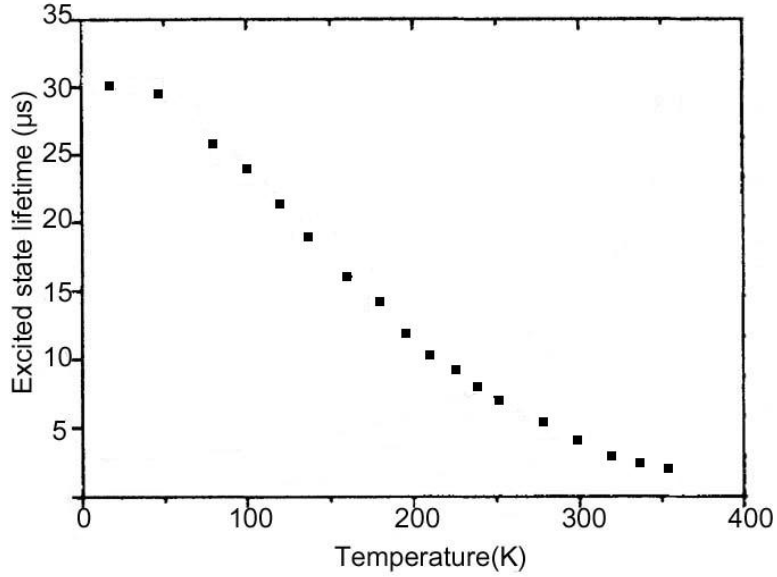
Figure 3.9: Temperature dependence of the lifetime for Cr^{4+}:YAG [11].

the intensity increases, the optical absorption centers become saturated and there is a concomitant observation of anisotropic behavior. However, compared with crystal A with $< 001 >$ cut, the crystal B with $< 111 >$ cut is not very sensitive to the rotation angle, exhibiting a few percent variation. Because of this relatively small sensitivity to orientation for the commonly used $< 111 >$ cut most recent articles about Q-switching using Cr^{4+}:YAG do not cite the orientation of the Cr^{4+}:YAG crystal.

Chapter 4

High repetition rate passively Q-switched ytterbium doped double-clad fiber laser

4.1 Introduction

Because of the tight confinement and long interaction length, stimulated Brillouin Scattering (SBS) is often observed in Q-switched fiber lasers. The SBS process can work like a fast Q-switch and provide strong feedback to the cavity and can generate very short pulses. $\sim$2-ns pulses with kilowatt peak power have been generated with single-mode (SM) [15] and multimode Yb double-clad (DC) [16] fiber. Although the peak power was significantly improved, the pulse stability was relatively poor (standard deviations of approximately 10% in time [15], and 15% in amplitude [16]) due to the stochastic nature of SBS process in silica fibers. In many cases, conventional Q-switched fiber lasers with stable and high repetition outputs are more promising for applications which require consistent and stable output. In this chapter, we present and characterize two high-power and high-repetition-rate passively Q-switched Yb doped double-clad fiber laser geometrics, which have been operated conventionally without showing nonlinear effects.

Modeling of the passively Q-switched fiber laser is also presented including the rate equations for both gain fiber and SA. The traveling wave method is required to accurately describe the inversion density, pump power and radiation power along the fiber. For the SA, a single point model is usually used due to its relatively small thickness [64, 65]. However, focusing is usually required for an external SA in a fiber laser and the focal spot diameter can vary significantly in the SA. Huang et, al. gave an analytical model for optimization of parameters for a passively Q-switched fiber laser with an external Q-switch [16]. In addition, it has been suggested that proper inclusion of amplified spontaneous emission (ASE) is necessary to fully model the operation of a passively Q-switched laser [66]. In this paper, a model including multi-wavelength emission and absorption cross sections is developed to estimate the laser wavelength. The focused beam in Cr^{4+}:YAG is assumed to be Gaussian in shape and traveling wave method is applied to both the Yb fiber and SA. Different spontaneous emission intensities are used in the modeling to investigate their effect on the laser output. The major results from this chapter have already been published in references [67, 68].

4.2 Experiment setup

Two laser configurations used in this experiment are shown in Figure 4.1. For both lasers: the pump laser is a fiber coupled diode laser with a center wavelength of 976 nm. The pump light was coupled into the active fiber by two collimating lenses L1, L2 and a dichroic mirror (DM) with > 96% transmission at 976 nm and > 99% reflectance at 1030-1100 nm. A broadband high-reflection (HR from 750 nm to 1150 nm) mirror at the left side was used as the rear mirror. Lens 3 and lens 4 (also lens 5 in Laser 1) were used to
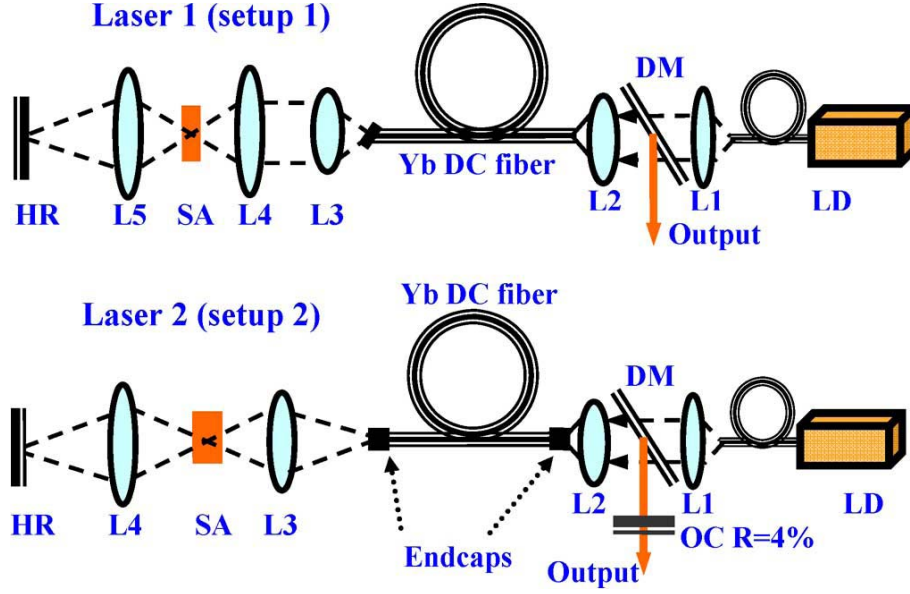
Figure 4.1: Experiment setups; HR-high reflection mirror; SA- Cr^{4+}:YAG saturable absorber; Yb DC fiber-Yb doped single-mode double-clad fiber; DM-dichroic mirror; LD-fiber coupled laser diode; OC-output coupling mirror.

focus the laser through the SA (Cr^{4+}:YAG crystal < 111 > cut). The SA was mounted in an aluminum holder without active cooling. A Picture of the real setup of laser 1 is shown in Figure 4.2.

One difference of the two setups is: in setup 1, the vertically cleaved fiber end face was used as an output coupler; the other fiber end face was angle cleaved to avoid unnecessary reflection. In setup 2, two end-caps were put onto both ends of the fiber and another 4% reflection from a plane surface of a plane-convex lens serves as an output coupler. The end-cap is a small piece of coreless fiber spliced on Yb fiber to protect the fiber end face. To keep the output beam quality, the maximum length of end-cap can be estimated by

$$L_{max} = \frac{d.n}{2NA} \tag{4.1}$$

where d (for example 125 μm) is the diameter of endcap, n (1.5) is the refractive index, NA (0.08 for the Yb fiber in Laser 2) is the numerical aperture. The

52
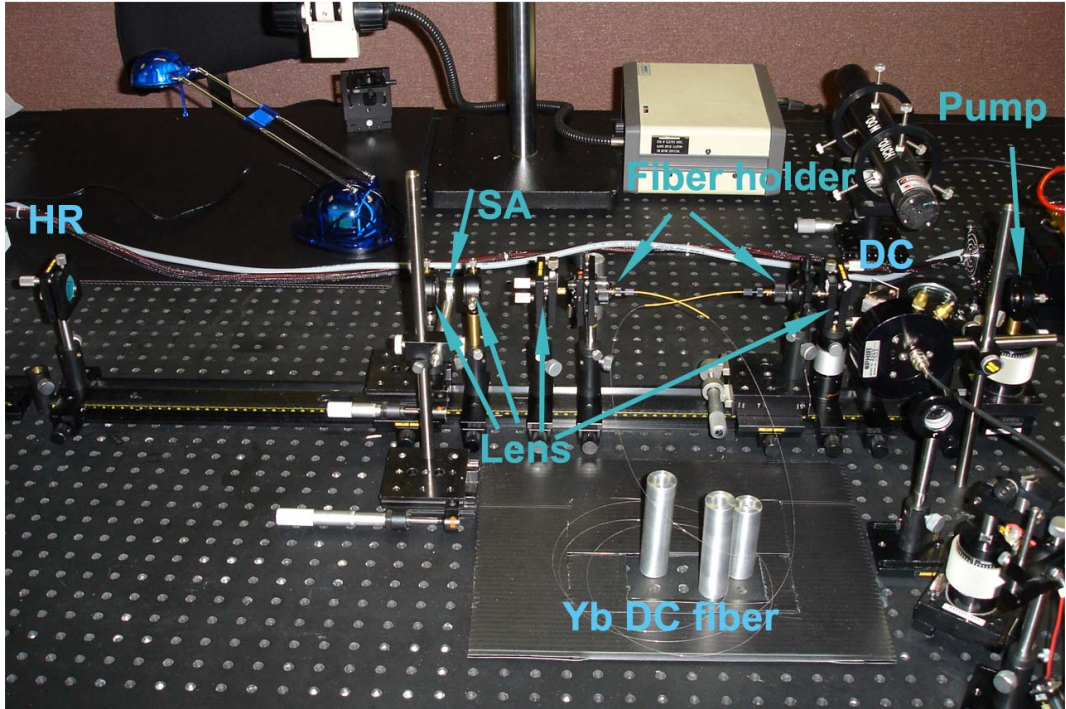
Figure 4.2: Picture of passively Q-switched fiber laser setup 1.

maximum length of endcap for Laser 1 is calculated to be ∼1.17 mm.

Setup 1 has the merits of easy alignment and lower loss; while Setup 2 has the advantage of supporting higher peak power without fiber end face damage. The other difference of the setups is: in setup 1, the angle cleaved end of the fiber was put ∼ $1 \times f$ (f: focal length of lens 3) distance from L3; the light was first collimated and then focused by L4. In setup 2, the fiber end was put ∼ $2 \times$ f distance from L3; the output beam was directly focused by L3. In setup 1, it is estimated ∼28% of the coupled pump power was left unabsorbed, and ∼75% of this was collected by L3 and focused on SA; while in setup 2 most of the residual pump which was only ∼2% of the coupled pump power was lost to free space. The effects that the residual pump induced in the SA in setup 1 will be discussed in a later section. Other details of the two lasers configurations are listed in Table 4.1.

Table 4.1: Laser Configurations

	Laser 1	Laser 2
Fiber length	3.0 m	2.8 m
Fiber core diameter, NA	D=5.4 μm **, NA=0.15	D= 10 μm, NA=0.08
Mode field diameter	$2\omega_0$=6.0 μm	$2\omega_0$=11.2 μm**
Cladding diameter, NA	ϕ=125 μm, NA=0.46	ϕ=125 μm, NA=0.46
Pump absorption (nominal)	2.6 dB/m	6.5 dB/m
Lens 3	f=6.24 mm, NA=0.4	f=11 mm, NA=0.3
Lens 4 (Lens 5)	f=15 mm	f=15 mm
Center lasing wavelength λ_0	1074 nm*	1072 nm*
SA transmission T_0 at λ_0	T_0=56%	T_0=35%
SA T_0 at 1064 nm	T_0=50%	T_0=30%
SA thickness L_{sa}	2.5 mm*	4.5 mm*
Focal ratio in SA	1:2.4**	1:1**

*Experimentally measured; **Calculated from manufacture specifications; all other values without asterisk are manufacture specifications. Fiber manufacture: LIEKKI.

4.3 Experiment results

At first the laser was aligned and the focal spot position in the SA was carefully adjusted until maximum single pulse amplitude was observed in an oscilloscope. The experimentally measured laser output characteristics: average output power, pulse-repetition-rate, pulse duration, and pulse energy versus the pump power are shown in Figure 4.3 (a, b, c, d). As can be seen in the figure, for the two lasers, the average output power and pulse-repetition-rate increased almost linearly with pump power; pulse durations decreased with pump power; and pulse energy increased slowly with pump power. The measured output wavelengths of the two lasers were centered at 1074 nm and 1072 nm with a linewidth of ∼3 nm. Figure 4.4 shows measured laser spectra at a pump power of 7.1 W. The center wavelengths were stable with pump power; however the linewidth of Laser 1 was observed to increase with pump power up to ∼5 nm. The broad spectra helped avoid any SBS effects in fiber and the lasers operated as conventionally Q-switched lasers. The Q-switched pulse shape was smooth and no SBS induced rapid temporal evolution was observed.

For Laser 1, 5.2 W output power has been obtained at a pump power of 10.1 W, with a pulse-repetition-rate of 282 kHz and a slope efficiency of 51%. The pulse energy increased from 13.4 μJ to 18.4 μJ when the pump power increased from 2.6 W to 10.1 W and the pulse duration was observed to decrease from 230 ns to 152 ns. Figure 4.5 shows a pulse train obtained at a pump power of 10.1 W. For Laser 2, 7.8 W output has been obtained at a pump power of 13.8 W, with a pulse-repetition- rate of 120 kHz and a slope efficiency of 55%. Although there is more cavity loss than Laser 1, Laser 2 achieved higher slope efficiency due to the higher pump absorption by the large core Yb fiber used in this setup. The pulse energy was also much higher
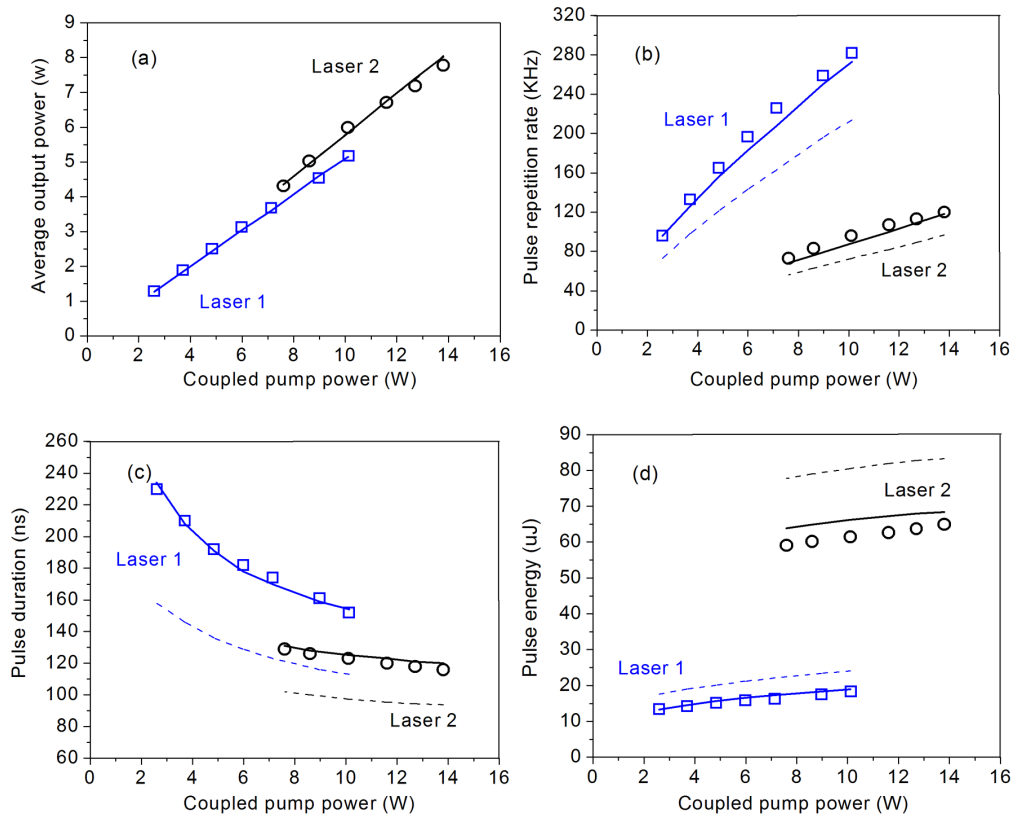
Figure 4.3: Laser output characteristics versus coupled pump power; separated dots: experimental results; dashed lines: theoretical simulations with $\xi_{k1} = 1.8 \times 10^{-31} W.m^2$, solid lines: theoretical simulations with $\xi_{k1} = 5.4 \times 10^{-29} W.m^2$; in (a) the solid lines and dashed lines overlap.
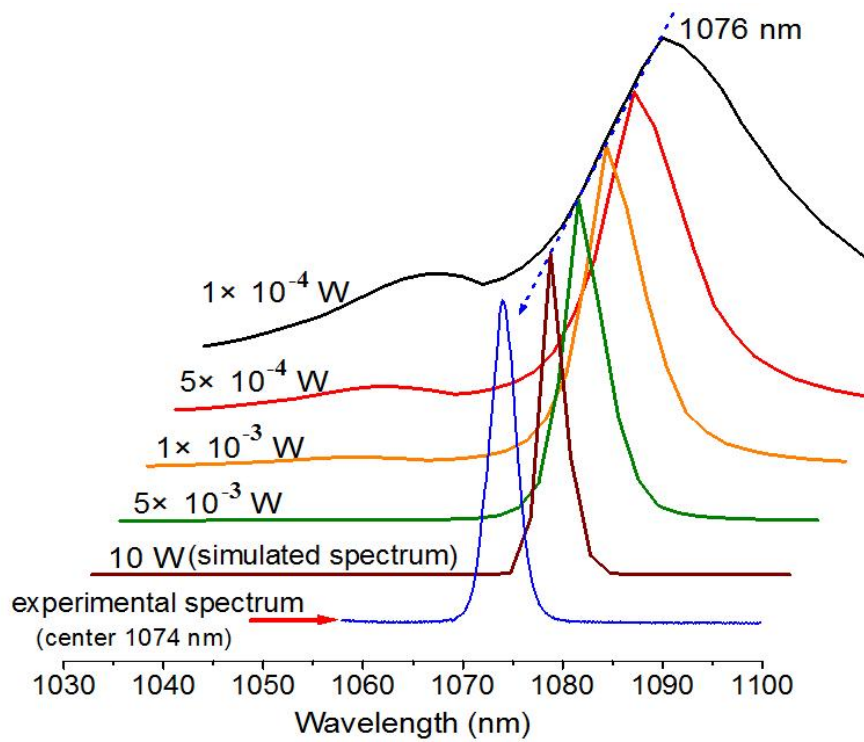
Figure 4.4: Experimentally measured spectrum and simulated laser emission spectrum building up from ASE for Laser 1 at a pump power of 7.1 W. The overall ASE output power is marked on the left side of the simulated curves and the intensities have been normalized by the 1076 nm peak for convenience of viewing.
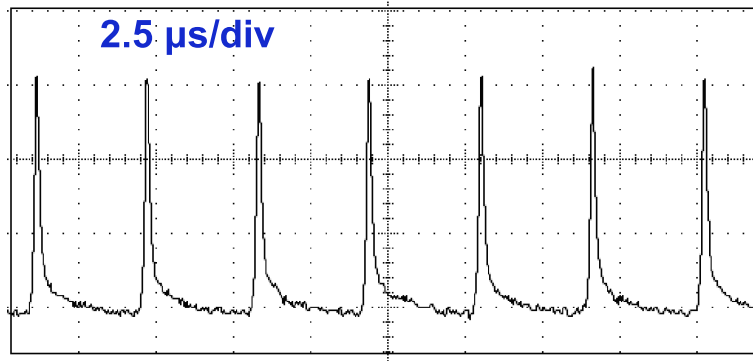
Figure 4.5: Observed pulse trains of Laser 1 at a pump power of 10.1 W with pulse repetition rate 282 kHz.

than that of Laser 1, which increased from 59 μJ to 65 μJ when the pump power increased from 7.6 W to 13.8 W. The pulse duration was observed to decrease from 129 ns to 116 ns, correspondingly. Figure 4.6 (a, b) shows a typical pulse shape and a pulse train obtained by Laser 2 at a pump power of 13.8 W. As can be seen in both Figure 4.5 and Figure 4.6, the pulse shapes are not symmetric in shape. A long decay time is observed at the trailing edge. Similar pulse profiles were also observed in other Q-switched Yb fiber lasers [13, 14, 17], however, no detailed explanation has been given yet for this tail.

The average timing jitter was measured to be less than 1% for Laser 1 and less than 0.5% for Laser 2, respectively, which are an order of magnitude better than passively Q-switched fiber laser exhibiting SBS effects [15]. Figure 4.7 shows an example of the pulse timing jitter measurements, which was measured by using the second pulse next to the triggering pulse.
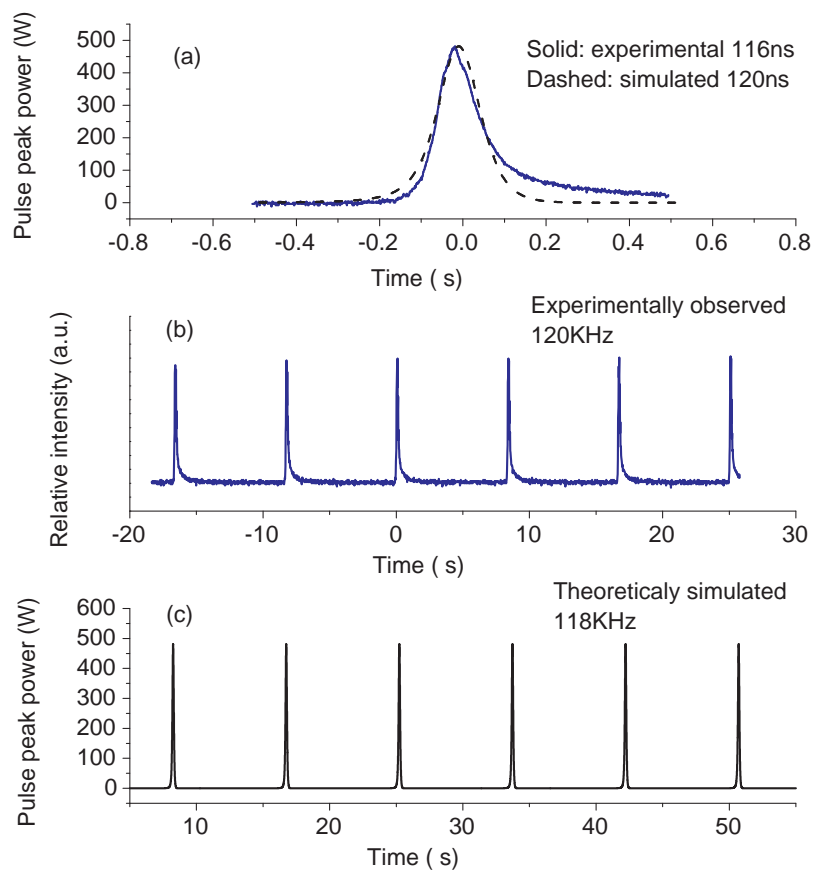
Figure 4.6: Experimental and simulated pulse shape and pulse trains of Laser 2 at a pump power of 13.8 W.
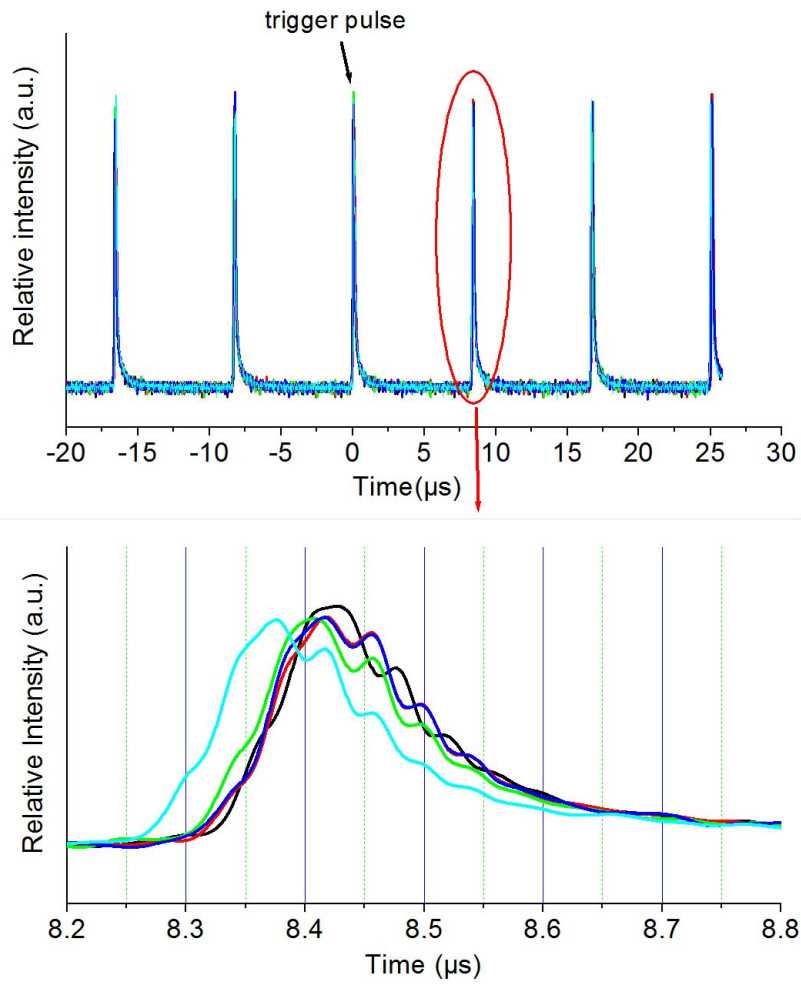
Figure 4.7: An example of the pulse timing jitter measurements at a pump power of 13.8 W. 5 pulse overlaps are used, which show a RMS timing jitter of 0.2%. The varying pulse heights are due to the low sampling rate of the oscilloscope when measuring the pulse train.

4.4   Discussion and analysis

4.4.1   SBS threshold

The Q-switched pulse shape was smooth and no SBS induced rapid temporal
evolution was observed. Taking Laser 1 as an example, the threshold power
for onset of SBS can be estimated as follows

$$P_{th} = 21\frac{A_{eff}}{g_B L_{eff}}\frac{\Delta\nu_L}{\Delta\nu_B} \tag{4.2}$$

where A_{eff} is the effective mode area ($28 \times 10^{-12}m^2$ for Laser 1), g_B is the
Brillouin gain coefficient ($5 \times 10^{-11}m/W$), $\Delta\nu_L$ and $\Delta\nu_B$ are the laser signal
and Brillouin gain bandwidth ($80 \times 10^6 Hz$), L_{eff} is the effective fiber length,
which can be estimated by

$$L_{eff} = \frac{2L}{ln(\frac{1}{R_1 R_2})} \tag{4.3}$$

where L is the fiber length (3 meter for Laser 1), R_1, R_2 are the signal feedback
at each end of the fiber, respectively (R_1 75%, R_2 4%). If we use a laser
linewidth of 3 nm, $\Delta\nu_L = 7.9 \times 10^{11}$ Hz. The SBS threshold is calculated
to be 68 kW for Laser 1, which is much higher than the peak pulse power
observed. Thus, the SBS gain is too low to provide effective SBS feedback. In
this case, the laser operates like a conventional Q-switched laser.

4.4.2   Saturable absorber recovery time

In a passively Q-switched laser, the pulse energy dependence on pump power
is affected by multiple factors. One of them is the SA and its recovery time
T_s (should be much longer than excited state lifetime τ_{sa}). In the low pump
power region, when the inter-pulse period T is much longer than T_s, the SA
recovers completely between laser pulses and the initial inversion population

is constant when the gain reaches the threshold value. However inversion population N_i will continue to increase during the growth of the pulse due to the ongoing pump power until the radiation intensity in the cavity is high enough to extract the stored inversion population energy, which causes the pulse energy to increase with pump power [37]. In a high pump regime, when T is smaller than T_s, the SA will not recover well between the pulses and N_i becomes lower, which can induce a decrease of pulse energy with pump power [69]. In addition, thermal lensing and other thermally induced losses as well as pump-induced bleaching in a micro-chip laser can also cause the pulse energy to decrease at high pump power. This rise and drop of pulse energy with pump power has been observed in a few passively Q-switched solid-state lasers [69–71].

However, such behaviour did not occur in the two lasers described in this work; the pulse energies increased almost linearly with pump powers up to 10.1 W and 13.8 W, with pulse-repetition-rates of 282 kHz and 120 kHz, for lasers 1 and 2 respectively, as shown in Figure 4.3 (b). The excited-state lifetime τ_{sa} of Cr^{4+}:YAG is 4 μs at room temperature and decreases at a rate of 0.04 $\mu s/^0C$ with increasing the temperature [11, 72]. To avoid pulse energy decreasing with pump power, the gain recovery time T_G should be much longer than τ_{sa}. For a pulse repetition-rate of 282 kHz, the inter-pulse period T_G is only 3.55 μs, which is of the order of τ_{sa} at room temperature. However, it is expected that there is significant lifetime shortening due the temperature increase of Cr^{4+}:YAG in these experiments. Because the pump light was continuous wave (CW) and transmitted in the fiber inner cladding, the focal area on the SA would be large (focal spot diameter $\sim$300 μm in Laser 1). The bleaching of the SA by the pump light intensity would be insignificant

and can be ignored. However it will cause the local temperature to increase. For Laser 1, the temperature induced by pump light can be estimated from a steady state cylindrical heat flow model with temperatures given by

$$T_1 = \frac{w}{2\pi\kappa} ln\frac{R_0}{R_1} + T_0 \qquad (4.4)$$

where κ is crystal thermal conductivity (0.12 W/cm.K), R_0 is crystal outer radius (0.5 cm) and R_1 is the radius of the heated pumped region (150 μm), T_0 is the temperature of the aluminium holder and considered as the temperature at the crystal edge, T_1 is the temperature at R_1; $w = P_{abs}/L_{sa}$, where P_{abs} is absorbed pump power and L_{sa} is crystal thickness. At a pump power of 10.1 W, $P_{abs} \sim$2 W and T_0 was measured to be $\sim 60^0C$, T_1 was calculated to be $\sim 97^0C$. The SA temperature will be further increased during transient Q-switching process in a very small focal position ($\sim$10-15 μm focal spot diameters) and somewhat decreased due to cooling from the end faces which is not taken into account. The SA temperatures for Laser 1 and 2 at high pump power were estimated to be approximately 97^0C and 60^0C, respectively. Therefore, SA recovery times of τ_{sa}=1 μs and τ_{sa}=2.5 μs were used for Lasers 1 and Laser 2 respectively in the simulation. This would ensure $\sim$97% excited-state density recovery when operating at maximum repetition rates (282 kHz for Laser 1 and 120 kHz for Laser 2).

4.5 Numerical modeling

4.5.1 Rate equations

Figure 4.8 shows the schematic diagram of the modeling. A two-level system is used to model the Yb laser and Cr^{4+}:YAG SA. The rate equations to model the Yb doped fiber are as follows [73]

$$N_0 = N_1(t) + N_2(t) \tag{4.5}$$

$$\frac{\partial N_2(x,t)}{\partial t} = \frac{\Gamma_p \lambda_p}{hcA_{co}}[\sigma_{\alpha p}N_1(x,t) - \sigma_{ep}N_2(x,t)]P_p^-(x,t)$$
$$+ \sum_k \frac{\Gamma_k \lambda_k}{hcA_{co}}[\sigma_{\alpha k}N_1(x,t) - \sigma_{ek}N_2(x,t)] \times (P_k^+(x,t) + P_k^-(x,t)) - \frac{N_2(x,t)}{\tau} \tag{4.6}$$

$$-\frac{\partial P_p^-(x,t)}{\partial x} + \frac{1}{v_p}\frac{\partial P_p^-(x,t)}{\partial t} = \Gamma_p[\sigma_{ep}N_2(x,t) - \sigma_{\alpha p}N_1(x,t)]P_p^-(x,t) - \alpha_p P_p^-(x,t) \tag{4.7}$$

$$\pm \frac{\partial P_k^\pm(x,t)}{\partial x} + \frac{1}{v_k}\frac{\partial P_k^\pm(x,t)}{\partial t} = \Gamma_k[\sigma_{ek}N_2(x,t) - \sigma_{\alpha k}N_1(x,t)]P_k^\pm(x,t)$$
$$-\alpha_k P_k^\pm(x,t) + N_2(x,t)\xi_k \tag{4.8}$$

where N_0 is the total Yb doping concentration; N_1 and N_2 are ground and excited states densities. P_p^- represents the backward propagating pump power. $P_k^\pm$ are the forward and backward propagating laser radiation, k is a wavelength index allowing multiple wavelengths to grow within laser cavity simultaneously; $\sigma_{\alpha p}$, σ_{ep}, $\sigma_{\alpha k}$ and σ_{ek} are the absorption and emission cross sections of Yb ion at pump wavelength and emission wavelength, respectively. The pump (emission) and fiber core overlap factors $\Gamma_p(k)$ were calculated with a Gaussian shape assumption for the signal wave; $\lambda_p(k)$ are the pump (emission) wavelengths in vacuum; $v_{p(k)}$ are pump (emission) group velocities, which were both set to c/n, where c is the speed of light in vacuum and n is fiber refractive index; h is the Planck constant, τ is the lifetime of Yb ion, and $\alpha_p(\alpha_k)$ is the fiber attenuation at the pump (emission) wavelength.
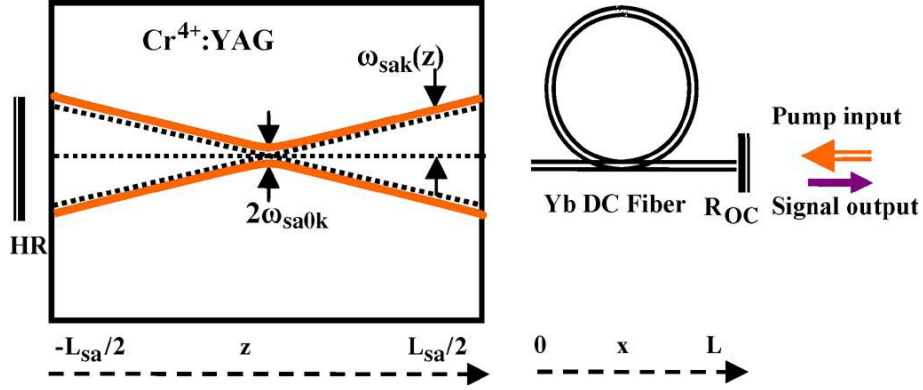
Figure 4.8: Schematic diagram for simulation; HR: high reflection mirror, R_{OC}: output coupler reflection, the dashed arrows mark the direction convention for distance z in the SA and x in the fiber for numerical simulation. L_{sa} is the thickness of SA; L is the length of the fiber

$N_2(x,t)\xi_k$ in (4) represents spontaneous emission in fiber core and

$$\xi_k = M\Gamma_k\sigma_{ek}\frac{hc^2}{\lambda_k^3}\Delta\lambda_k \qquad (4.9)$$

with units of Wm^2, in which M and $\Delta\lambda_k$ are the number of transverse modes and bandwidth of spontaneous emission, respectively. A traveling wave model was also used to depict the Cr⁴⁺:YAG SA, the rate equations are

$$N^{sa} = N_1^{sa}(t) + N_2^{sa}(t) \qquad (4.10)$$

$$\frac{\partial N_2^{sa}(x,t)}{\partial t} = \sum_k \frac{\lambda_k}{hcA_{sak}(z)}\sigma_{gsak}N_1^{sa}(z,t) \times [P_{sak}^+(z,t) + P_{sak}^-(z,t)] - \frac{N_2^{sa}(z,t)}{\tau_{sa}} \qquad (4.11)$$

$$\pm\frac{\partial P_{sak}^\pm(z,t)}{\partial z} + \frac{1}{v_{sa}}\frac{\partial P_{sak}^\pm(z,t)}{\partial t} = \qquad (4.12)$$
$$[-\sigma_{gsak}N_2^{sa}(z,t) - \sigma_{esak}N_2^{sa}(z,t)]P_{sak}^\pm(z,t) + \alpha_{sa}P_{sak}^\pm(z,t)$$

where N_{sa} is the total ion doping, N_{sa}^1 and N_{sa}^2 are the ground and excited state densities; $P_{sak}^\pm$ are the forward and backward propagating laser power

65

in the SA. σ_{gsak}, σ_{esak} are the ground-state and excited-state absorption cross sections, respectively. τ_{sa} is the lifetime of the excited state; $v_{sa} = c/n_{sa}$ is the light speed in the SA, n_{sa} is the refractive index of Cr^{4+}:YAG. α_{sa} is non-saturable loss other than excited-state absorption. The focused beam in the SA was assumed to propagate as a Gaussian beam where $A_{sak}(z) = \pi\omega_{sak}^2(z)$ is the beam area at position z in the SA and $\omega_{sak}(z)$ is the beam radius, which was determined by

$$\omega_{sak}(z) = \omega_{sa0k}(z)[1 + (\frac{z}{z_0})^2]^{1/2} \tag{4.13}$$

$$z_{0k} = \frac{\pi\omega_{sa0k}^2 n_{sa}}{\lambda_k} \tag{4.14}$$

where ω_{sa0k} is determined by the mode field diameter in the fiber and focal ratio in SA. It is found that the maximum pulse energy in the simulation was obtained when the focal spot was located in the exact middle position of the SA. The above equations are solved under the boundary conditions given as

$$P_p^-(L,t) = P_0 \tag{4.15}$$

$$P_k^-(L,t) = P_k^+(L,t).R_{oc} \tag{4.16}$$

$$P_{sak}^-(L_{sa}/2,t) = P_k^-(0,t).(1-\eta) \tag{4.17}$$

$$P_{sak}^+(-L_{sa}/2,t) = P_{sak}^-(0,t).(-L_{sa}/2,t) \tag{4.18}$$

$$P_k^+(0,t) = P_{sak}^+(0,t)(L_{sa}/2,t).(1-\eta) \tag{4.19}$$

$$P_{output-k}(t) = P_k^+(L,t).(1-R_{oc}) \tag{4.20}$$

where P_0 is the pump power, L is the fiber length, L_{sa} is the thickness of SA. $R_{oc} = 0.04$ is the reflectivity of the output coupler, $\eta \sim 15\%$ is the one way cavity loss due to Fresnel reflection of fiber face, lens coupling and coating

loss. $P_{output-k}$ is the output power. For Laser 2, an additional 5% one way loss was estimated due to the end-caps and coupling mirror at the output end. To ensure high precision in the calculations, the fiber and SA are divided into 200 and 50 segments, respectively. The coupled equations are numerically solved with steps in space and time as: $dx = L/200$; $dz = L_{sa}/50$; $dt = dx/(nc)$. In simulation, ~ 30 cm free space in cavity each way has also been considered. The parameter values used in the simulation are shown in Table 4.2.

Table 4.2: Values of parameters in simulation

Parameters	Values	Parameters	Values
N_0	$9 \times 10^{19}/cm^3$	τ	$850\mu s$
$\sigma_{e1072nm}$	$2.40 \times 10^{-21}cm^2$	$\sigma_{e1074nm}$	$2.34 \times 10^{-21}cm^2$
$\sigma_{\alpha1072nm}$	$1.75 \times 10^{-23}cm^2$	$\sigma_{\alpha1074nm}$	$1.16 \times 10^{-23}cm^2$
$\Gamma_{k1074nm}$	0.803	$\Gamma_{k1074nm}$	0.798
$\Gamma_p(Laser1)$	1.87×10^{-3}	$\Gamma_p(Laser2)$	6.40×10^{-3}
α_p, α_k	$0.005m^{-1}$	α_{sa}	$0.01mm^{-1}$
$\tau_{sa}(Laser1)$	$1\mu s$	$\tau_{sa}(Laser2)$	$2.5\mu s$
N^{sa}	$6.2 \times 10^{17}/cm^3$	$\sigma_{gsa1072-1074nm}$	$3.8 \times 10^{-18}cm^2$
$\sigma_{gsa}/\sigma_{esa1072-1074nm}$	3	n_{sa}	1.82
n	1.45		

4.5.2 Laser spectrum simulation

To estimate the laser center wavelength, 36 wavelengths were included from 1030 nm to 1100 nm with $\Delta\lambda = 2nm$ separation between them to simulate the laser emission built up from the broad band spontaneous emission spectra. The Yb emission and absorption cross sections were taken from the data provided by the fiber manufacturer (as shown in Figure 3.4). The SA σ_{gsak} at λ_k is

calculated by the reported value at 1064 nm ($4.3 \times 10^{-18} cm^2$ [53]) and corrected for wavelength by using the measured initial transmission T_0 at 1064 nm and from 1030-1100 nm. The ratio of $\sigma_{gsak}/\sigma_{esak}$ was estimated by using linear fit of the values at 1064 nm and 1047 nm reported in reference [74]. Figure 4.4 shows the simulated laser emission built up from ASE spectrum for Laser 1 at a pump power of 10.1 W. At the beginning when the inversion density is below the threshold, there is no actual lasing and the ASE spectrum is broad with a peak wavelength of 1076 nm. With an increase of the inversion density, the ASE power becomes higher and the spectral peak becomes narrower; only the spectrum within a few nanometers of the center wavelength could reach the threshold for lasing, as shown by the curve marked with 10 W. The simulated laser spectrum agrees well with the experimentally measured spectrum and does not depend on pump power. The same simulated center wavelength and similar spectral shape were also obtained for Laser 2. The minor center wavelength difference may be due to minor discrepancies between the cross section values used in the simulations as compared to the real fiber. The slight wavelength dependence of optical coatings might be another factor, since it is not included in the simulation.

4.5.3 Modeling of Q-switching

To model the Q-switched behavior of the laser we solved the numerical model using the single peak measured output wavelength. As shown in Figure 4.4 the ASE seeds the build up of the pulse. In addition, the ASE can deplete the population inversion and limit the laser performance if the net single pass gain is large enough. However this was not a major factor in this experiment since the lasers operated at a high-repetition-rate and the gain is low ($\sim$10 dB

each way maximum). After the laser reaches the threshold, the ASE emission within the laser radiation bandwidth and within the guided mode acts as the seed during the build up of the Q-switched pulses. If we use M=2 (single mode and two polarizations) and $\Delta\lambda_k = 10nm$ with a center emission wavelength $\lambda_k = 1074nm$, ξ_k is estimated to be $\sim 1.8 \times 10^{-31}$ by Eq. 4.9. Besides the value of $\xi_{k1} = 1.8 \times 10^{-31}$, another much higher value of $\xi_{k2} = 1.8 \times 5.4^{-29}$ was also used in the simulation to compare to the results. This value was chosen to give a better fit to the measured results.

The pulse energy is determined by integration of instantaneous output power over a period including one pulse. The average output power is calculated by pulse energy multiplied by pulse repetition rate. The simulated laser average output power, pulse repetition rate, pulse duration and pulse energy with two spontaneous emission, ξ_k, coefficients are shown in Figure 4.3 (a, b, c, d) with dashed and solid lines, respectively. Except for average output powers, which show no difference for the two ξ_k values, the simulation with ξ_{k2} results in much better agreement with experimental values for both laser systems. The simulation with ξ_{k1} generates much higher pulse energy, as well as lower repetition rate and shorter pulse duration than measured in the experiment. The higher ξ_k value gives better agreement with experiment indicating that ASE is significantly underestimated by only considering the spontaneous emission near λ_k using Eq. 4.9. A similar conclusion, that a higher ASE level was required to model experimental measurements, was given in reference [66], in which the ASE parameters were deduced by fitting experimental results. Although the full mechanism for this requirement for a higher ASE level in the model is not understood yet, we believe it is related to the long tail on the pulse profile and leading to a higher level of residual photons remaining from

the previous pulse.

One simulated pulse shape and pulse train with ξ_{k2} and Laser 2 at a pump power of 13.8 W are shown in Figure 4.6 (a, c). The pulse power shows the instantaneous output power of the simulated Q-switched pulses. As can be seen in Figure 4.6 (a), the simulation did not reproduce the long trailing edge of the experimental pulse. Similar pulse profiles with tails were also observed in Q-switched Nd doped lasers [54, 75]. They could be explained by the finite lifetime of the real lower laser level [76], which is determined by the relaxation between manifolds and thermalization among sublevels [77] with the real ground state. The thermalization within Yb lower manifold $^2F_{7/2}$ is normally believed to be very fast. However with relatively large energy splitting (up to $1490cm^{-1}$ in silica fiber [78]), multi-phonon transitions will be required and the thermalization time might be longer than expected. In addition, transient and cw heating may lead to higher temperatures which might be another factor. The fiber core temperature will increase during a pulse peak by the heat generated from the quantum defect, nonradiative relaxation, partial absorption of the laser radiation, etc. Since the thermal relaxation time for the fiber core is in the $\sim \mu$s range [79], the core temperature will decrease during the tail of the pulse. The population of the higher sublevel, which is the laser lower level, will decrease with temperature, which may induce additional gain for the laser radiation and cause the long decay time of the pulse observed.

By using the travelling wave method, the two-way radiation powers and excited-state density in the SA at each position at any instant in time can be determined. Figure 4.9(a) and (b) show the distributions of N_2^{sa} distributions along z at different times when the radiation power (sum of the two-way power) at the middle position of the SA reaches different levels. Significant non-

70

uniformity of the saturation of the SA was observed in both lasers. As can be seen in the figures, the center part of SA is saturated first; the saturated region then gradually expands with the increasing laser intensity; the edge parts are not totally bleached even when the laser power reaches its maximum value. The simulation predicts that if a thinner SA (but with higher doping level to the transmission constant) is used in experiment, higher pulse energy and shorter pulse duration (thus higher peak power) will be obtained, since better saturation can be achieved under the same focusing conditions. Table 4.3 shows the comparison results of the predicted pulse energy and duration for different doping level and thickness of the SA.

Table 4.3: Comparison of predicted pulse energy and duration if increased doping level and reduced thickness of the saturable absorber

SA doping level		
N^{sa}	$6.2{\times}10^{17}/cm^3$(current)	$15.5{\times}10^{17}/cm^3$
SA thickness		
$T_0 = 50\%$	2.5 mm	1 mm
Estimated pulse energy		
Laser 1		
pump power 10.1 W	18.9 μJ	23.8 μJ
Estimated pulse duration		
Laser 1		
pump power 10.1 W	154 ns	110 ns

For the convenience of discussion, a position averaged inversion density $\underline{N}_2(t)$ in the Yb fiber and a position averaged excited-state density in the SA $\underline{N}_2^{sa}(t)$ at any instant in time are defined as follows:

$$\underline{N}_2(t) = \int_0^L \frac{N_2(x,t)dx}{L} \tag{4.21}$$
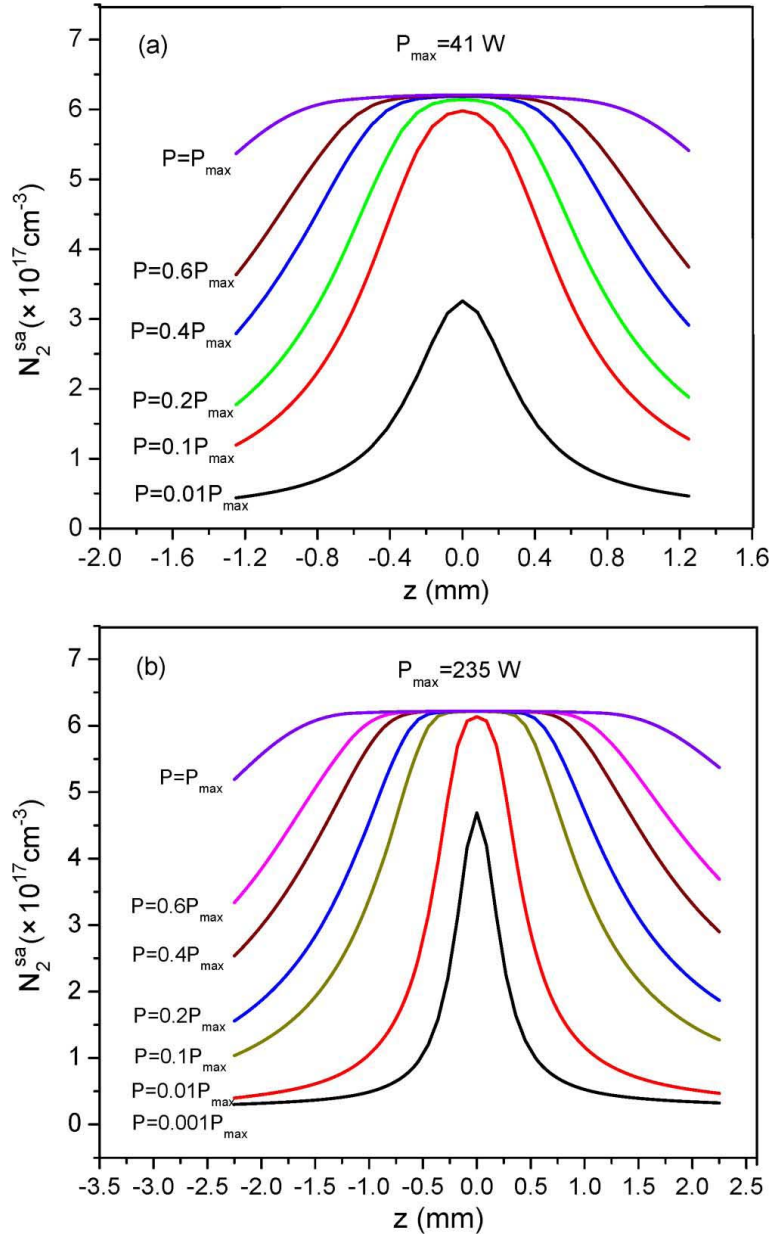
Figure 4.9: Excited-state density distributions of SA along z at different times during pulse build up when the power at the center (z=0) position reaches different levels. P_{max} is the maximum power at the center position that is observed under current pump power; (a) Laser 1 at a pump power of 10.1W, (b) Laser 2 at a pump power of 13.8W. Both the figures are obtained under ξ_{k2}.

$$\underline{N}_2^{sa}(t) = \int_0^{L_{sa}} \frac{N_2^{sa}(z,t)dz}{L_{sa}} \tag{4.22}$$

Figure 4.11 shows dynamics of $\underline{N}_2(t)$ and $\underline{N}_2^{sa}(t)$ for pulses with different ξ_k values at a pump power of 2.6 W, which illustrates how the ASE level affects the pulse energy during the pulse built up in a passively Q-switched fiber laser. At time t_0, $\underline{N}_2(t) = \underline{N}_2(0)$, which is close to thresholds; altlhough there is a minor difference between the thresholds for the two cases due to slight saturations of the SA by the different ASE intensities. $\underline{N}_2(t)$ will continue to increase due to pump power until the radiation intensity reaches a certain level in the cavity. For smaller ξ_k value, it takes a longer time ($t_0 \to t_1$ is longer than $t_0 \to t_2$) for the signal to reach this level due to a much smaller initial intensity value which originates from the spontaneous emission. Thus with the same pump power, the case with lower ASE will reach higher inversion number value than that with higher ξ_k value [$\underline{N}_2(2)$ is higher than $\underline{N}_2(1)$] and thus could generate more intense pulses and shorter pulse durations.

Figure 4.11 shows dynamics of $\underline{N}_2(t)$ and $\underline{N}_2^{sa}(t)$ for pulses at pump power 10.1 W and 2.6 W with ξ_{k2}, which illustrates how the pulse energy increases with pump power in a passively Q-switched laser. At time t_0, the two pump powers achieve equal inversion densities $\underline{N}_2(t) = \underline{N}_2(0)$, which is close to the laser thresholds. $\underline{N}_2(t)$ will continue to increase due to pump power; at the same time, laser radiation becomes stronger and starts to bleach the SA. At time $t_1(t_2$ for 2.6 W pump power), the radiation power is high enough that $\underline{N}_2(t)$ reaches its maximum value and starts to decrease. As can be seen in the figure, the 10.1 W pump power can increase $\underline{N}_2(t)$ to a significantly higher value $\underline{N}_2(1)$ during period $t_0 \to t_1$ than 2.6 W pump power does, $\underline{N}_2(2)$ during period $t_0 \to t_2$; and thus generates stronger pulse and shorter pulse duration.
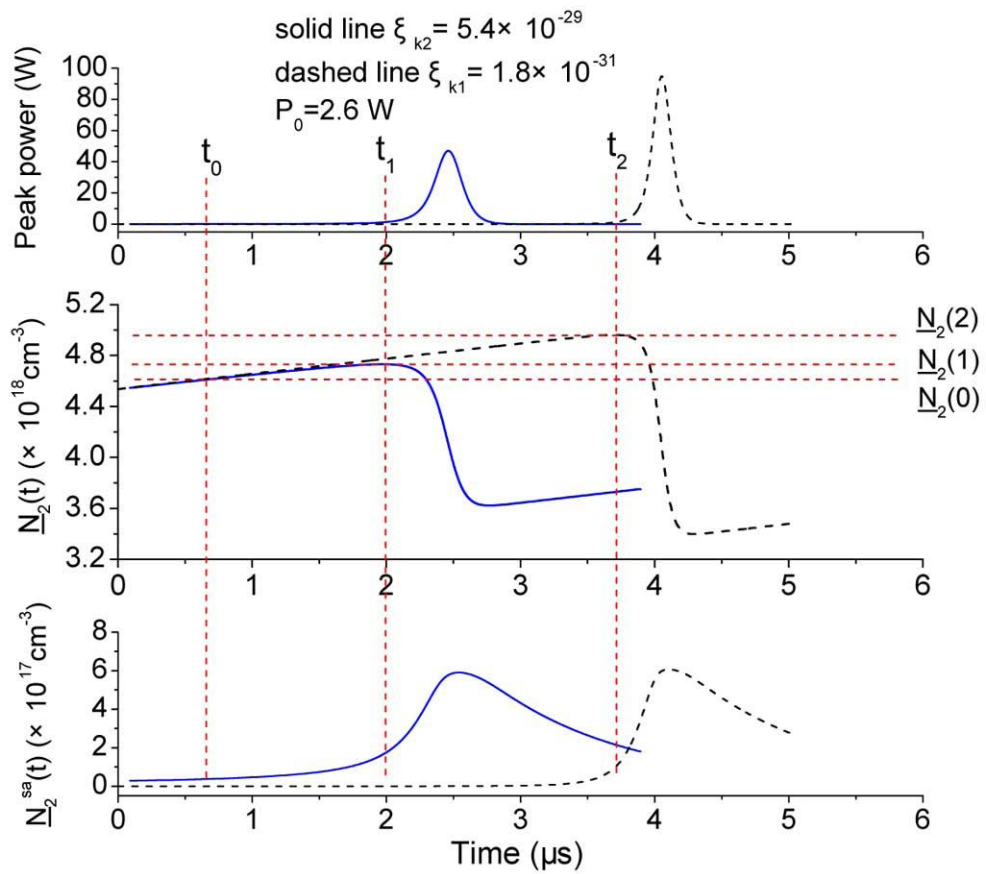
Figure 4.10: Simulated dynamics of for output pulses with different spontaneous emission intensities at a pump power of 2.6 W for Laser 1
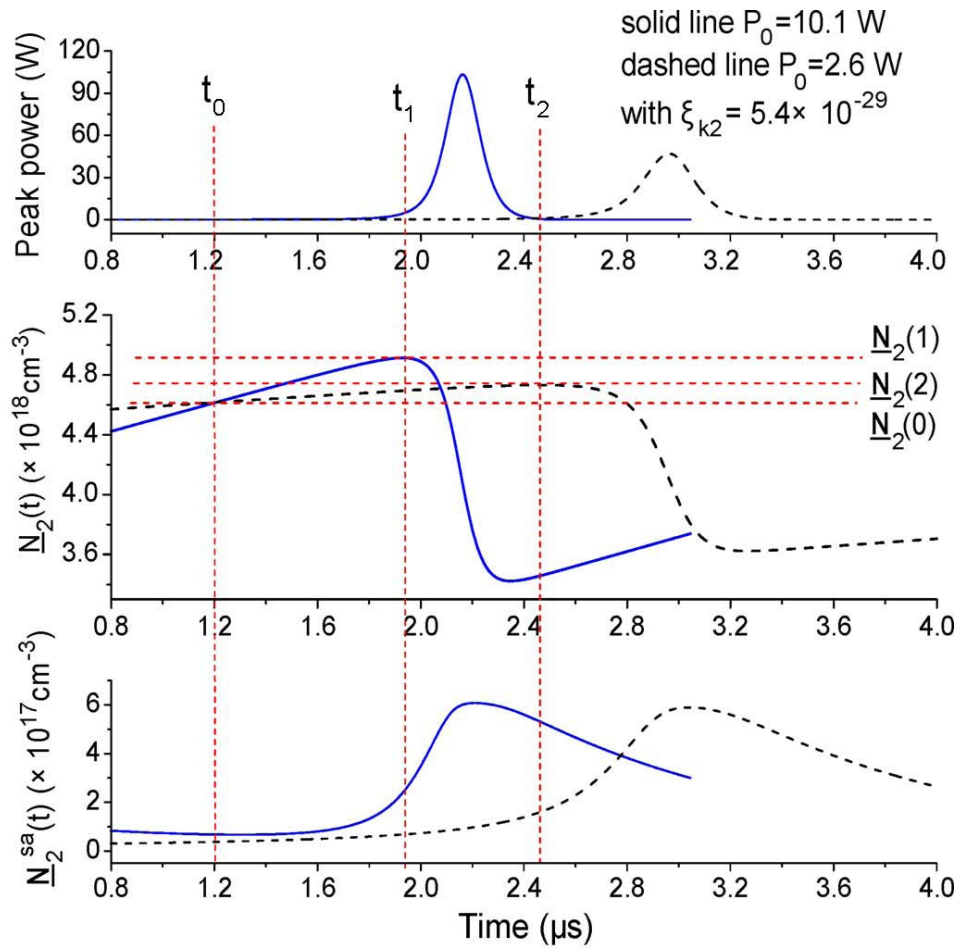
Figure 4.11: Simulated dynamics for output pulses at low and high pump powers for Laser 1.

4.6   Summary

In this chapter, two high-power and high-repetition rate passively Q-switched Yb-doped double-clad fiber lasers with Cr^{4+}:YAG SAs have been demonstrated based on small- and medium-core fibers. The laser output characteristics as a function of pump power were investigated experimentally and theoretically. Output energies of 18.4 μJ and 65 μJ were obtained with slope efficiencies of 51% and 55%, respectively. A wavelength-dependent model, including the nonuniformity of saturation in the SA was used to predict the laser spectral output characteristics. A single-wavelength model was used to simulate the Q-switched behavior. In the model, the shortening of the excited- state lifetime of Cr^{4+}:YAG due to heating of the SA was taken into consideration. Good agreement was found between the predicted and measured characteristics for both fiber laser systems if the level of ASE is assumed to be larger than the single-mode ASE within the laser linewidth. It is expected that the present model can be used to help design other passively Q-switched fiber laser systems with different SA, fiber, and operating characteristics.

Chapter 5

Two wavelength ytterbium doped fiber laser

5.1 Introduction

Multi-wavelength fiber lasers have the potential for applications in many fields such as optical communication system, laser sensors and optical instruments. The emission spectrum of Yb is also broad which allows wide wavelength tuning or multi-wavelength lasing. Normally, homogeneous gain broadening in laser gain media, such as Yb or Er doped fibers, is expected to prohibit multi-wavelength lasing in the continuous wave (CW) regime unless some techniques are employed for the wavelength selection and stabilization. Recently a few multi or two-wavelength Yb doped fiber lasers have been demonstrated, with different configurations for the wavelength selection and stabilization. These include the use of spatial mode beating in multimode fiber [18], a few-mode fiber Bragg grating (FBG) together with polarization control working as a filter [80], dual frequency generation using the birefringence of a polarization-maintaining (PM) FBG [19], dual wavelength operation using a FBG stabilized by four wave mixing [20], and a Mach-Zehnder interferometer (MZI) operating as a comb filter [81].

In this chapter, we demonstrate a free-running two-wavelength Yb fiber laser. Relaxation oscillations around 1044 nm and 1070 nm are generated directly from a Yb doped double-clad fiber without using any spectral control mechanism. The laser output characteristics are investigated as a function of pump power. A theoretical model is developed to show that the two-wavelength radiations arise from the natural peaks in the net gain curve at particular configurations of fiber length and cavity Q. The transient buildup of a free-running laser has also been simulated which is able to qualitatively explain the experimental observations. The results reported here have been published in reference [82].

5.2   Experiment setup and results

The laser configuration is shown in Figure 5.1. The gain medium is Yb doped single-mode double-clad fiber (LIEKKI Yb10/125DC) with core/inner cladding diameters (numerical aperture NA) of 10/125 μm (0.08/0.46). The fiber doping was $9.0 \times 10^{19}/cm^3$. The pump laser was a fiber coupled diode laser with CW output at 976 nm. The pump absorption of the fiber at 976 nm was 6.5 dB/m. The pump radiation was coupled into the active fiber by two collimating lenses and a dichroic mirror (DM). End-caps were put onto both ends of the fiber to avoid unnecessary reflection. The broadband high reflection mirror at the left side of the setup ensures all the emission spectra from the Yb fiber is reflected equally. Another broadband mirror with 4% reflection on the right side of the system was used as an output coupler. Two wavelength outputs were separated by a grating (1180 g/mm) and the waveforms were detected by two photodiodes and recorded by a two-channel oscilloscope. In addition the output spectra were measured in some experiments using a

78
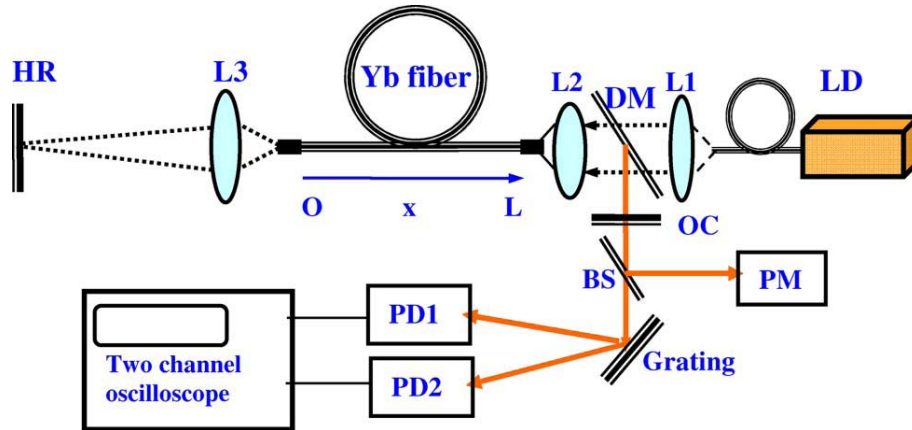
Figure 5.1: Experiment setup for two-wavelength ytterbium doped fiber laser: HR, high reflection mirror; Yb fiber, Yb doped single-mode double-clad fiber; DM, dichroic mirror; L1, L2, and L3, focusing or imaging lenses; LD, fiber coupled pump laser diode; BS, beam splitter; PD1, PD2, photodiodes; OC, output coupling mirror 4% reflection; arrow ($\rightarrow$), direction convention for distance x in the theoretical simulation.

compact spectrometer.

Different fiber lengths have been used in the experiment and two-wavelength output radiation centered at 1044 nm and 1070 nm has been observed when the fiber lengths ranged from 1.6 m to 2.0 m. It is observed that longer fiber length favors 1070 nm radiation and shorter fiber length favors 1044 nm. The two-wavelength behavior was also found to depend on the pump power. Figure 5.2 shows the variations of the two-wavelength powers and the total output power versus pump power with a fiber length of 190 cm. The power ratio of the two wavelengths was determined by measuring the first diffraction order from the grating. As can be seen in the figure, the 1044 nm output dominated in the output at a low pump power; it increased until it reached a maximum at a pump power of 7.2 W and then decreased. The 1070 nm output increased steadily with the pump power, and became dominant when the pump power was around 4 to 5 W. At a pump power of 4.8 W, an output of 0.95 W at
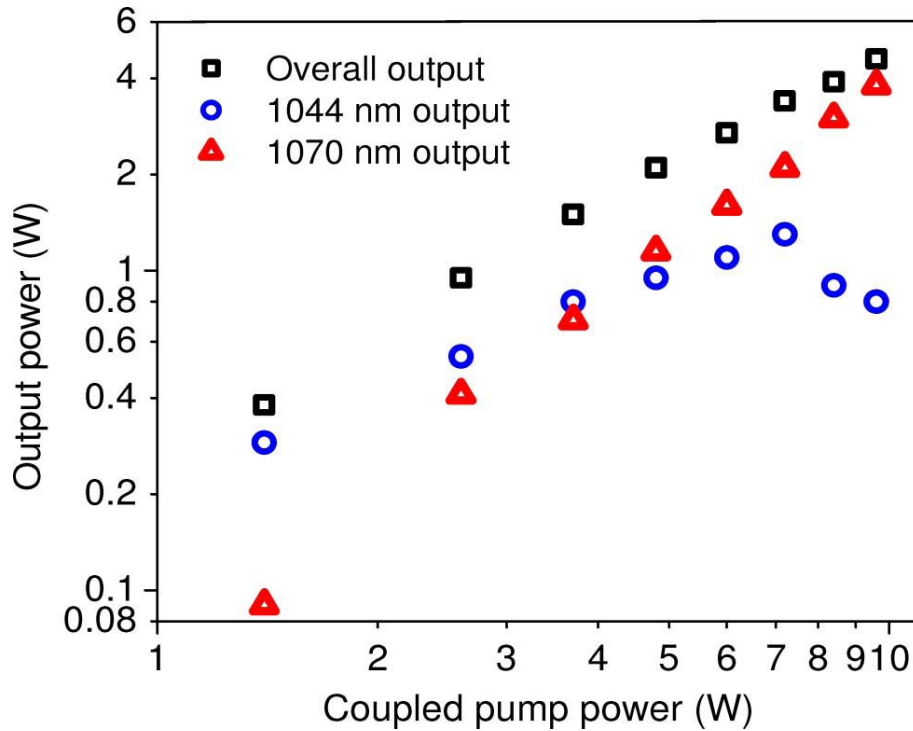
Figure 5.2: Dependences of total average power and 1044nm and 1070nm power on pump power

1044 nm and of 1.15 W at 1070 nm was obtained. Figure 5.3 shows the laser output spectra measured at low, medium and high pump power which also reflects changes in relative intensities of outputs at different pump powers. However, it should be noticed that responsivity of the silicon CCD detector in the spectrometer decreases rapidly from 1044 nm to 1070 nm, and the correct power ratio was determined from power meter readings taken of the two output wavelengths from the grating.

Figure 5.4 (a, b, c) shows the output dynamics with time at varied pump powers synchronously displayed by a two-channel oscilloscope. Rather than pure CW output, sustained relaxation oscillation pulses were observed for both wavelengths. The anti-correlated distribution of pulses indicates the two wavelengths dominated alternatively in the output. At a low pump power,
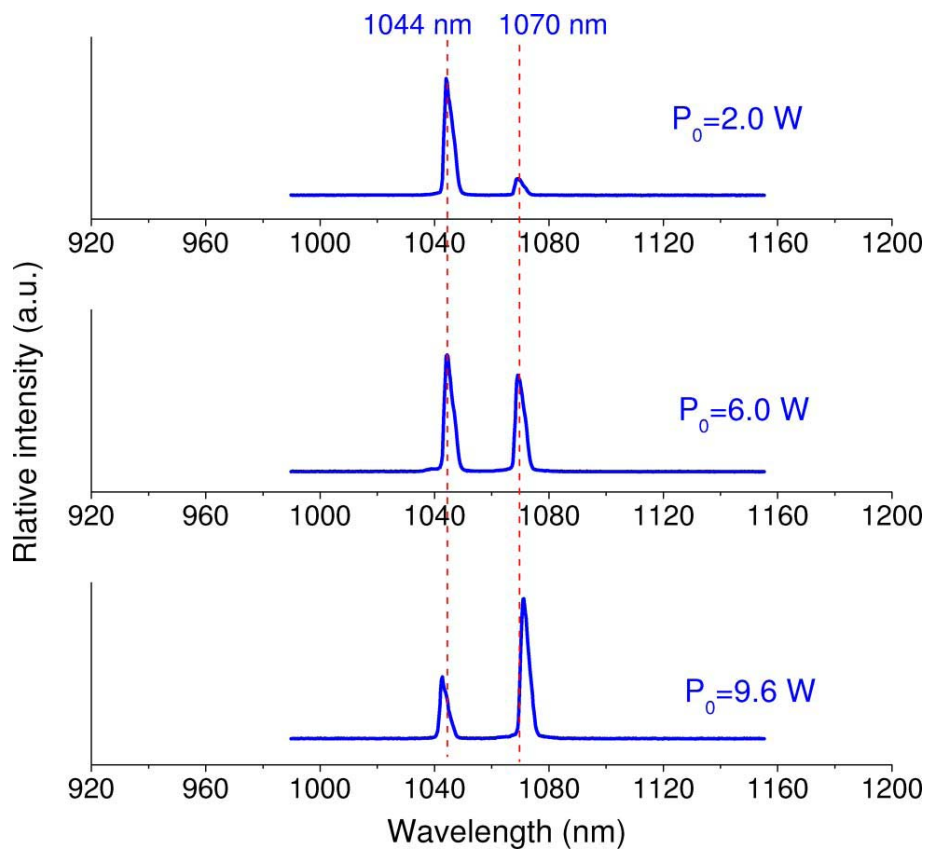
Figure 5.3: Laser output spectrum measured at different pump powers.

1044 nm output showed many more pulses than that of 1070 nm. With an increase in pump power, the number of pulses at the two wavelengths was comparable; and at a high pump power 1070 nm prevails in the competition and displayed a much higher pulse frequency.

5.3 Theoretical analysis and discussion

As a quasi-three level gain medium, the gain in Yb doped fiber strongly depends on the excitation level due to the absorption by the unpumped ions. To calculate the gain of the fiber at an instant in time, we can calculate the position averaged upper state density $\underline{N}_2(t)$ defined by Eq. 4.21. The use of spatially averaged variables is valid since the relaxation oscillation pulse duration is in the microsecond range, which is much longer than the cavity round-trip time ($\sim$20 ns). To study the frequency competition effects, numerical calculation are carried out for multiple wavelengths λ_k, across the gain profile. The round trip gain for wavelength k at time t is given by

$$g_k(t) = 2L\Gamma_k[\sigma_{ek}\underline{N}_2(t) - \sigma_{\alpha k}(N_0 - \underline{N}_2(t))] \qquad (5.1)$$

where Γ_k is the fiber core overlap factor, which is calculated with the Gaussian assumption for each wavelength, N_0 is the total Yb dopant concentration ($9.0 \times 10^{19}/cm^3$) and $\sigma_{\alpha k}, \sigma_{ek}$ are the effective absorption and emission cross sections, which are shown in Figure 3.4. Figure 5.5 shows the relative gain profile (double pass through the fiber) of the Yb fiber from 1020 nm to 1100 nm at different excitation levels. As shown in the figure, there exists two gain peaks for Yb doped fiber, with one located around 1044-1048 nm and the other around 1070-1074 nm. At lower or higher excitation levels, the longer or shorter wavelength peaks display higher gain, respectively. At a certain

82
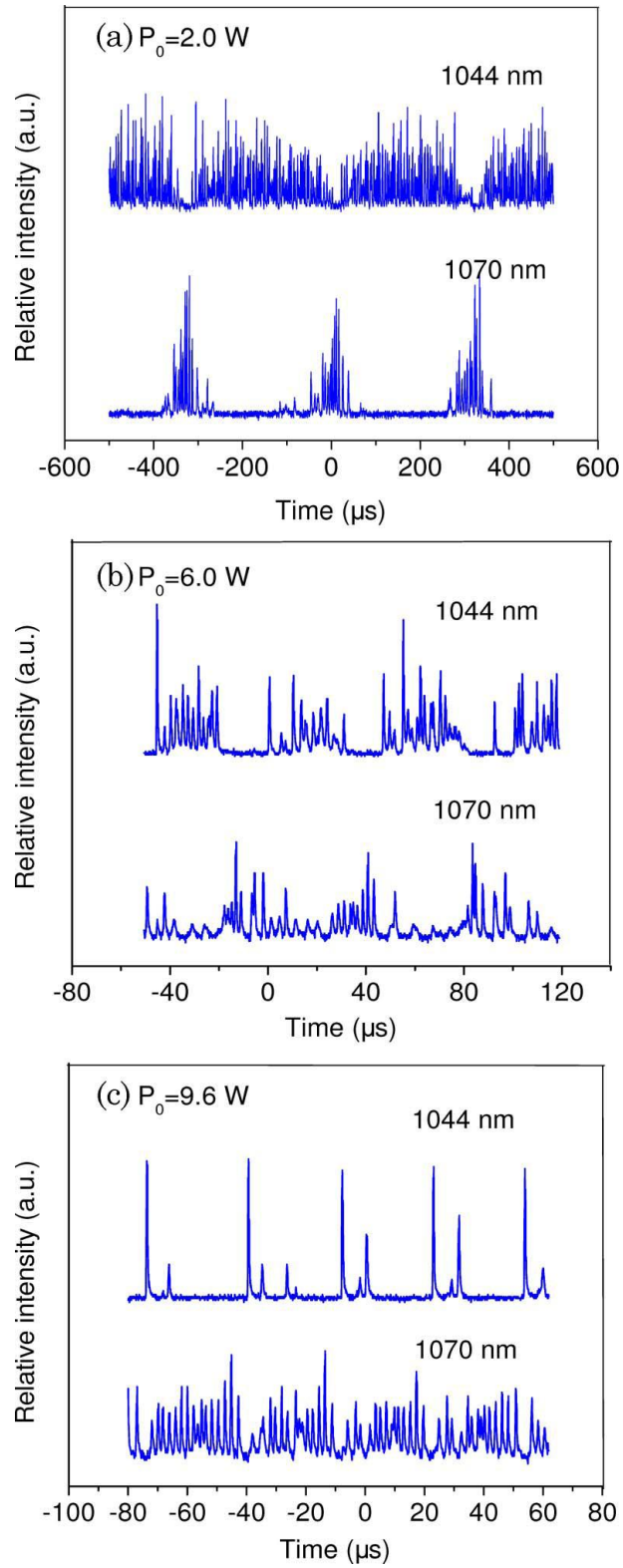
Figure 5.4: Two-wavelength output dynamics at different pump power with a fiber length of 190 cm.
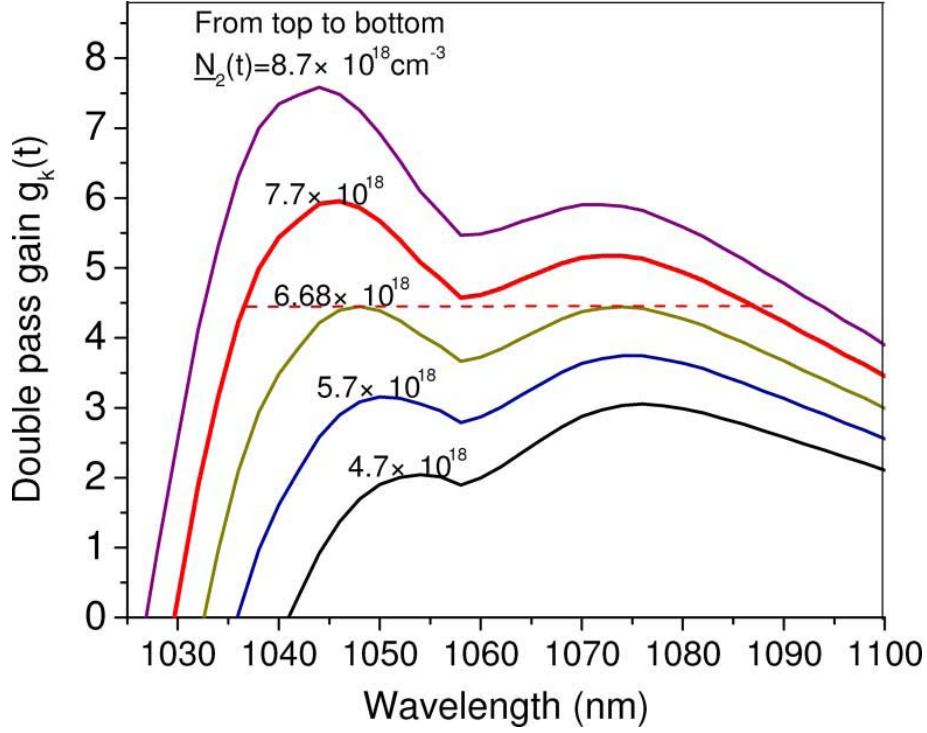
Figure 5.5: Yb fiber gain profile (net double pass gain) at different upper-state densities with an overall doping level $(9.0 \times 10^{19}/cm^3)$ L=190 cm.

intermediate level, $\underline{N}_c = 6.68 \times 10^{18} cm^{-3}$, the two peaks display almost equal gain, which can explain the simultaneous two-wavelength radiation observed in experiment.

To simulate the build up of two-wavelength radiation and position depen-dant population densities, we have used the rate equations including multi-wavelength emission

$$N_0 = N_1 + N_2 \tag{5.2}$$

$$\frac{\partial N_2}{\partial t} = \frac{\Gamma_p \lambda_p}{hcA_{co}}[\sigma_{\alpha p}N_1 - \sigma_{ep}N_2]P_p^- + \sum_k \frac{\Gamma_k \lambda_k}{hcA_{co}}[\sigma_{\alpha k}N_1 - \sigma_{ek}N_2](P_k^+ + P_k^-) - \frac{N_2}{\tau} \tag{5.3}$$

$$-\frac{\partial P_p^-}{\partial x} + \frac{1}{v_p}\frac{\partial P_p^-}{\partial t} = \Gamma_p[\sigma_{ep}N_2 - \sigma_{\alpha p}N_1]P_p^- - \alpha_p P_p^- \tag{5.4}$$

$$\pm\frac{\partial P_k^\pm}{\partial x} + \frac{1}{v_k}\frac{\partial P_k^\pm}{\partial t} = \Gamma_k[\sigma_{ek}N_2 - \sigma_{\alpha k}N_1]P_k^\pm - \alpha_k P_k^\pm + 2\Gamma_k\sigma_{ek}N_2\frac{hc^2}{\lambda_k^3}\Delta\lambda_k$$
$$k = 1,...,K \tag{5.5}$$

where N_0 is the total Yb dopant concentration (Provided by LIEKKI); N_1 and N_2 are ground and excited number densities. $P_k^\pm$ are the forward and backward propagating laser radiation power for emission wavelength k. For the emission spectra, we have included K=51 lines from 1000 nm to 1100 nm with $\Delta\lambda$=2 nm separation each. $\sigma_{\alpha p}, \sigma_{ep}, \sigma_{\alpha k}, \sigma_{ek}$ are the absorption and emission cross sections of Yb ion at the pump wavelength and each emission wavelength, respectively. Seeding of the emission comes about from the ASE emission term included as the last term in Eq. 5.5. v_p and v_k are the pump and emission group velocities and both set to c/n, where c is the speed of light in vacuum, n is the fiber refractive index ($\sim$1.5); h is Planck constant, τ is the lifetime of Yb ($\sim$850μs), and $\alpha_{p(k)}$ is the fiber attenuation coefficient at the pump (emission) wavelength ($\sim$0.005/m). The equations are numerically solved under the boundary conditions given by

$$P_p^-(L) = P_0 \tag{5.6}$$

$$P_k^-(L,t) = P_k^+(L,t)R_{oc} \tag{5.7}$$

$$P_k^+(L,t) = P_k^-(0,t)(1-\eta)^2 \tag{5.8}$$

where η is the one way cavity loss, was estimated to be $\sim$15% loss due to Fresnel reflection of the end-caps, lens coupling and coatings.

Figure 5.6 shows the evolution of the output spectra for different fiber lengths as a function of time from turn on of the pump (P_0=6 W) to the start of the relaxation oscillation ($\sim$32 to 33 μs). During most of the time of this period, the inversion density is below the threshold and there is no actual lasing. There are two emission peaks centered at 1048 nm and 1074 nm, respectively. With an increase of the inversion density, the spontaneous emission is amplified exponentially and the two peaks become narrower and narrower. The evolution is very sensitive to fiber length; two-wavelength emission only occurs when the fiber length was around 157 cm in the simulation as shown in Figure 5.6 (b). For shorter and longer fiber lengths (taking 145 cm and 165 cm as examples shown in Figure 5.6 (a) and (c)), one peak will gradually be suppressed and single wavelength radiation will be generated. Longer fibers favor 1074 nm and shorter fibers prefer 1048 nm which agrees with the experimental observations. The difference between the measured and predicted peak wavelengths may be due to minor discrepancies between the spontaneous emission and absorption cross sections used in the simulations as compared to the real fiber. In addition, the slight wavelength dependence of optical coatings might be another factor, since it is not included in the simulation.

Dual wavelength operation was obtained in a broader range of fiber lengths in the experiment, 1.6 m-2.0 m, than that predicted by the simulation, which was only in a narrow range around 1.57 m. However, the simulation still does not model all the relevant physics including intraband relaxations, transient heating effects, fiber nonlinearities and partial inhomogeneous broadening in the Yb doped fiber [10], which will favor multi-wavelength generation over a broader range.

Figure 5.7 shows the simulated dynamics of the two-wavelength relaxation

86
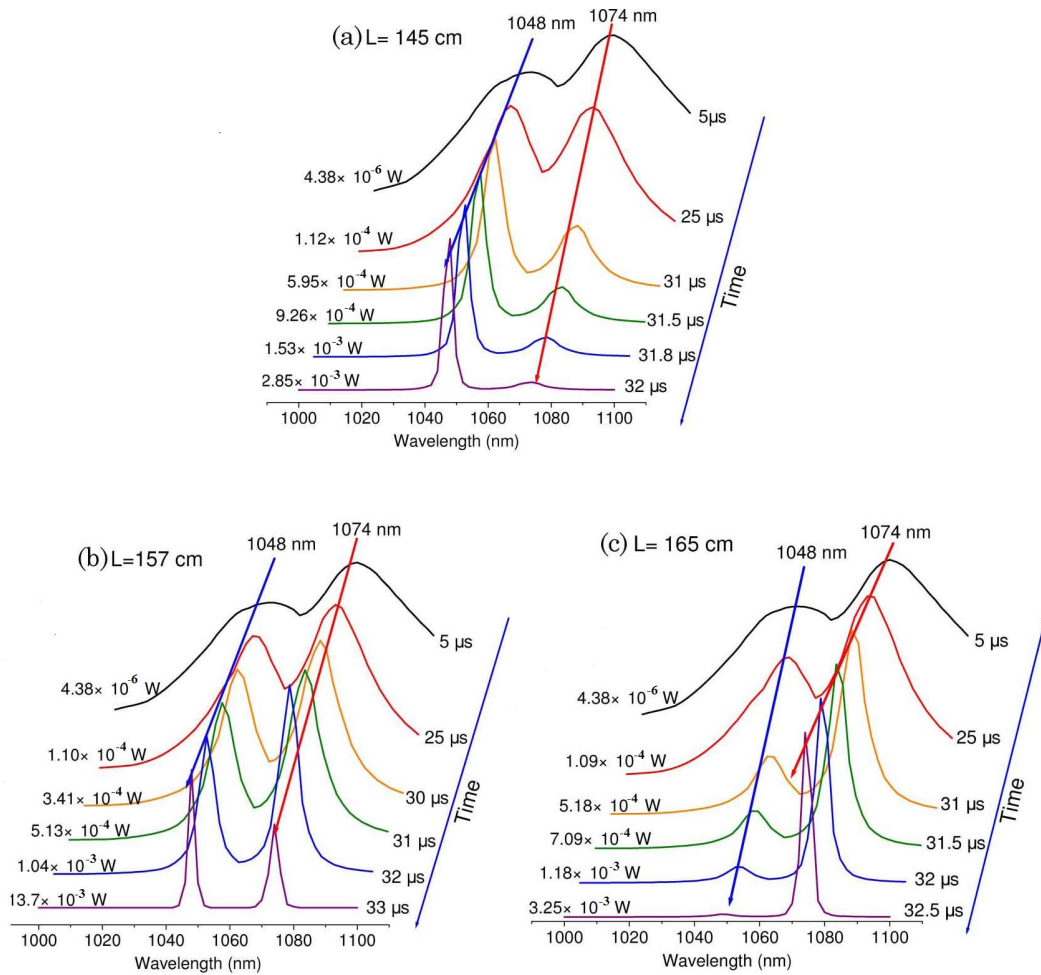
Figure 5.6: Simulated evolution of the amplified spontaneous emission spectrum during the early time start of the free-running relaxation oscillation for different fiber lengths at pump powers of 6 W: (a) 145 cm, (b) 157 cm, (c) 165 cm. The output power at each time is marked at the left side of the curve, and the intensities have been normalized by the 1048 nm or 1074 nm peak for convenience of viewing.

oscillations and the inversion density $\underline{N}_2(t)$ for the case described in Figure 5.6 (b). The radiation always starts with a strong 1048 nm pulse when $\underline{N}_2(t)$ is at a relatively high level at the beginning; then 1074 nm pulses start to be stronger and dominate in the output as $\underline{N}_2(t)$ decreases. The oscillation decreases in time and one wavelength gradually suppresses the other. This results in single wavelength CW operation and the wavelength is determined by the level of steady-state inversion density $\underline{N}_{ss}$ as shown in the figure by a dashed line. In this case $\underline{N}_{ss} = 6.70 \times 10^{18} cm^{-3}$, which is slightly higher than $\underline{N}_c = 6.68 \times 10^{18} cm^{-3}$, so that 1048 nm radiation will eventually again suppress 1074 nm radiation and finally dominate in the CW output. The anti-correlated dynamics shown in the two-wavelength relaxation oscillation output in Figure 5.6 agree well with the experimental observations. However in the experiment, free-running did not end up as single wavelength CW output and the oscillation was observed constantly. Therefore there must be other instabilities that have not been included in the simulation.

Recently, self-pulsing in Yb doped fiber lasers has been investigated intensively [50, 83–86]. Besides external perturbations such as pump fluctuation, other mechanisms that may cause instability of the laser include the reabsorption by the unpumped part of the fiber at relatively low pump power [83, 84], nonlinear scattering losses such as Rayleigh scattering and stimulated Brillouin scattering (SBS) for high loss cavity or high pump power case [50, 85], and ion pairs in highly doped fiber that may work as saturable absorbers [86, 87]. Further investigations are required to clearly identify the dominant mechanisms that may be causing the sustained relaxation oscillation in the real laser system. As shown in Figure 5.3, the spectrum is relatively broad (FWHM 3-4 nm) and the instantaneous emission wavelength may shift within the bandwidth.
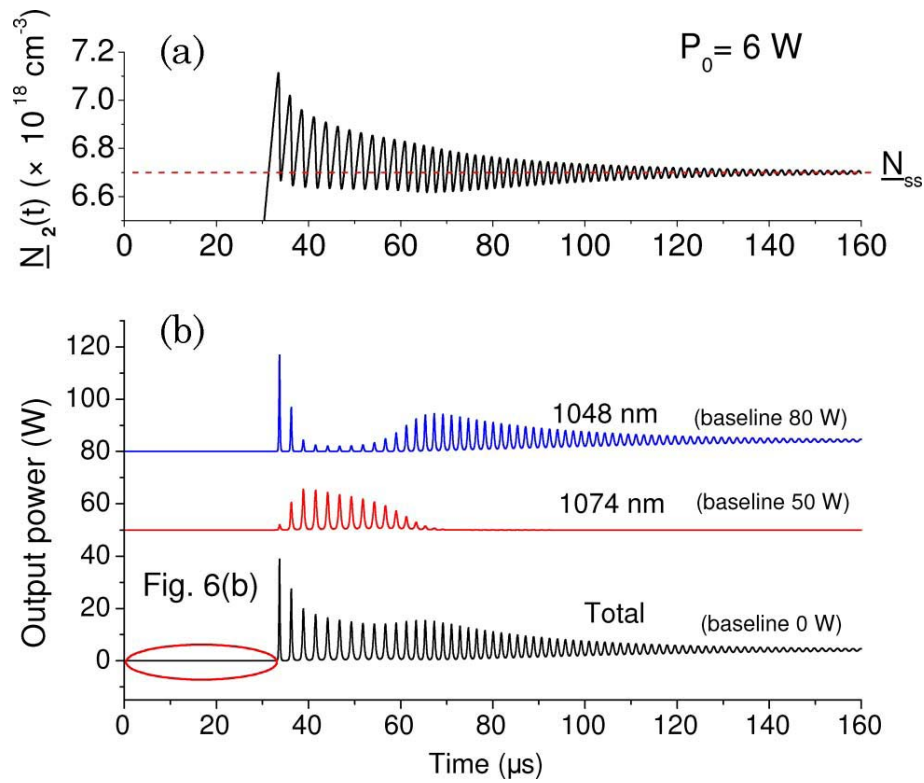
Figure 5.7: Simulated (a) upper-state population density and (b) two-wavelength relaxation oscillations and inversion number dynamics for a fiber length 1:57 m and a pump power 6 W; the baselines for 1048nm and 1074nm output have been shifted as shown.

Such wavelength instability has been reported in a Yb doped ceramic laser [88]. A more complete model would require considering the partial inhomogeneous broadening, relaxation dynamics within the upper and lower manifolds and thermal heating effects.

Figure 5.8 (a) shows the two-wavelength output dynamics at a pump power of 10 W. Compared with that in Figure 5.7, the intensity of 1048 nm oscillation increases with pump power due to the higher $\underline{N}_2(t)$ achieved by higher pump at the very beginning of the lasing ($7.19 \times 10^{18} cm^{-3}$ compared with $7.13 \times 10^{18} cm^{-3}$), which is contrary to the experimental observations that higher pump power favors 1070 nm radiation. Possible explanations might be due to the temperature increase of the fiber core at high pump power. The temperature dependence of effective emission and absorption cross sections of Yb doped fibers have been studied and it was observed that increased long wavelength lasing was expected at high temperatures [89,90] due to increased thermal population in the various levels of the lower state manifold. To investigate effects of the small change of the effective cross section on two-wavelength output, we repeated the simulation by increasing the emission cross section of 1074 nm only 0.1% and keeping that of 1048 nm unchanged. Figure 5.8 (b), the intensity of 1074 nm output is significantly improved compared with that in Figure 5.8 (a), which shows that the two-wavelength competition is very sensitive to the relative emission cross sections. The increase of 1074 nm output with pump power might due to the tiny changes of effective cross sections of the fiber at higher temperature induced by higher pump power, which dominates over the slightly increased upper state population.
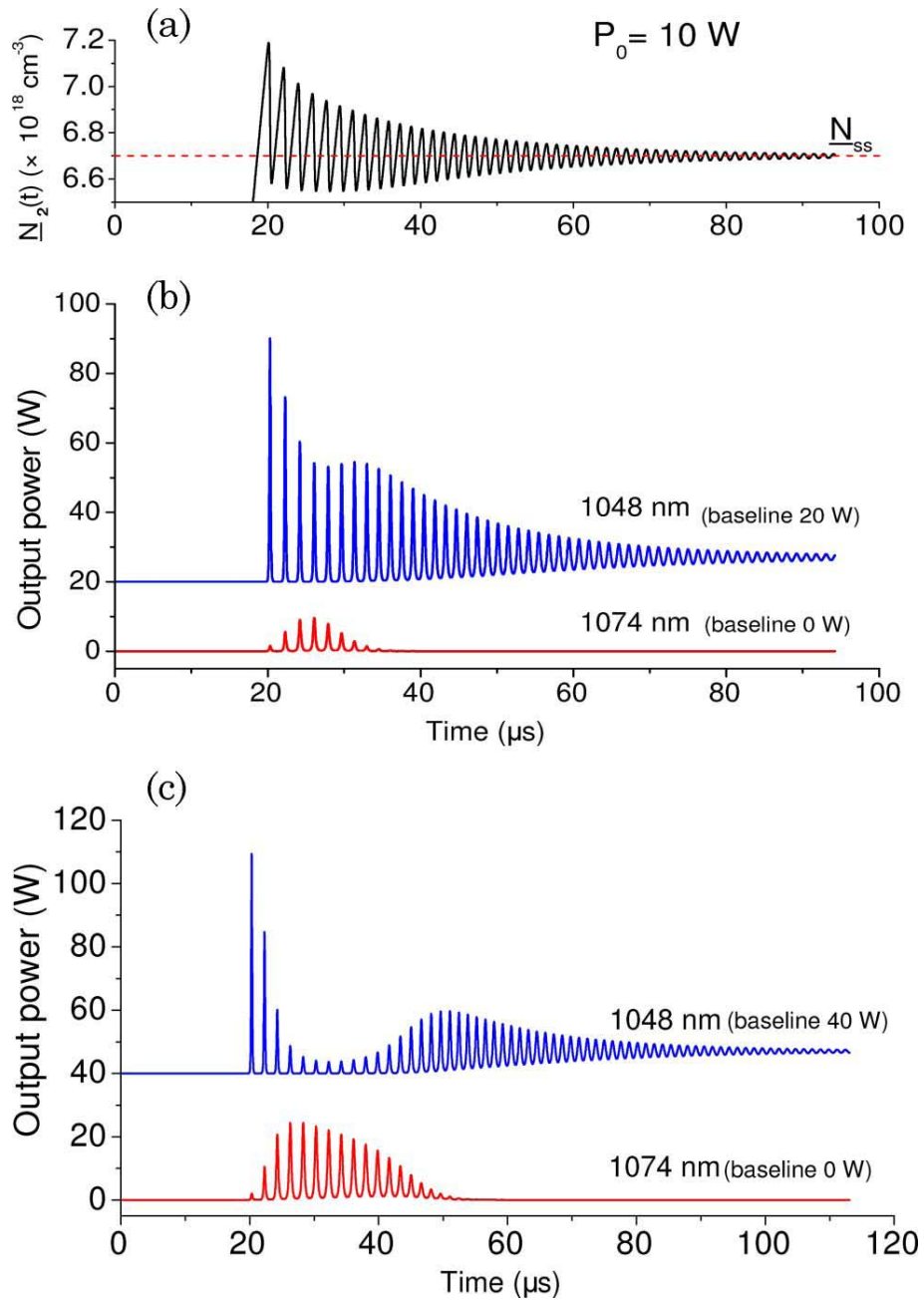
Figure 5.8: Simulated (a) upper-state population density, (b) two-wavelength relaxation oscillations and (c) two-wavelength relaxation oscillations with emission cross section of 1074nm radiation increased by 0.1%; fiber length 1.57 m and pump power 10 W; the baselines for 1048nm and 1074nm output have been shifted as shown.

91

5.4 Summary

A high power, free-running Yb doped fiber laser operating at two wavelengths has been demonstrated. The output showed sustained relaxation oscillation with anti-correlated dynamics for the two wavelengths. The gain profiles of Yb fiber at different excitation levels was calculated and the two-wavelength generation is demonstrated to be due to two equal gain peaks of Yb fiber under particular pump conditions. The current theoretical simulation could qualitatively reproduce the simultaneous existence of two gain peaks at two wavelengths and anti-correlated relaxation oscillations at the two wavelengths during a transient build up phase. A more quantitative model is required for further clarification of the continuous self-pulsing mechanisms. Such a model should take into account the partial inhomogeneity of the fiber gain medium, transitions within manifolds and thermal heating effects which would effect the laser dynamics.

Chapter 6

Dynamics of two-wavelength passively Q-switched ytterbium doped fiber laser

6.1 Introduction

In the last chapter, a free-running two-wavelength Yb doped double-clad fiber laser has been demonstrated. In many cases, Q-switched multi-wavelength lasers operating at high peak power are of interest for applications such as laser micro-machining and laser sensing. Hu et. al. [21] reported a dual wavelength nanosecond Yb doped fiber laser based on the mechanism of stimulated Brillouin scattering (SBS) induced self-Q-switching. The two wavelengths 1109.6 nm and 1127.6 nm were reportedly due to the birefringence in the fiber and the pulse energy was relatively low ($\sim$nJ) in this case. In this chapter we present a high power multi-μJ two-wavelength passively Q-switched Yb fiber laser based on a Cr^{4+}:YAG saturable absorber (SA). Similar to the free running in last chapter, the two-wavelength Q-switched outputs centered at 1040 nm and 1070 nm were generated directly from the setup. A theoretical model is developed to simulate the dynamics of two-wavelength Q-switched operation, which gives qualitative agreement with the experimental observations.

The results have been published in reference [91].

6.2   Experiment setup and results

The experiment setup is shown in Figure 6.1, which is updated from the setup in 5.1 by inserting a Cr^{4+}:YAG crystal as SA. Lenses 3 and 4 were used to focus the laser through the SA (T_0=30% at 1064 nm) with a focal spot diameter of $15\mu m$. A diffraction grating (1180 g/mm) was used for spectral separation of the laser output. To detect the dynamics of the two wavelength output two fast photodiodes were placed at a distance of 2 m from the grating where the spectrum displayed two well separated peaks. Each photodiode was centered on the corresponding peak and connected to a two-channel digital oscilloscope

During operation two output wavelength components were observed as shown in Figure 6.2. The dependency of the average output power at 1040 nm and 1070 nm and the total output power on pump power was measured with a power meter and is shown in Figure 6.3. Two-wavelength emissions appeared when the pump power was 3.5 W or higher; below this power, only one output wavelength at 1040 nm existed. The spectral positions of two-wavelength peaks were stable with pump power, with a minor shift of the short wavelength peak from 1040 nm to 1042 nm when the pump power increased up to 9.9 W. A total output power of 4.2 W was obtained at a pump power of 9.9 W, with a slope efficiency of 44%. The ratio of average power at the two wavelengths was determined by measuring the two beams in the first diffraction order from the grating. As can be seen in the figure, the 1040 nm power at first increased with the pump power; reached a maximum at a pump power of 7.8 W and then decreased. The 1070 nm output increased steadily with the pump power. It is also expected that higher cavity Q will favor 1070 nm output since lower

94

population inversion is required with the peak gain shifting to 1070 nm. An indication of this can be observed by comparing Figure 6.3 with Figure 5.2 in Chapter 5, in which 1070 nm became dominant at a much lower pump power of ~4-5 W due to the higher cavity Q when the saturable absorber was removed.
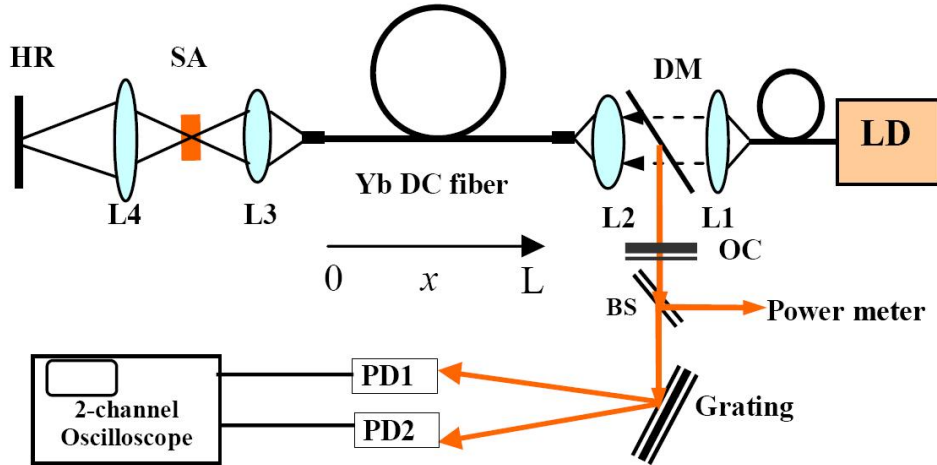
Figure 6.1: Experiment setup for two-wavelength passively Q-switched fiber laser.

At a pump power of 4.5 W, the pulse trains for both wavelengths exhibited a period doubled behavior; a big-small 1040 nm pulse pattern was accompanied with a big-small 1070 nm pulse pattern, as shown in Figure 6.4 (a). The average powers for 1040 nm and 1070 nm were 1.4 W and 0.4 W; and pulse durations (Figure 6.4 (b)) were about 100 ns and 300 ns, respectively. At this pump power, the 1040 nm emission dominates in the wavelength competition, experiencing higher gain, and achieving higher pulse energy and shorter pulse duration. As also can be seen in Figure 6.4 (b), the 1070 nm pulse was 500 ns later than 1040 nm pulse.

With an increase in pump power, the output at 1070 nm increased significantly; the big-small and big-small pulse patterns became unstable and changed to big-small small-big patterns for the two wavelengths respectively:
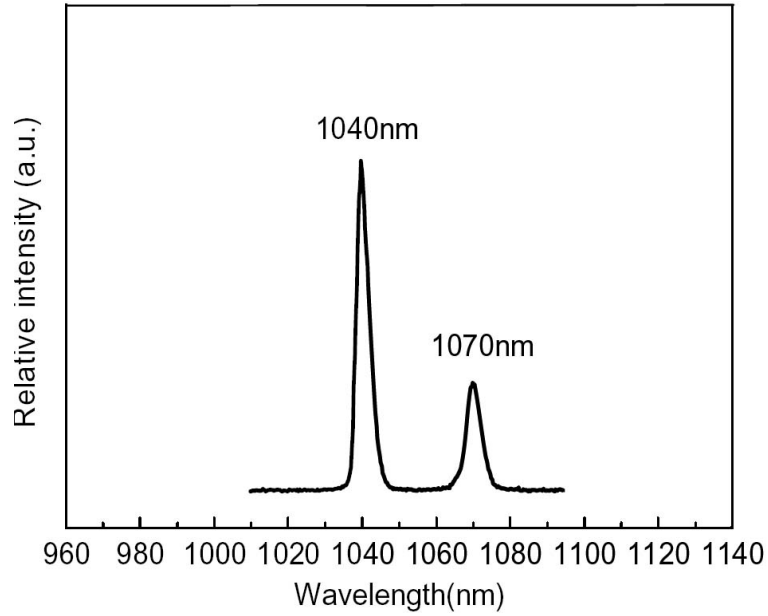
Figure 6.2: Laser output spectrum measured by a compact spectrometer (Ocean-Optics with resolution 1.5 nm) at a pump power of 7.8 W; the low peak height at 1070 nm is due to the rapidly decreasing responsivity of the silicon based spectrometer CCD at this wavelength.
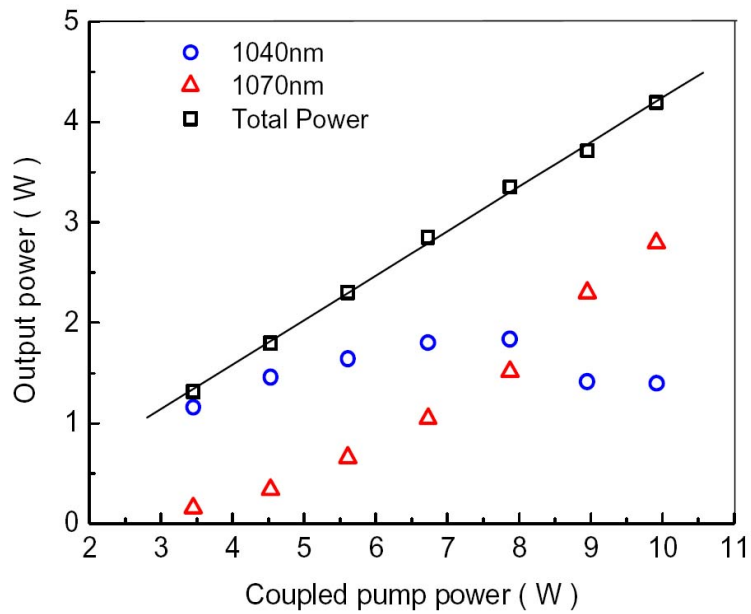
Figure 6.3: Dependencies of total average power, 1070 nm, and 1040 nm power on pump power.

a strong 1040 nm pulse was accompanied with a weak 1070 nm pulse, and vice versa. At a pump power of 7.8 W, the weak pulse almost disappeared in the pattern and the two-wavelength pulses appeared alternatively. The 1040 nm pulse train still exhibited period-doubled shape and the 1070 nm pulse train was stable, as shown in Figure 6.5 (a). Average outputs of 1.8 W and 1.5 W have been obtained for 1040 nm and 1070 nm, with a pulse repetition rate of 32 kHz and average pulse energies of 56 μJ and 47μJ. Under this condition the pulse durations were same with a duration of 105 ns, leading to peak powers of the two-wavelength pulses of 533 W and 448 W, respectively. At this pump power, the two wavelengths achieved a balance in competition in gain and dominated alternatively with every second pulse. With further increase in the pump power, the output at 1070 nm increased further and the pulse pattern became more complicated. A new stable pattern was formed at a pump power of 9.9 W; in this case period-2 for 1040 nm and period-6 for 1070 nm output was observed, as shown in Figure 6.5 (b). The dual wavelength operation also depended on fiber length; longer fibers would lase primarily around 1070 nm while shorter fibers would lase around 1040 nm. However similar behavior was observed for fibers with approximate lengths from 1.6 m to 2.0 m.

6.3 Theoretical simulation and discussions

To understand this behaviour, we have theoretically simulated the Q-switched operation using a multi-wavelength model. Eq. 5.2 to Eq. 5.5 are used to describe the Yb doped double clad fiber. For Cr^{4+}:YAG SA, we have used a point model [65]

$$N^{sa} = N^{sa}_1 + N^{sa}_2 \tag{6.1}$$
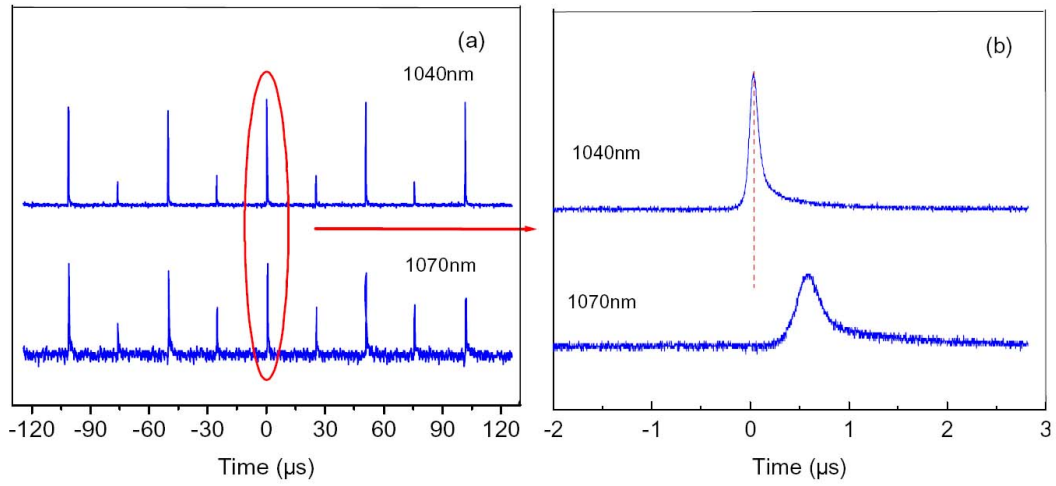
Figure 6.4: Synchronized (a) pulse trains and (b) pulse shapes of the output at the two wavelengths for a pump power of 4.5 W, the dashed line marks the peak of 1040 nm pulse. The intensity of 1070 nm pulse has been amplified for convenience of viewing.
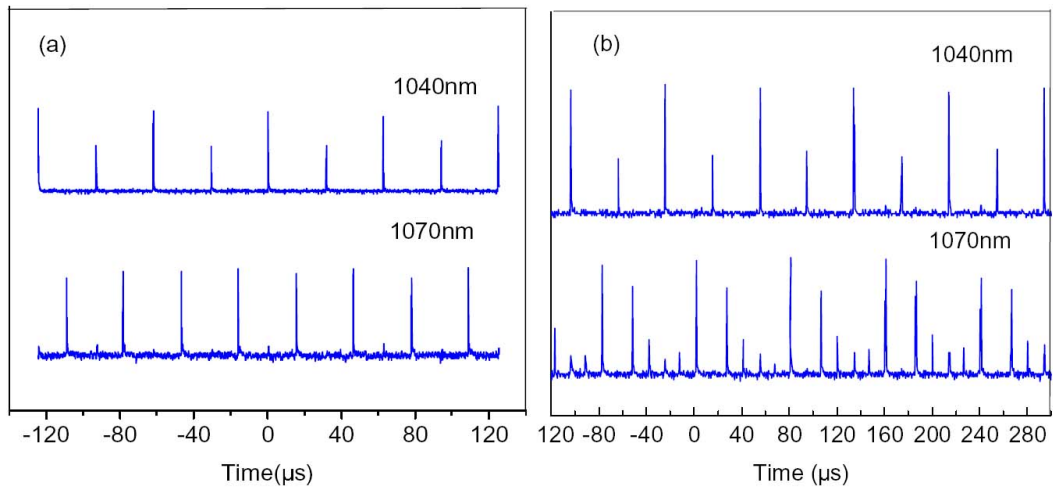
Figure 6.5: Synchronized pulse trains at a pump power of (a) 7.8 W (b) 9.9 W.

$$T_k(t) = exp[-2L_{sa}(\sigma_{gsak}N_1^{sa} + \sigma_{esak}N_2^{sa})] \tag{6.2}$$

$$\frac{dN_2^{sa}}{dt} = \sum_k \frac{P_k^+(0,t) + P_k^-(0,t)}{2} \frac{\lambda_k}{A_{sa}hc}\sigma_{gsak}N_1^{sa} - \frac{N_1^{sa}}{\tau_{sa}} \tag{6.3}$$

where N_{sa} is the total ion doping, N_1^{sa} and N_2^{sa} are the ground and excited level number intensities; $T_k(t)$ is the instantaneous two way transmission of the SA, and σ_{gsa}, σ_{esa} are the ground-state and excited-state-absorption cross sections, respectively. L_{sa} is the thickness of the SA (4.5 mm). A_{sa} is the focal spot area on the SA; τ_{sa} is the lifetime of the excited state. N_{sa} was calculated based on L_{sa}, initial transmission $T_0 = 30\%$ and $\sigma_{gsa} = 4.3 \times 10^{-18}cm^2$ at 1064 nm. T_0 was measured to be 26% at 1040 nm and 35% at 1070 nm, so σ_{gsa} can be estimated at the two wavelengths. For the ratio of $\sigma_{gsa}/\sigma_{esa}$, we have used 6 and 4 for 1040nm and 1070 nm as approximate values [74]. Because the SA is relatively thick and the focused beam was not uniform in the SA; the positions far from the focal spot may not be well saturated and thus would contribute towards the non-saturable loss rather than acting as a saturable absorber. In the simulation we have used L_{sa} =3.5 mm and an averaged focal spot diameter $d_{sa} = 70\mu m$ to represent the central region of SA where the saturation is expected.

The above equations are solved under the boundary conditions given by

$$P_p^-(L) = P_0 \tag{6.4}$$

$$P_k^-(L,t) = P_k^+(L,t)R_{oc} \tag{6.5}$$

$$P_k^+(0,t) = P_k^-(0,t)(1-\eta)^2 T_k(t) \qquad (6.6)$$

where P_0 is the pump power, L is the fiber length, R_{oc}=0.04 is the reflectivity of the output coupler, η is the loss at the high reflector end ($\sim$15% one way) due to the non-saturable loss of the saturable absorber, Fresnel reflection from the end-cap, coating loss and lens coupling loss, etc. The values of parameters used in simulation are shown in Table 6.1.

Table 6.1: Values of parameters in simulation

Parameters	Values	Parameters	Values
N_0	$9 \times 10^{19}/cm^3$	τ	$850\mu s$
$\sigma_{e1040nm}$	$5.86 \times 10^{-21}cm^2$	$\sigma_{e1070nm}$	$2.47 \times 10^{-21}cm^2$
$\sigma_{\alpha1040nm}$	$3.34 \times 10^{-22}cm^2$	$\sigma_{\alpha1070nm}$	$2.51 \times 10^{-23}cm^2$
Γ_{1040nm}	0.811	Γ_{1070nm}	0.799
$\alpha_{p(k)}$	$0.005m^{-1}$	Γ_p	0.064
N^{sa}	$6.2 \times 10^{17}/cm^3$	τ_{sa}	$4\mu s$
$\sigma_{gsa1040nm}$	$4.8 \times 10^{-18}cm^2$	$\sigma_{gsa1070nm}$	$3.8 \times 10^{-18}cm^2$

The simulation results show that the two emission wavelengths can co-exist in the Q-switched operation; the ratio of the power between two wavelengths depended on the fiber length and pump power; long fibers and higher pump will favour 1070 nm radiation. We have fixed the fiber length L=190 cm and investigated the Q-switching characteristics at different pump powers, which are shown in Figure 6.6 (a-f). At a pump power of 5 W, the 1040 nm dominates in the output, achieving much higher peak power ($\sim$560 W compared with $\sim$5 W). With an increase of pump power to 8 W, the 1070 nm wavelengths observes higher gain and starts to induce instabilities to the pulse train: an alternative big-small pulse pattern starts to be evident. At a pump power of

11 W, the weak pulse almost disappears in the big-small pattern, and the two wavelengths appear alternatively, which is similar to the experimental results shown in Figure 6.5 (a). With further increase to a pump power to 18 W, the pulse intensities return to constant values; the 1070 nm wavelength dominates the output and achieves higher peak power ($\sim$580 W compared with $\sim$115 W for 1040 nm). The time delay of 1070 nm pulse to 1040 nm pulse is shown in Figure 6.6 (b) and 6.6 (f). The output at 1040 nm precedes the output at 1070 nm similar to that measured experimentally as shown in Figure 6.4 (b).

Since the Yb ion inversion number is changing with time and position in the fiber, we can define a position averaged inversion number density $\underline{N}_2(t)$ defined by: Eq. 4.21. The two-way signal gain (loss) for each wavelength with fiber and SA at an instantaneous time can be estimated as

$$g_k(t) = 2L\Gamma_k[\sigma_{ek}\underline{N}_2(t) - \sigma_{ek}(N_0 - \underline{N}_2(t))] - ln[1/T_k(t)] \qquad (6.7)$$

With a relatively larger σ_e, there is higher gain at 1040 nm when $\underline{N}_2(t)$ is higher; also with much smaller σ_e, the lasing threshold for 1070 nm is lower: $\underline{N}_{2\ 1070}^{th} < \underline{N}_{2\ 1040}^{th}$. Thus there exists a critical value $\underline{N}_2^c$ above which $g_{1040nm} > g_{1070nm}$ and below which $g_{1070nm} > g_{1040nm}$. At an early stage of each pulse when $\underline{N}_2(t)$ is its maximum $(\underline{N}_2^0)$, $g_{1040nm} > g_{1070nm}$; the 1040 nm wavelength pulse can build up and bleach the SA more quickly, and lead to emission at 1040 nm early in time. With the decrease of $\underline{N}_2(t)$ throughout the pulse to $\underline{N}_2^c$, higher gain is observed at 1070 nm sometime later during the pulse. With lower threshold, the 1070 nm wavelength continues to see gain even after the 1040 nm wavelength is no longer amplified. Thus the 1070 nm pulse can deplete $\underline{N}_2(t)$ to a deeper final level $\underline{N}_2^f$, which explains why the 1070 nm pulse could lase well after 1040 nm pulse, as shown in Figure 6.4 (b) and Figure 6.6 (b, f). Figure 6.7 shows an example of how the inversion number along the

101
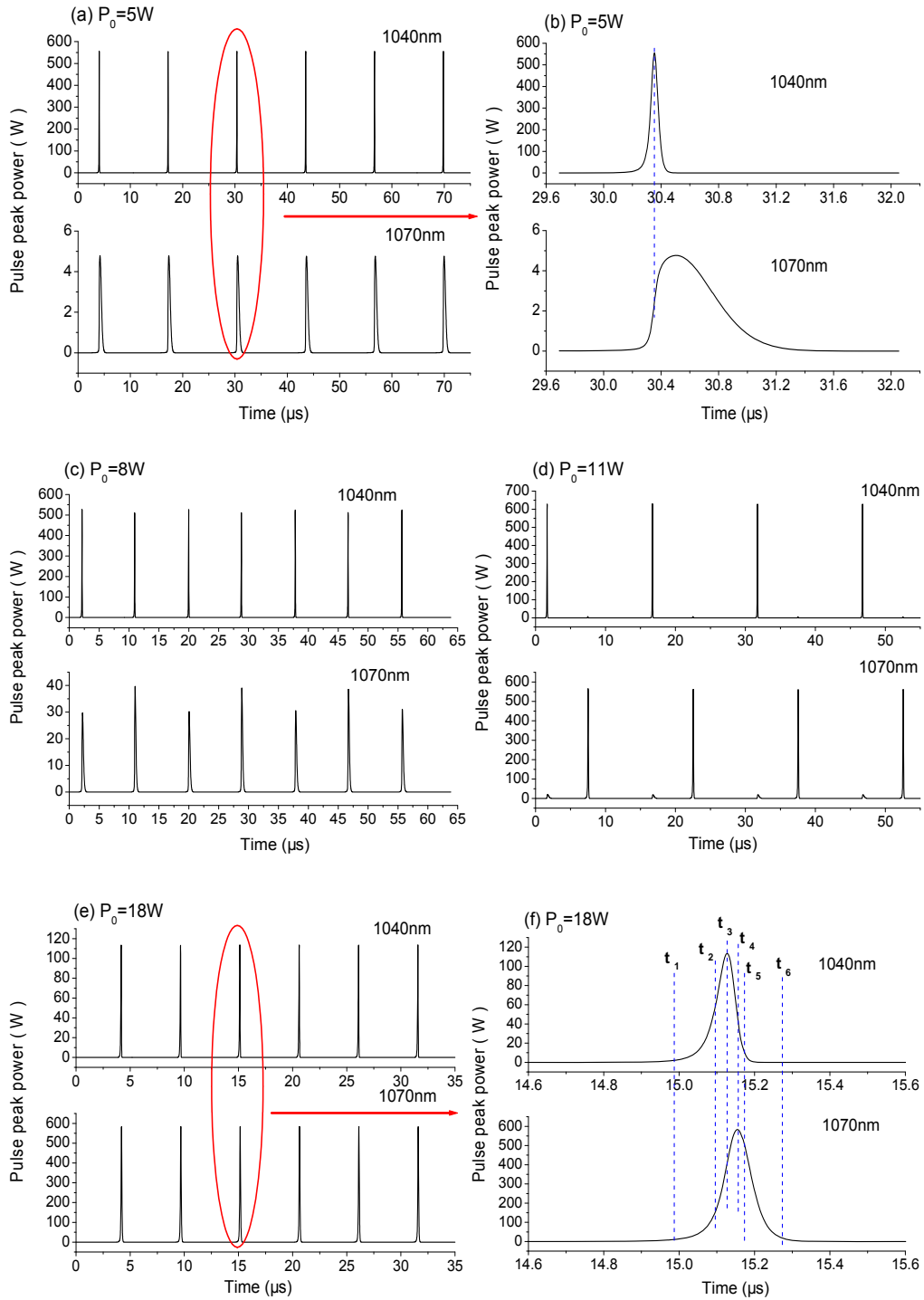
Figure 6.6: Simulated Q-switched pulse trains and shapes at different pump powers P_0, fiber length L= 190 cm; (b) the dashed line marks the peak of 1040 nm pulse; (f) t_1 to t_6 mark different times through the pulse at a pump power of 18 W, which are explained in Figure 6.7. Note each plot uses different vertical scale.

102

length of fiber changes during the stages discussed above for a pump power of 18 W; the times t_1 to t_6 are defined in Figure 6.6 (f). As shown in the figure, the gain drops below threshold at t_3 and t_4 for 1040 nm and 1070 nm wavelengths respectively. In the period of time from t_5 to t_6 the 1070 nm laser pulse continues to deplete the inversion number after the 1040 nm pulse has finished. If we increase the fiber length without changing other parameters, the overall inversion number will be distributed over a longer fiber. Thus $\underline{N}_2^0$ will decrease and the 1070 nm emission will dominate sooner. If the fiber is long enough then $\underline{N}_2^0$ drops below $\underline{N}_2^{th}{}_{1070}$, and the 1040 nm emission will completely disappear.
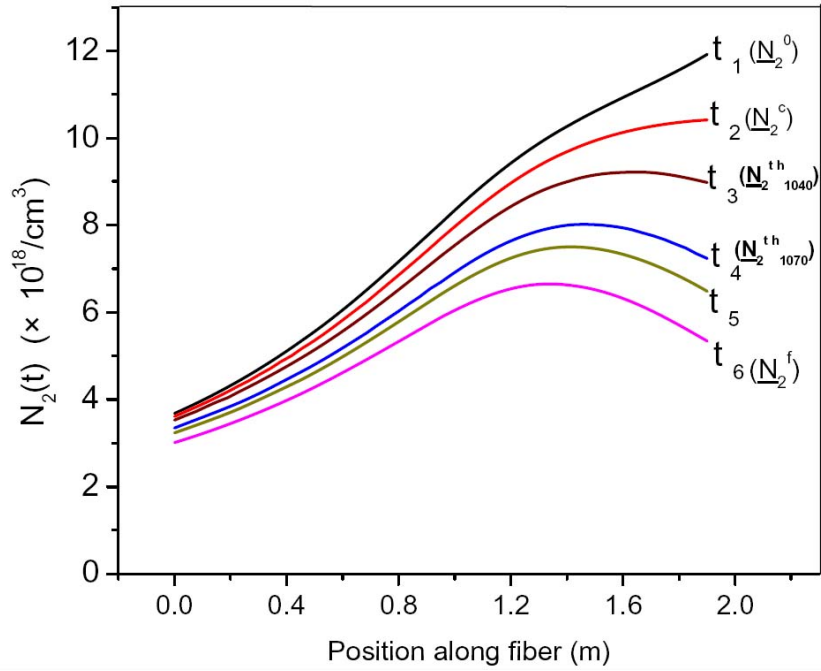
Figure 6.7: Inversion number distribution along fiber at different times which are shown in Figure 6.6 (f); t_1 and t_6 are the times when the inversion number is maximum and minimum; t_3 and t_4 mark the peaks of the two pulses when the inversion number drops to threshold for 1040 nm and 1070 nm wavelengths respectively; t_2 is the time when the gain at 1070 nm becomes higher than at 1040 nm; t_5 marks 10% intensity tail of the 1040 nm pulse.

The situation is further complicated by the recovery time and spectral characteristics of the SA. At a low pump power, the pulse repetition rate is low and the time period between pulses is long; so the saturable absorber recovers to its thermal equilibrium state between pulses. Thus $\underline{N}_2^0$ is high to overcome the large initial absorption in the saturable absorber and the 1040 nm wavelength dominates in each pulse. At a high pump power, the pulse separation time is short and the saturable absorber does not fully recover, thus $\underline{N}_2^0$ is lower in order to reach the switching threshold, and emission at 1070 nm wavelength will become stronger. The 1040 nm (1070 nm) pulse will dominate only when the pump power is very low (high). For a medium pump power, the two wavelengths both see net gain; they dominate in the output alternatively and big-small pulse patterns are observed. Figure 6.8 shows the dynamics of $g_{1040}(t)$, $g_{1070}(t)$, $\underline{N}_2^0$ and N_2^{sa} with the 1040 nm and 1070 nm output pulses at a pump power of 11 W. As can be seen in the figure, after a stronger 1070 nm pulse, the inversion number is depleted to a deeper level. It takes a longer time for the pump to restore the inversion number. At the same time the saturable absorber has more time to recover and N_2^{sa} reaches a lower value for the start of the next pulse. Thus $\underline{N}_2^0$ will be higher for the next pulse and the 1040 nm wavelength will dominate. After the strong 1040 nm pulse the inversion number is not depleted so deeply and the time to buildup to the next pulse time is shorter, thus 1070 nm will dominate in turn for next pulse. So the two wavelengths dominate alternatively as shown in Figure 6.5 (a) and Figure 6.6 (d). In the figures, there is a longer time period between pulses after a 1070 nm pulse compared to after a 1040 nm pulse, which also agrees with the above explanation. Figure 6.9 shows an expanded view of the details of the changes in $g_{1040}(t)$, $g_{1070}(t)$ within the time duration of the pulses

themselves. As depicted in Figure 6.8, $g_{1040}(t)$ becomes higher than $g_{1070}(t)$ sometime preceding the pulses and then drops below $g_{1070}(t)$ sometimes during the pulse. For the 1070 nm dominated case shown in Figure 6.9 (a), the 1070 nm output overcomes 1040 nm output all the time during the pulse, although $g_{1040}(t)$ is slightly higher than $g_{1070}(t)$ during a relatively short period.

The above modeling and discussion can explain the coexistence of the two peak wavelengths, with longer fibers and higher pump powers favoring 1070 nm output, as well, the pulse instabilities such as the two wavelengths lasing alternatively in the pulse train. However we have not reproduced all the pulse patterns in the experiment, such as big-small and big-small pattern for the two wavelengths respectively shown in Figure 6.4 (a) and the period-6 behavior shown in Figure 6.5 (b). In a passive Q-switched laser, pulse instabilities due to nonlinear dynamics have been reported and investigated recently [58, 92, 93]. In reference [58], a period-doubled route to chaotic pulse trains have been observed in a passively Q-switched Nd:YAG laser operating under specific cavity configurations and pump powers. The nonlinear behavior was believed to be related to the rapid relaxation between levels in the lower manifold. In the modeling, in addition to the two-level model for the Nd ion that was conventionally used, the authors included splitting of the ground level with a relaxation lifetime of 30 ns (compared to an upper level lifetime of $230\mu s$). The period-doubling to chaotic pulse shapes could be observed in the simulation under certain pump conditions.

Figure 3.3 shows the Yb ion energy levels in a fiber involved in the lasing output around 1050 nm. The upper and lower manifolds include three and four Stark shifted levels, respectively. The 1040 nm and 1070 nm output radiation correspond to transitions from the bottom of upper level to two
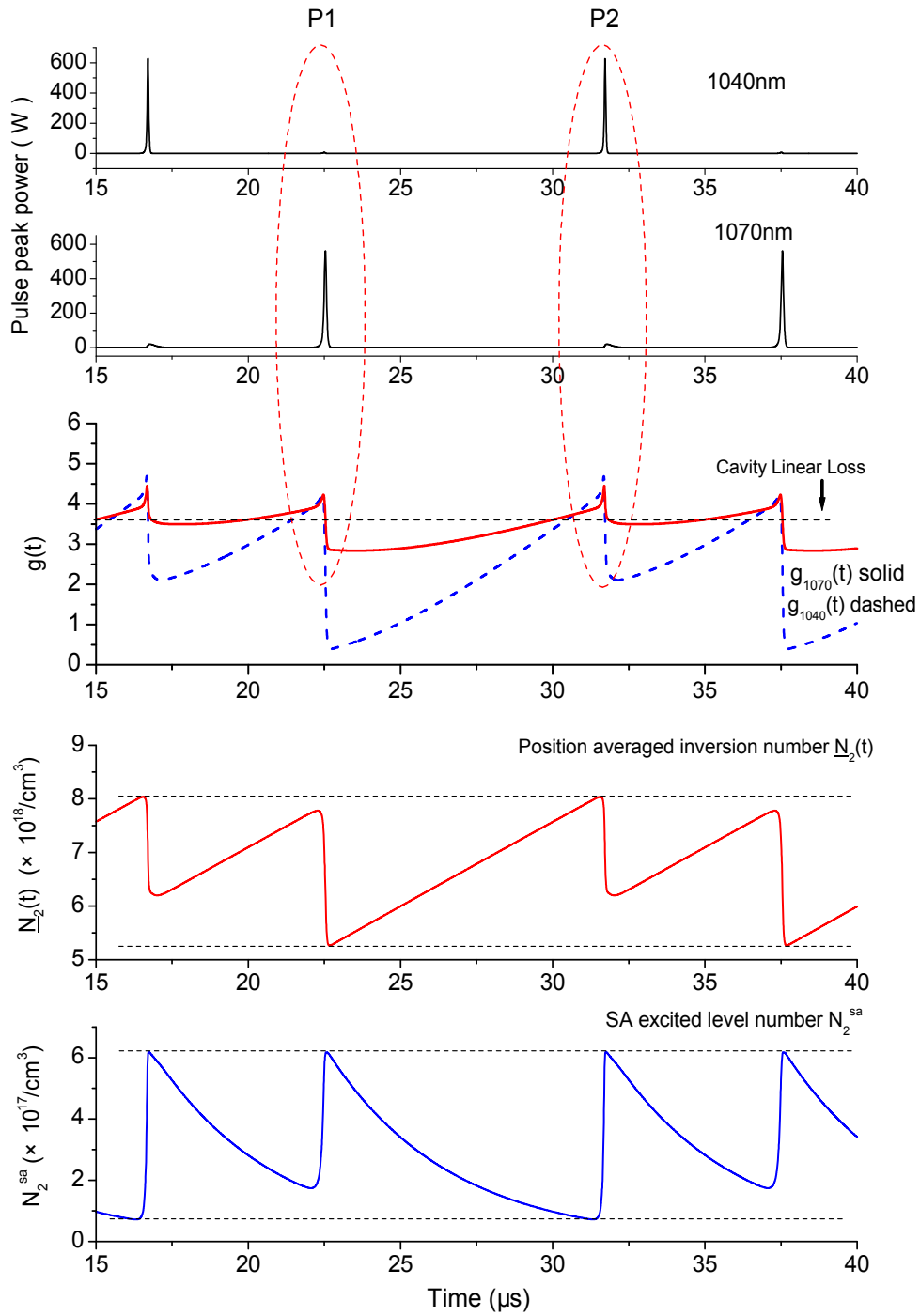
Figure 6.8: Simulated dynamics of $g_{1040}(t)$, $g_{1070}(t)$, $\underline{N}_2(t)$ and $N_2^{sa}(t)$ with 1040 nm or 1070 nm pulses at a pump power of 11 W. The pulse train is also shown in Figure 6.6 (d). Cavity linear loss (~ 3.56) includes output coupler loss, cavity loss η, and fiber attenuation α_k.
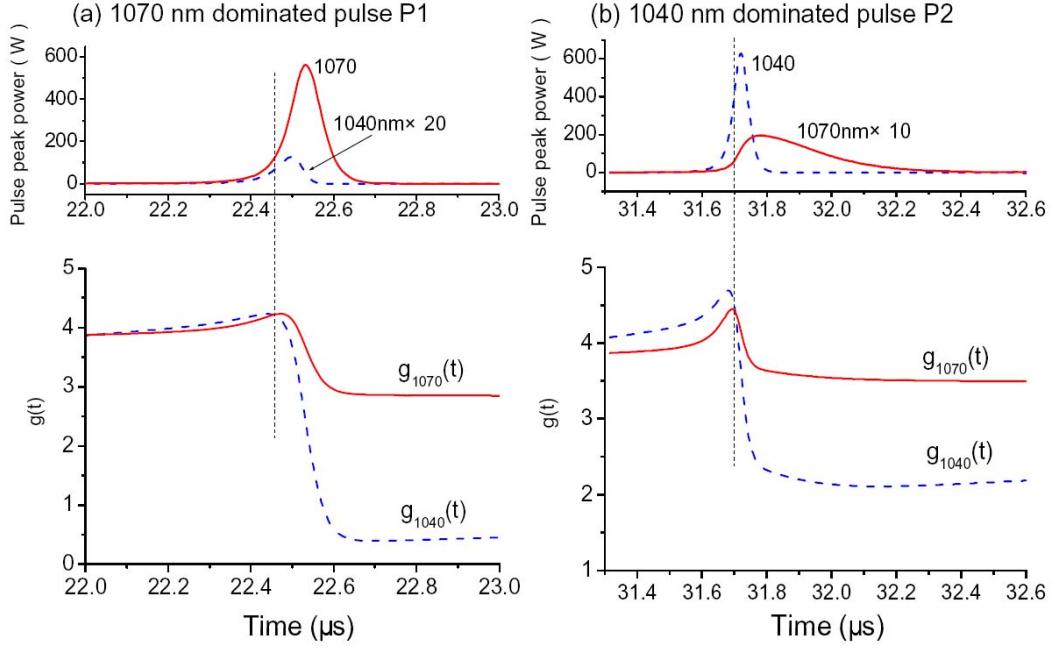
Figure 6.9: Expanded views in time of $g_{1040}(t)$ and $g_{1070}(t)$ for the pulses P1 and P2 shown in Figure 6.8. The vertical dashed lines mark the time when $g_{1070}(t)$ becomes higher than $g_{1040}(t)$ during the pulses.

different sublevels of the lower manifold. Due to the strong broadening of Yb ions in glass at room temperature, the transitions between the sublevels are not fully resolved [10]. As can be seen in Figure 6.2, the spectrum is relatively broad (FWHM ∼3-4 nm), which indicates that the instantaneous emission wavelength may shift within the bandwidth and can be related to the broadening of each sublevel. Therefore, as we have discussed in Chapter 5 for the free-running two-wavelength Yb fiber laser, there are many other mechanisms that have not been included in the simulation, such as sublevels within the manifolds, partial inhomogeneous broadening and transient heating effects. A complete simulation of two wavelength operation would require a more advanced model.

6.4 Summary

A high power, two-wavelength passively Q-switched Yb doped fiber laser has been demonstrated with a very simple cavity configuration. Single transverse mode output at 1040 nm and 1070 nm was obtained with tens of micro-joule pulse energies and hundred nanosecond pulse durations. The two-wavelength generation can be achieved for particular configurations where the effective net gains seen by both wavelengths are comparable and is dependent on fiber length, pump power and cavity Q. A theoretical simulation model qualitatively explains the dynamics of the two wavelengths behavior observed in the experiment indicating that longer fibers and higher pump powers favor 1070 nm laser output and reproduces the pulse pattern where two wavelength pulses alternate at an intermediate pump power.

Chapter 7

High peak power sub-nanosecond passively Q-switched ytterbium doped fiber laser

7.1 Introduction

Nonlinear effects are often observed in pulsed fiber lasers due to the tight confinement of the optical mode and long interaction length, among which the stimulated Brillouin scattering (SBS) has the lowest threshold for narrow line width systems. SBS can provide strong feedback to the cavity together with pulse compression and pulses with duration much shorter than the cavity round-trip time can be generated. Such SBS pulses have been observed in different fiber laser designs, such as self-Q-switched [50, 94], self-Q-switched together with Rayleigh scattering feedback [95,96], actively Q-switched [97,98] and passively Q-switched [15, 16, 24] fiber lasers. Although the pulse stability is usually poor compared to that of conventional Q-switched fiber lasers [22], the pulse peak power can be significantly increased which is beneficial for many applications such as laser micro-machining, laser ablation and nonlinear optics.

In this chapter, we report a passively Q-switched Yb fiber laser using a Cr^{4+}:YAG saturable absorber (SA). SBS output with 245 μJ pulse energy has been obtained, $\sim$75% of which is contained in a main peak with pulse duration of $\sim$490 ps, corresponding to a peak power of $\sim$375 kW. It is the highest peak power reported to date for passively Q-switched fiber lasers to the best of our knowledge. A theoretical model is developed to include SBS dynamics together with passive Q-switching which reproduces the experimental results reasonably well. The results presented in this chapter have been published in reference [99].

7.2 Experiment setup and results

The laser configuration is shown in Figure 7.1. The gain medium is Yb doped large mode area (LMA) double clad (DC) polarization maintaining (PM) fiber with a length of $\sim$1 m. The fiber core/cladding diameters (numerical apertures NA) are 25/250 μm (0.07/0.46) with a nominal absorption of $\sim$11 dB/m at 976nm. End caps (200μm diameter, 1.5 mm length) were put on both ends of the fiber to avoid any unnecessary reflection and facet damage. The pump laser, dichroic mirror (DM), high-reflection broadband mirror (HR) and the output coupler (OC) have been described in detail in Figure 4.1. The SA is a Cr^{4+}:YAG crystal ($< 111 >$ cut) with a small signal transmission of 25% at 1033 nm. Lens 3 and lens 4 were used to focus the laser through the SA with imaging ratios of 1:1.

The laser output power and pulse repetition rate versus pump power are shown in Figure 7.2. The output was linearly polarized ($>$15 dB) with a threshold pump power of $\sim$2.9 W. SBS pulse shortening was observed over the whole pump range. The laser spectrum is shown in Figure 7.3. Although
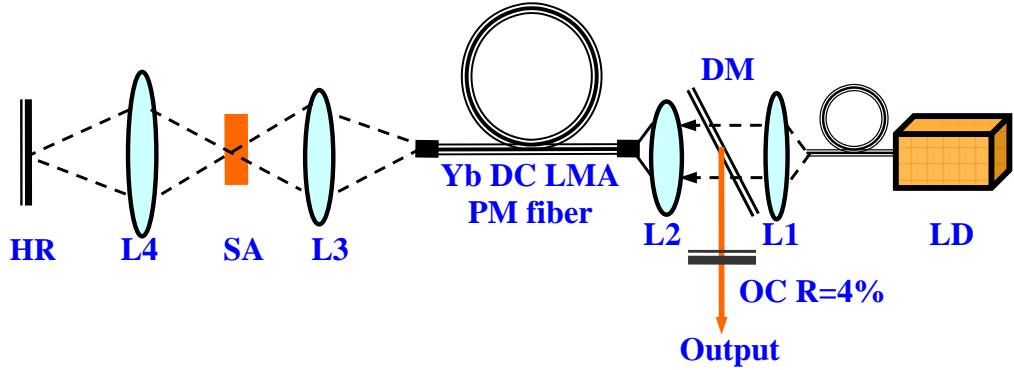
Figure 7.1: Experimental setup: HR-high reflection mirror; SA- Cr^{4+}:YAG saturable absorber; Yb DC fiber-Yb doped large mode area polarization maintaining double-clad fiber; DM-dichroic mirror; LD-fiber coupled laser diode; OC-output coupling mirror.

the spectrometer resolution used in measurement was limited ($\sim$0.05 nm) and the exact seed radiation wavelength varies from pulse to pulse. One can see a modulation with a separation $\sim$0.06 nm (marked by dashed lines) as expected for Stokes shifted SBS [50]. At a pump power of 14.5 W, 5.2 W output has been obtained, with a slope efficiency of $\sim$44%. However, the best pulse repetition rate stability was obtained when the pump power was 4.1 W. With the increase of pump power, the pulse train gradually became less stable; at the same time, wavelength instability was also observed. At pump power of 14.5 W, the pulse repetition rate was $\sim$22 kHz with an averaged timing jitter of 24% (rms). This might be improved by inserting a spectrum control element in the cavity, such as a filter or a grating.

At a pump power of 4.1 W, 637 mW output has been obtained with a pulse repetition rate of 2.6 kHz and pulse energy of 245 μJ. The averaged pulse timing jitter was less than 5% (rms), as shown in Figure 7.4 (a). It is estimated $\sim$75% of the pulse energy was situated in the main peak. The pulse shapes were detected by a fast photodiode (15 ps rise time) and displayed on a 1 GHz analog oscilloscope, which are shown in Figure 7.4 (b) and (c).
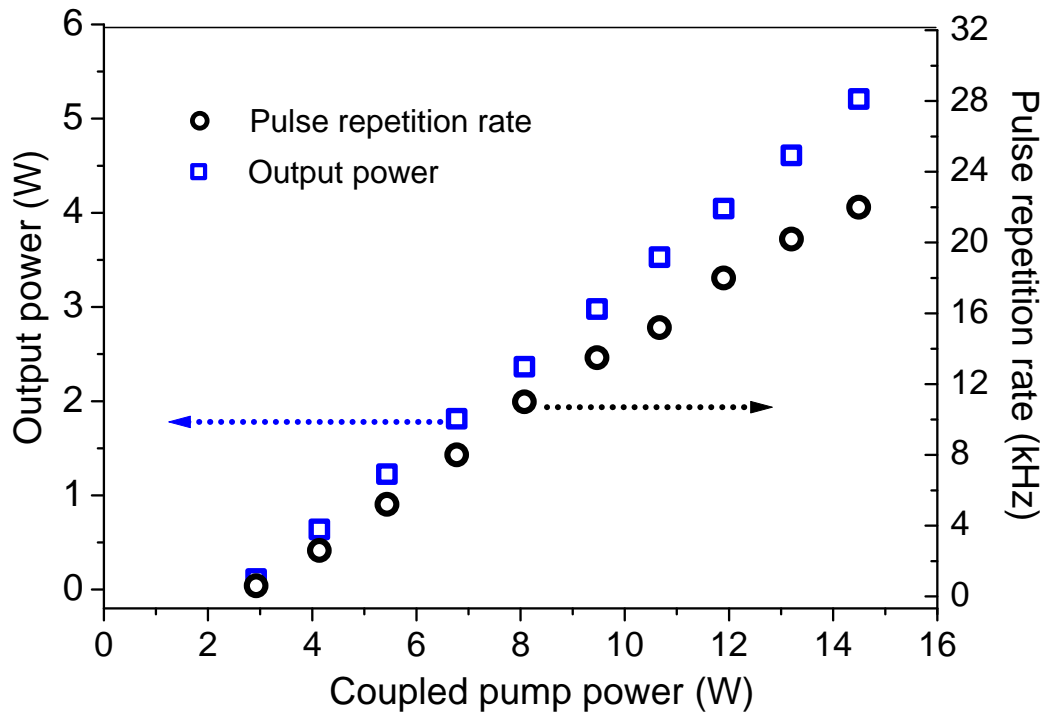
Figure 7.2: Laser output power and pulse repetition rate versus pump power.
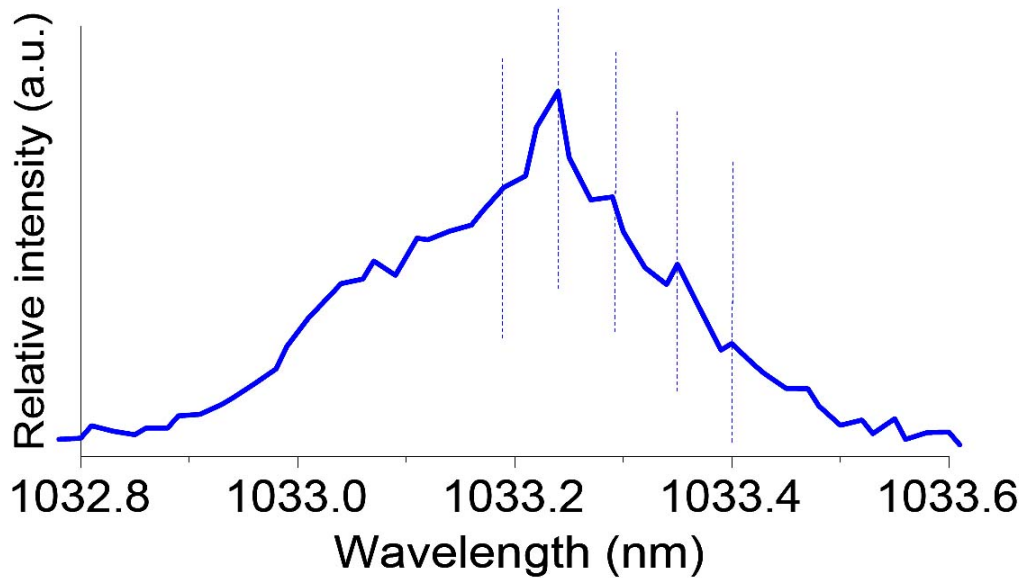
Figure 7.3: laser spectrum measured at a pump power of 2.9 W, the dashed lines mark the peaks of the spectrum, which are separated by ∼0.06 nm.

The temporal response of the photodiode/oscilloscope detection system has been characterized using 120 fs pulses from a separate Ti: sapphire laser, giving an delta input function response time of 350 ps, as shown in Figure 7.5. Deconvolving this instrumental width from the measured width of ∼600 ps gives a real pulse duration of ∼490 ps at 4.1 W pump power, corresponding to a peak power of ∼375 kW. Occasionally during setup adjustment, we have observed damage within the active fiber volume when the peak powers have exceeded these levels. One picture of the damage in fiber is shown in Figure 7.6. As can be seen in the picture, the damage in fiber started from a tiny line in the center position (fiber core) then burst to the cladding area.

7.3 Theoretical simulation and analysis

The laser dynamics can be understood as follows: when the population inversion reaches threshold, which is determined by the cavity feedback and the SA, the emission mode with the highest gain will build up as the signal radiation. Once the signal reaches the Brillouin threshold, laser power will be transferred to cascading Stokes orders. At the same time, the Stokes pulses will also obtain gain from the population inversion as long as the inversion is above the threshold. To better describe the dynamics of Q-switching with SBS, rate equations were employed as follows [49, 96]

$$N_0 = N_1 + N_2 \tag{7.1}$$

$$-\frac{\partial P_p^-}{\partial x} + \frac{1}{v_p}\frac{\partial P_p^-}{\partial t} = \Gamma_p[\sigma_{ep}N_2 - \sigma_{\alpha p}N_1]P_p^- - \alpha_p P_p^- \tag{7.2}$$

$$g_k = \sigma_{ek}N_2 - \sigma_{\alpha k}N_1 \tag{7.3}$$

113
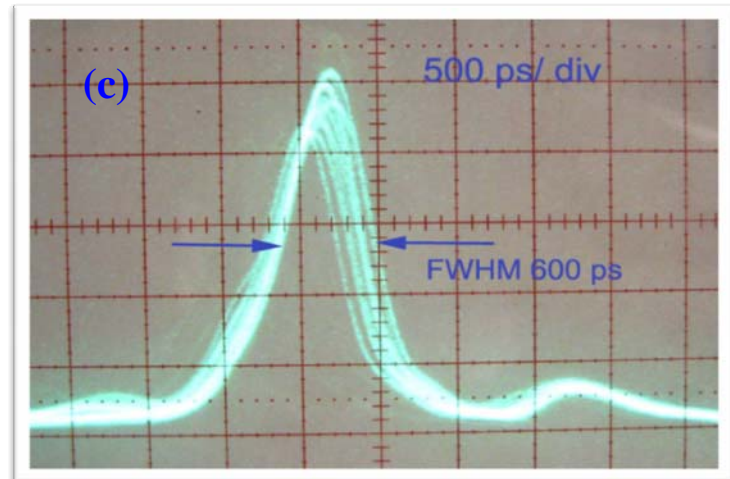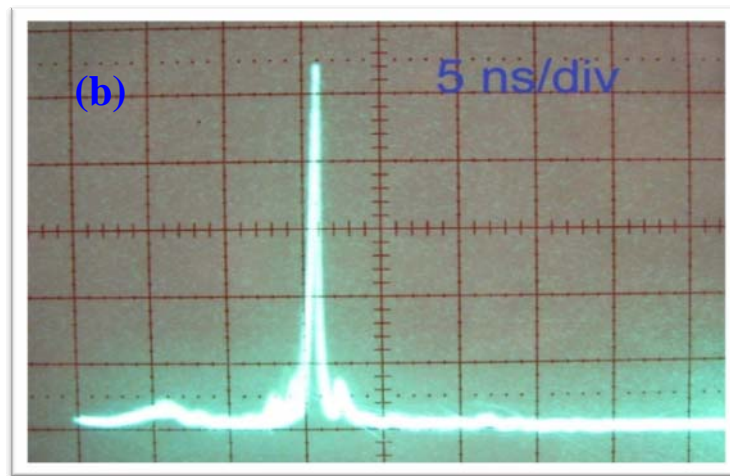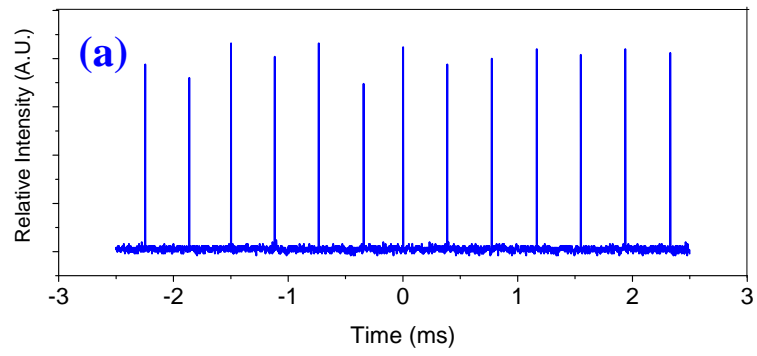
Figure 7.4: Observed (a) pulse train with pulse repetition rate of 2.6 kHz (b) pulse shape and (c) details of the main pulse at a pump power of 4.1 W.

114
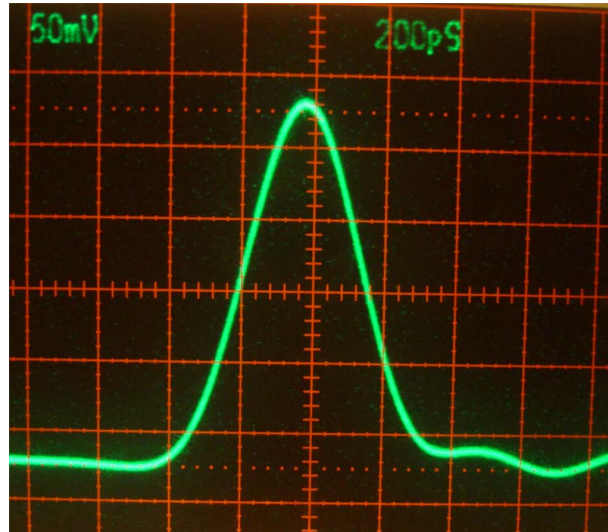
Figure 7.5: Response time of photodiode/oscilloscope calibrated by 100 fs pulses from a separate Ti: sapphire laser.
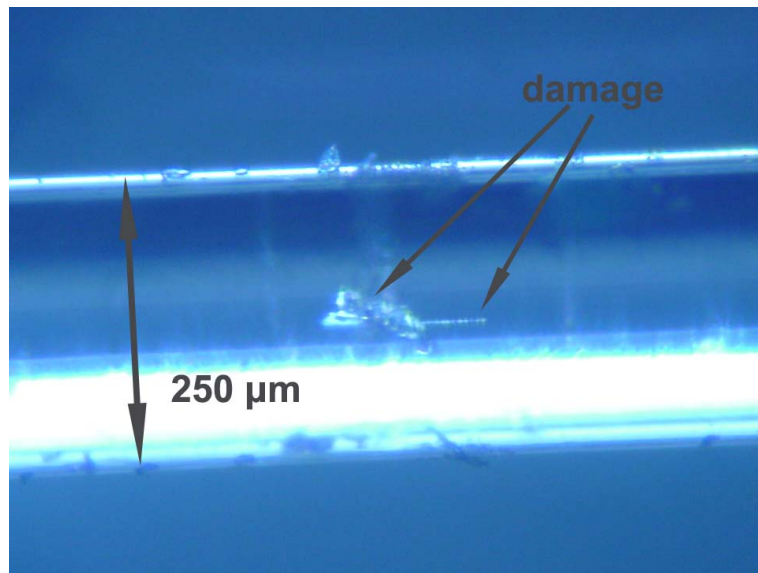
Figure 7.6: Picture of damage inside the fiber caused by the intense SBS pulse.

$$\frac{\partial N_2}{\partial t} = \frac{\Gamma_p \lambda_p}{hcA_{co}}[\sigma_{\alpha p} N_1 - \sigma_{ep} N_2] P_p^-$$
$$+ \sum_k \frac{\Gamma_k \lambda_k}{hcA_{co}}[\sigma_{\alpha k} N_1 - \sigma_{ek} N_2](P_k^+ + P_k^-) - \frac{N_2}{\tau} \tag{7.4}$$

$$\pm\frac{\partial E_k^\pm}{\partial x} + \frac{1}{v_k}\frac{\partial E_k^\pm}{\partial t} = \Gamma_k \frac{g_k}{2} E_k^\pm + \frac{g_B}{2A_{eff}}(\rho_{k-1}^\mp E_{k-1}^\mp - \rho_k^\pm E_{k+1}^\mp) - \frac{\alpha_k}{2} E_k^\pm \tag{7.5}$$

$$\tau_B \frac{\partial \rho_k \pm}{\partial t} + \rho_k^\pm = E_k^\pm E_{k+1}^\mp + f_k^\pm \tag{7.6}$$

where N_0 is the total Yb dopant concentration; N_1 and N_2 are ground and excited number densities. P_p^- represents the backward propagating pump power. $E_k^\pm$ are the normalized forward and backward propagating electrical field amplitudes; $|E_k^\pm|^2$ represent the power in different SBS Stokes shifted orders; k indicates different wavelengths of radiation: 0 is for signal and k=1, 2, 3 ....., are for Stokes orders. The number of Stokes orders included in the simulation can be chosen as necessary; $\sigma_{\alpha p}$, σ_{ep}, $\sigma_{\alpha k}$, σ_{ek} are the absorption and emission cross sections of Yb ion at the pump wavelength and each emission wavelength, respectively, we have used the same values for signal and Stokes since they are very close in wavelength. A_{co} and A_{eff} are fiber core area and effective mode area. $\Gamma_{p(k)}$ is the pump (emission) and fiber core overlap factors, we have assumed the signal has a Gaussian profile when calculating A_{eff} and Γ_k; g_B is the SBS gain coefficient; $f_k^\pm$ are Langevin noise sources and estimated by Gaussian random process [4]; $\rho_k^\pm$ are amplitudes of the hypersound waves and τ_B is their relaxation time. The fiber refractive index was set to n=1.5 and the pump and emission group velocities v_p and v_k were both set to c/n, where c is the speed of light in vacuum. h is the Planck constant, τ is the lifetime of Yb, and $\alpha_{p(k)}$ is the fiber attenuation at pump (emission) wavelength.

116

The rate equation for Cr^{4+}:YAG are:

$$N^{sa} = N_1^{sa} + N_2^{sa} \tag{7.7}$$

$$T_k(t) = exp[-2L_{sa}(\sigma_{gsak}N_1^{sa} + \sigma_{esak}N_2^{sa})] \tag{7.8}$$

$$\frac{dN_2^{sa}}{dt} = \sum_k \frac{|E_k^+|^2 + |E_k^-|^2}{2} \frac{\lambda_k}{A_{sa}hc} \sigma_{gsak}N_1^{sa} - \frac{N_1^{sa}}{\tau_{sa}} \tag{7.9}$$

where N^{sa} is the total ion doping, N_1^{sa} and N_2^{sa} are the ground and excited level number intensities; $T_k(t)$ is the instantaneous two way transmission of the SA, and σ_{gsa}, σ_{esa} are the ground-state and excited-state-absorption cross sections, respectively; L_{sa} is the thickness of the SA; $A_{sa} = \pi d_{sa}^2/4$ is the focal spot area on the SA where d_{sa} is an averaged focal diameter over the length of saturable absorber; τ_{sa} is the lifetime of the excited state.

The coupled rate equations were numerically solved by finite difference method under the boundary conditions given by:

$$P_p^-(L) = P_0 \tag{7.10}$$

$$P_k^-(L,t) = P_k^+(L,t)R_{oc} \tag{7.11}$$

$$P_k^+(0,t) = P_k^-(0,t)(1-\eta)^2 T_k(t) \tag{7.12}$$

where P_0 is the pump power, L is the fiber length, R_{oc}=0.04 is the reflectivity of the output coupler, η is the loss at the high reflector end. The losses at each end of the cavity due to end-cap reflection and lens coupling mismatch

and has been estimated to be ~15% one way. The values of parameters used in the simulation are listed in Table 7.1.

Table 7.1: Values of parameters in simulation

Parameters	Values	Parameters	Values
N_0	$9 \times 10^{19}/cm^3$	τ	$850\mu s$
$\sigma_{e1033nm}$	$6.61 \times 10^{-21}cm^2$	σ_{e976nm}	$2.44 \times 10^{-20}cm^2$
$\sigma_{\alpha 1.33nm}$	$5.15 \times 10^{-22}cm^2$	$\sigma_{\alpha 976nm}$	$2.50 \times 10^{-20}cm^2$
Γ_k	0.96	Γ_p	0.01
N^{sa}	$6.2 \times 10^{17}/cm^3$	τ_{sa}	$4\mu s$
σ_{gsa}	$4.95 \times 10^{-18}cm^2$	$\sigma_{gsa}/\sigma_{gsa}$	7
$\alpha_{p(k)}$	$0.005m^{-1}$	τ_B	5 ns
L_{sa}	4.5 mm	g_B	$5 \times 10^{-11}m/W$
d_{sa}	$150\mu m$	A_{eff}	$300\mu m^2$
A_{co}	$491\mu m^2$	η	15%

For the first Q-switched pulse after the start of pumping, the initial inversion distribution along the fiber is relatively non-uniform (Figure 7.7 (a)). After a few (~3) periods, it reaches a steady state, in which the inversion distribution along fiber is more uniform (Figure 7.7 (b)). The simulated pulse shapes are shown in Figure 7.8. It is observed that the SBS process depends not only on the overall gain of the fiber, but also on its distribution along fiber, since the SBS pulse can be much shorter than the cavity round trip time. Figure 7.9 shows the simulated cascaded SBS process under inversion profile (a). Four orders of Stokes are observed and the pulses are separated by the cavity round trip time of ~10 ns. As can be seen in the figure, the averaged population inversion density along fiber decreases nonuniformly because the pulse duration can be significantly shorter than cavity round trip time. Similar SBS

trains have been observed in other reported Q-switched fiber lasers [16, 50]. In this case, the Stokes peaks were formed always in the position close to the fiber output end, where the cavity radiation is at its peak. Therefore the generated peaks will lag the previous pulse by approximately the cavity round-trip time. This also allows each Stokes pulse to obtain maximum gain from the inversion along the full length of fiber.

The simulated cascaded SBS process under inversion profile (b) is shown in Figure 7.10, in which the SBS peaks can be formed close to the HR mirror of the cavity, for example, Stokes 3. It is exported out of the cavity closely following Stokes 2 without obtaining large gain from the inversion. In this case, the SBS train looks more irregular and one Stokes pulse can dominate in the output.

The simulated pulse shape and duration are in good agreement with experiment. The deviations can originate from the single mode assumption in the simulation. In fact, although the fiber has a low NA and we have used a bending diameter of ~ 20 cm in the experiment, it supports a few modes. Therefore the parameters A_{eff} and Γ_k might not be very accurately estimated. In addition, transverse modes beat together producing high intensity region [100] and line narrowing effects, which may trigger the SBS interaction. This might also be one reason that SBS was not observed when a single mode fiber was used in a similar setup in Chapter 4. In fact, all reported observations of pulse compression by SBS in single mode fibers have required an additional element to enhance the SBS generation such as a frequency narrowing grating [15, 50], an extra length of passive fiber [15, 95–97] or a ring mirror reflector [95, 96].

119
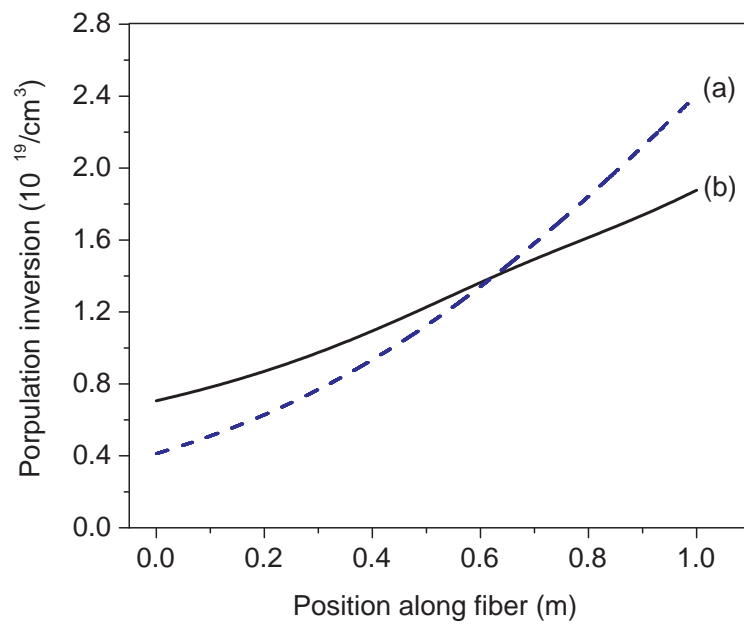
Figure 7.7: Population inversion density along fiber; profile (a), initial inversion for the first Q-switched SBS pulse from the start of pump; profile (b) initial population inversion density for steady state conditions after many pulses. The position axis is oriented with zero position at the HR end of the fiber.
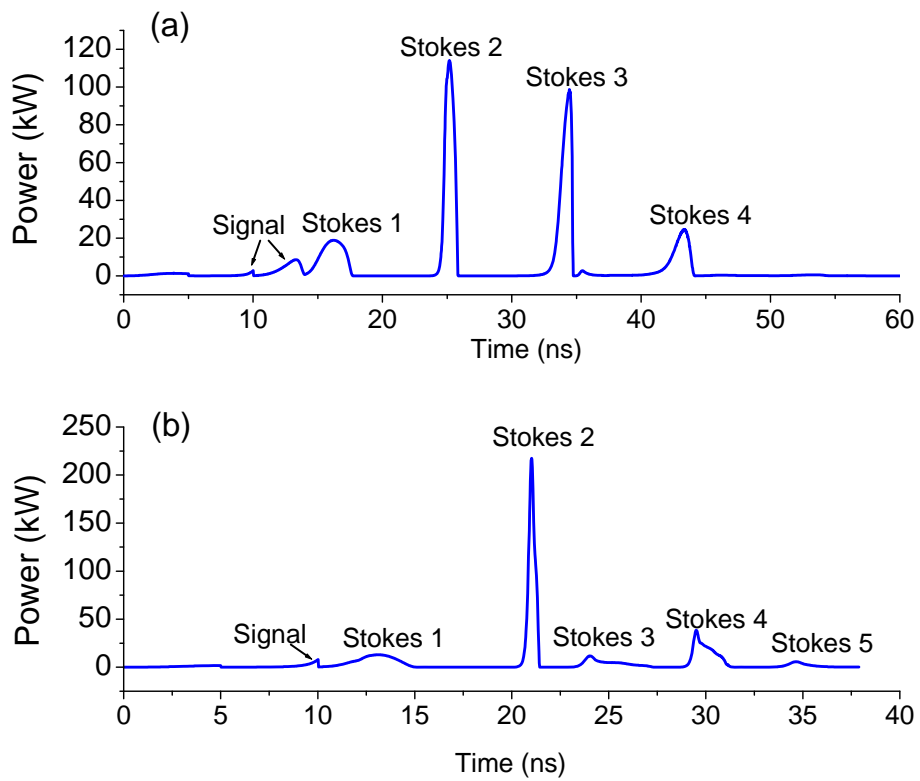
Figure 7.8: (a) Simulated SBS pulse with starting inversion profile from Figure 7.7 profile (a); (b) simulated SBS pulse with starting inversion profile from Figure 7.7 profile (b);
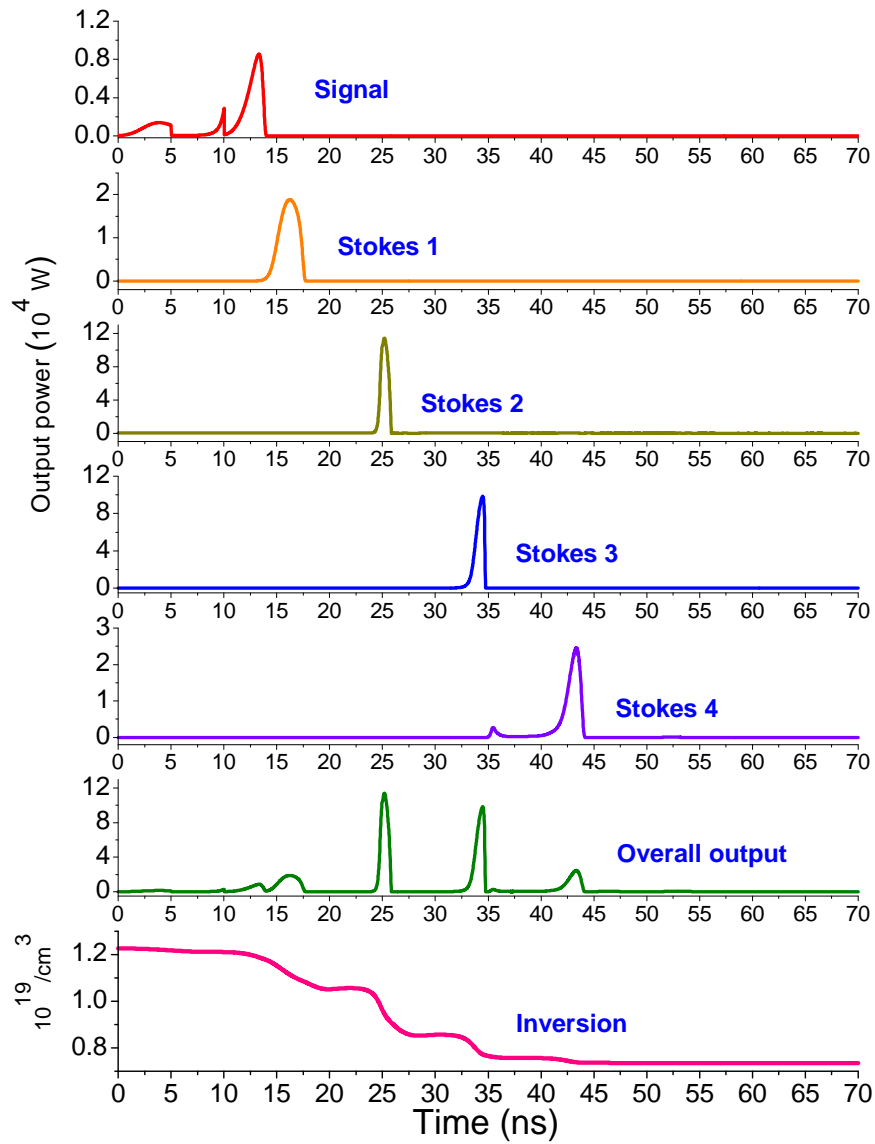
Figure 7.9: Simulated SBS cascaded process under the initial population inversion profile given in Figure 7.7 (a), the inversion is the position averaged population density which has been defined in chapter 4.

122
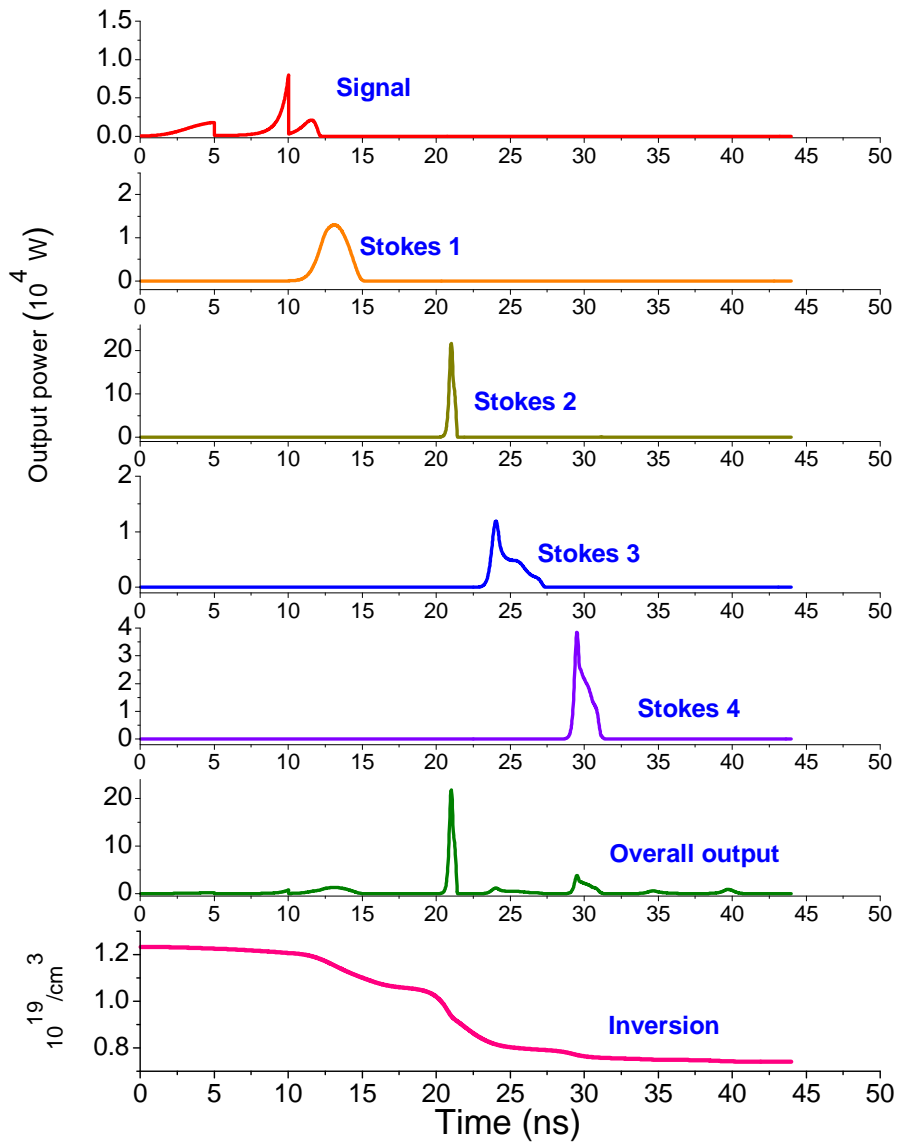
Figure 7.10: Simulated SBS cascaded process under the initial population inversion profile given in Figure 7.7 (b), the inversion is the position averaged population density which has been defined in chapter 4.

123

7.4 Summary

In conclusion, we have demonstrated a passively Q-switched Yb fiber laser utilizing SBS pulse shortening. Linearly polarized 490 ps output pulses with a few hundred kW peak power have been achieved. The numerical model was able to reproduce the mode locked structure and SBS giant pulse observed in experiment reasonably well. Such a compact, affordable high peak power fiber laser could have potential applications in many fields. However, at present the system operates very close to the damage threshold and further work is required to modify the geometry to reduce the peak intensity within the fiber.

Chapter 8

Self-Q-switched ytterbium doped double clad fiber laser with Rayleigh-Brillouin ring mirror

8.1 Introduction

In Chapter 7, a high peak power passively Q-switched Yb fiber laser has been demonstrated with large mode area polarization maintaining fiber. The multiple transverse modes can beat together producing higher intensity regions and may contribute to the line narrowing and the generation of SBS. SBS compressed pulses with ∼490 ps pulse duration and ∼375 kW peak power have been obtained. However damage inside the fiber has been observed occasionally during the adjustment of the fiber laser, which may limit the applications of such Q-switched fiber lasers with SBS.

Recently the mechanism of cooperative dynamics of Rayleigh scattering (RS) and SBS for passive Q-switching in fiber lasers has been investigated [95,96,101–103]. Such a mechanism can be introduced in a fiber laser by means of a nonlinear all-fiber ring mirror. It is observed that the ring mirror could coherently accumulate energy at its extremely narrow resonant frequencies

125

and create the conditions for SBS generation at a relatively low threshold. Operating at lower pulse energies might be a solution for a compact, stable and long lasting Q-switched fiber laser with SBS.

In this chapter, we present a self Q-switched ytterbium doped fiber laser with such a Rayleigh-Brillouin ring mirror. A fiber Bragg grating (FBG) in double clad fiber was employed for both pump coupling and as a cavity mirror. SBS pulses as short as <1 ns have been obtained at both ends of the resonator. Significant Raman scattering effects have also been simultaneously observed and subnanosecond pulses at Raman frequency are generated.

8.2   Experiment setup and results

The laser configuration is schematically shown in Figure 8.1. The gain medium is Yb doped double clad fiber with a length of ∼4.5 m. The core/cladding diameters (numerical apertures NA) are 5.5/130 μm (0.13/0.46) with a nominal absorption of ∼1.7 dB/m at 975nm. The pump laser is a fiber coupled diode laser with a center wavelength of 976 nm. The pump light was coupled into the active fiber by two collimating lenses L1, L2 and a dichroic mirror (DM) with > 96% transmission at 976 nm and > 99% reflectance at 1030-1100 nm. A FBG serving as a cavity mirror was fabricated in double clad fiber (∼ 6 μ m core diameter and 0.15 core NA, single mode at 1060 nm) with a pigtail of ∼ 1m at each side. The FBG has a center wavelength of ∼ 1063.5 nm (16 dB reflection) and a 3 dB bandwidth of ∼ 0.09 nm. The ring mirror acts like a fiber output coupler. 90% of the input power is coupled as output power and 10% of the input is coupled into the ring. A piece of passive fiber (∼ 7m length 1060XP) was spliced between the ring mirror and Yb doped double clad fiber. The output end of the fiber ring mirror was cleaved with an angle

126
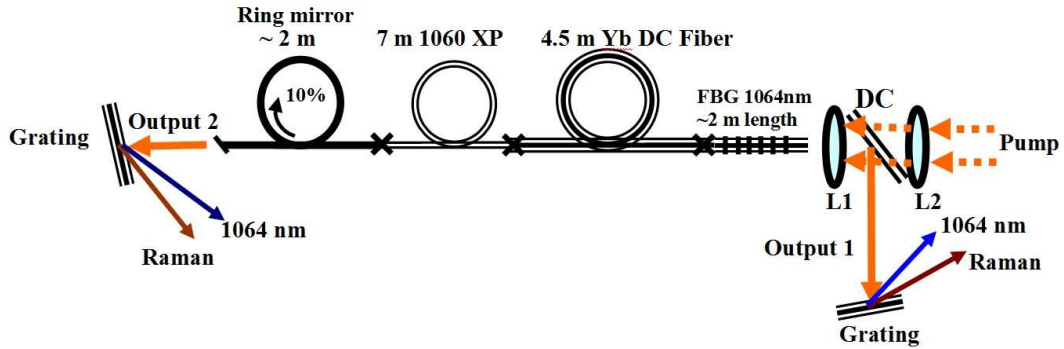
Figure 8.1: Experiment setup, Pump: fiber coupled diode laser at 976 nm, Yb DC fiber: ytterbium doped double clad fiber, DC dichroic mirror, FBG: fiber Bragg grating double clad fiber, L1 and L2: lenses for pump and signal lasers coupling, × indicates fiber splicing position.

of greater than 10^0 to avoid any unwanted back reflection. A grating with a line density of 1180 g/mm was placed at each output end to analyze the different frequency components. At the beginning the gratings have been removed for general measurement of output power, pulse repetition rate, spectrum and overall pulse shape.

Figures 8.2 and 8.3 show the output powers at both ends of the cavity and pulse repetition rate versus pump power. Relatively regular pulse trains can be observed when the absorbed pump power was higher than ∼0.5 W. Output 1 has a slightly higher slope efficiency than output 2 (∼30% compared with ∼22%. At a pump power of 0.85 W, the powers for output 1 and 2 are 0.16 W and 0.15 W, with a pulse repetition rate of ∼7.5 kHz, corresponding to pulse energies ∼ 21 μJ and ∼ 20 μJ, respectively. At a pump power of 2.2 W, the powers for output 1 and 2 are 0.55 W and 0.44 W, with a pulse repetition rate of ∼22 kHz, corresponding to pulse energies ∼ 25 μJ and ∼ 20 μJ. Since SBS is a stochastic progress and can be affected by many factors such as environmental disturbances and noises, the measurements are subject to fluctuations and ±10% error bars have been added to the plots. However
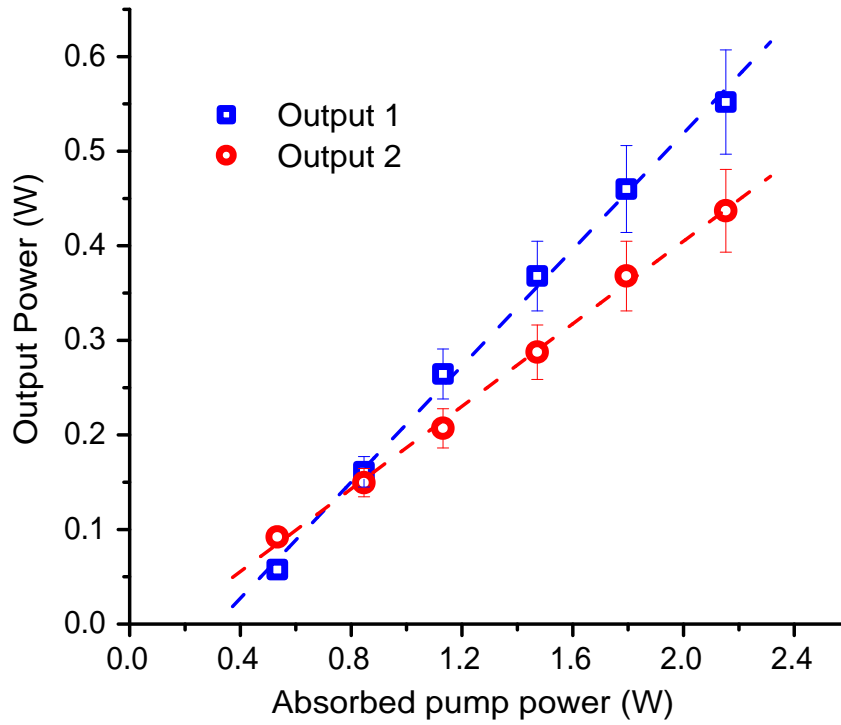
Figure 8.2: Output power of each end versus absorbed pump power, the dashed lines are the linear fit of the measurements, error bars ±10%.

the timing jitter is not constant with time. The pulse trains kept shifting in frequency from one to another with a time scale of a few seconds. Higher timing jitter is usually exhibited during switching in output frequency. However very stable pulse repetition rate has been observed for period up to 1∼2 seconds. Figure 8.4 shows the pictures grabbed from the video recording the pulse trains displayed by a digital oscilloscope. Significant range of the timing jitters can be viewed with the best examples having a jitter less than a few percent. This might indicate that some disturbances to the laser operation are varying with relatively slow speed, for example, temperature variations. However further study is required to clearly understand the physics behind the phenomena. Figure 8.5 shows a pulse train obtained at a pump power of 2.2 W with a pulse repetition rate of ∼22 kHz. The measured timing jitter is ∼5% (RMS).

Figure 8.6 shows the measured spectra for both outputs. Before starting
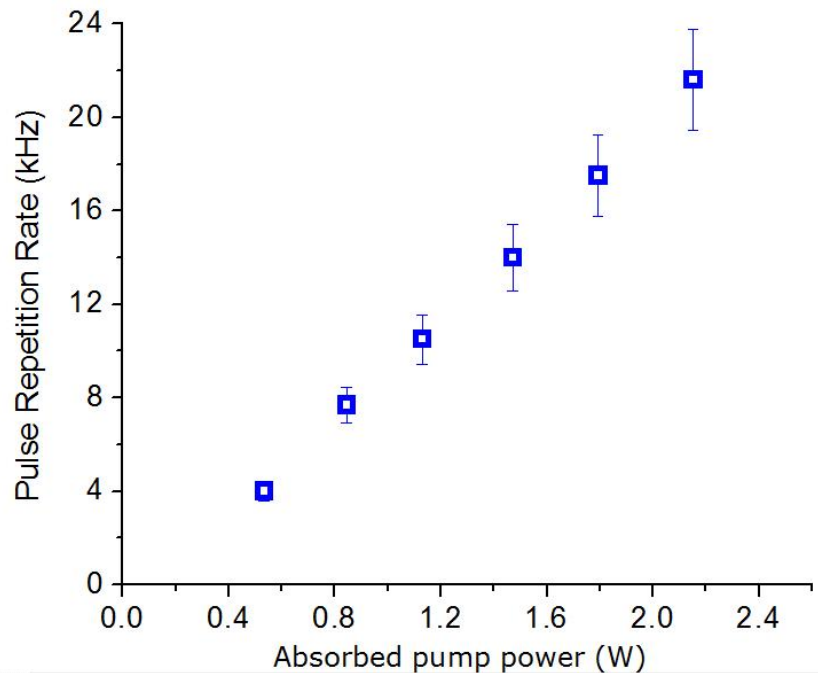
Figure 8.3: Pulse repetition rate versus absorbed pump power, error bars ±10%.

the operation, the central wavelength of the FBG was measured. A free running Yb fiber laser was firstly built by removing the passive fiber and ring mirror and vertically cleaving the end of Yb double clad fiber to be working as an output coupler. The measured spectrum is shown in Figure 8.6 as a dashed line, the peak of which corresponds to the center wavelength of the FBG. The vertical dashed lines mark the peaks of each frequency component of the outputs. The separation between the dashes lines is ∼0.06 nm, which matches the SBS shift in fiber at 1.06 μm wavelength. As can be seen in the spectra, the output 1 consists largely of the energy of even number Stokes orders 2, 4, 6, $\cdots$, with the majority in the second order. The output 2 includes the odd number Stokes orders 1, 3, 5,$\cdots$, with most of the energy in the first order. Similar results have been obtained in reference [96] with a self-Q-switched Er doped fiber laser.

Figure 8.4: Grabbed pictures from the video recording the pulse trains. The upper traces show the picture when the laser sticking to pulse repetition rate and the lower traces show hte cases when the laser was in a high timing jitter state. The pulse trains were recorded at an absorbed pump power of 0.65 W with a pulse repetition rate of ~5kHz.
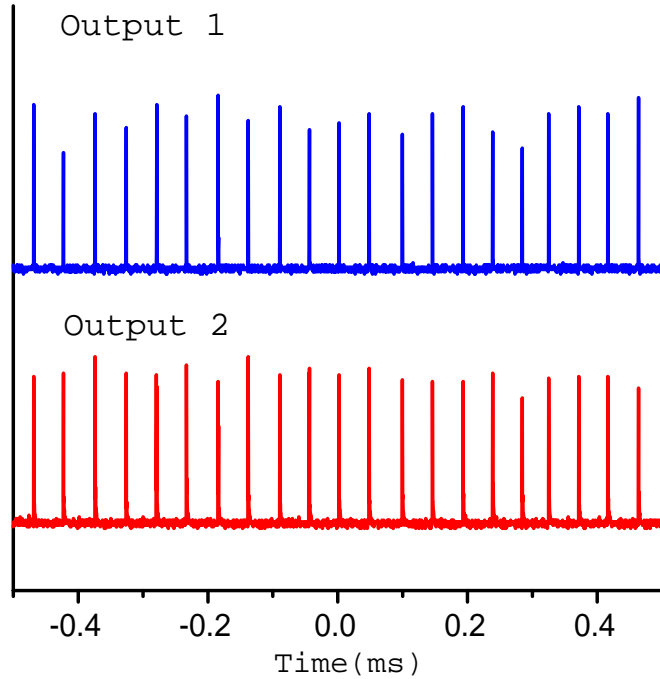
Figure 8.5: Observed pulse train at an absorbed pump power of 2.2 W with a pulse repetition rate of ∼22 kHz.

The temporal relation of the two output pulses is shown in Figure 8.7, in which peak of output 1 pulse is ∼40 ns earlier than that of output 2 pulse. This indicates the pulse peaks are always formed in a position that is close to the end of output 1, with a optical path difference of ∼8 m in fiber (assuming the fiber refractive index is 1.5). To represent a more general case, an averaged mode (128 pulses) of the digital oscilloscope has been employed in taking the pulse shapes. However due to the limited sampling rate, the temporal resolution of the oscilloscope is low (∼ 5 ns). The detailed structure of the pulses are not observable. Therefore, a faster analog oscilloscope (1 GHz sampling rate) was used to display the pulse shapes, as shown in Figures 8.8 and 8.9. The output pulse usually shows a few separated peaks within a time scale of ∼10 to 20 ns. For output 1, most of the energy is contained in one major peak with a measured pulse duration of ∼700 ps, as shown in Figure 8.8 (b). Deconvolving

131
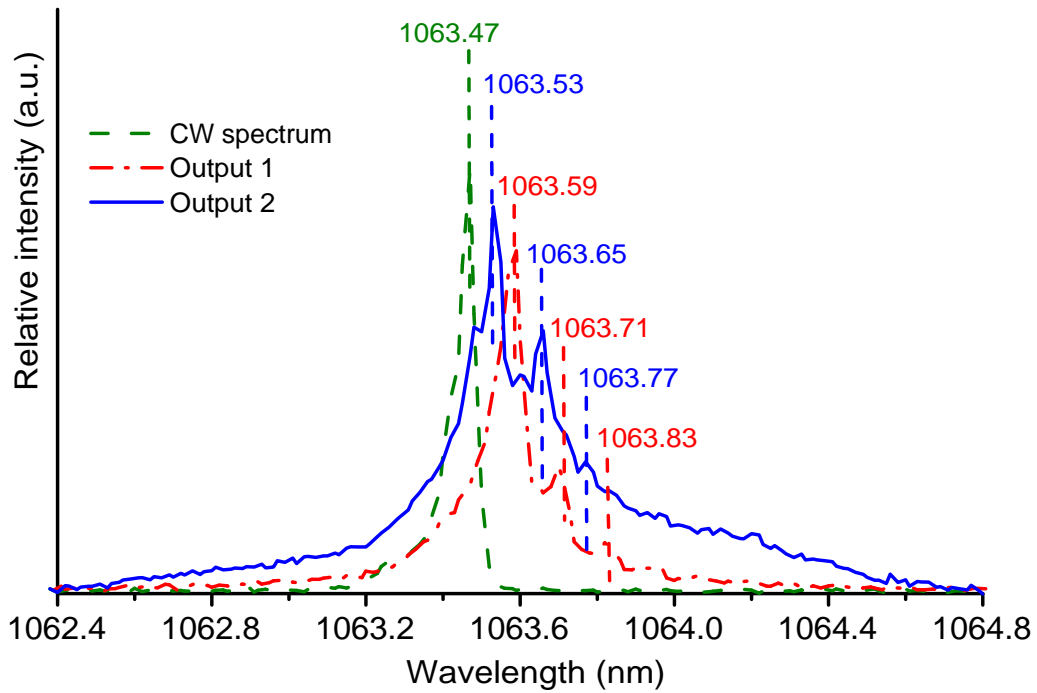
Figure 8.6: Laser spectrum of each output, measured at a pump power of 0.85 W. The CW spectrum is the free running spectrum of the laser built with this FBG, which indicates the center wavelength of the FBG, the vertical dashed lines mark the peaks of each frequency components. The separation between the dashes lines is ~0.06 nm, which is an indication of SBS in fiber at 1.06 μm wavelength.
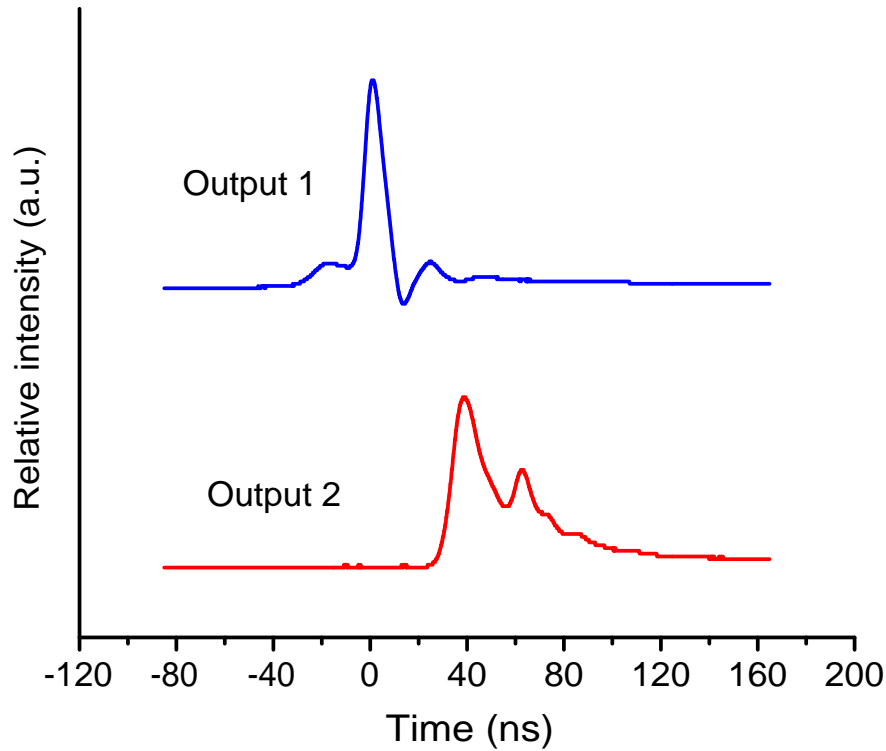
Figure 8.7: Synchronized pulse shapes of output 1 and 2, measured by a two-channel oscilloscope with averaged mode at a pump power of 0.85 W.

the instrumental response time of 350 ps, the real pulse duration should be $\sim$ 600 ps. It is estimated that no less than 3/4 of the whole pulse energy ($\sim$21μJ) was situated in the main peak, which results in a peak power of 26 kW. For the pulse of output 2, there are a few (2$\sim$3) major peaks spaced closely with pulse duration $\sim$ 1ns, as can be seen in Figure 8.9 (b).

As such high peak power pulses transmit within relatively long fiber laser cavity (overall cavity length $\sim$15 m), significant Raman effects have been observed at both ends of the output. The two gratings were then put on to separate the Raman frequencies from the SBS frequencies. The ratio of average power at the SBS and SRS frequencies was determined by measuring the two beams in the first diffraction order from the grating. It is estimated $\sim$20% and $\sim$50% of the overall power has been transferred to SRS for outputs

133
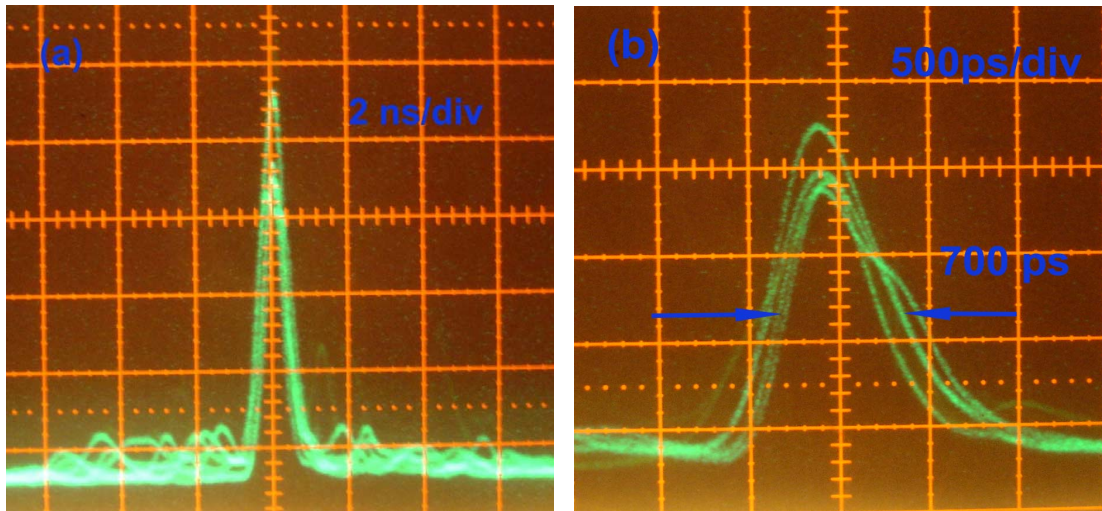
Figure 8.8: Measured pulse shape of output 1 with a 1 GHz analog oscilloscope at a pump power of 0.85 W, (a) 2 ns/div (b) 500 ps/div; deconvolving the intrumental response time of 350 ps from the ~700 ps, the real pulse duration is ~600 ps.

Figure 8.9: Measured pulse shape of output 1 with a 1 GHz analog oscilloscope at a pump power of 0.85 W, (a) 10 ns/div (b) 1 ns/div.
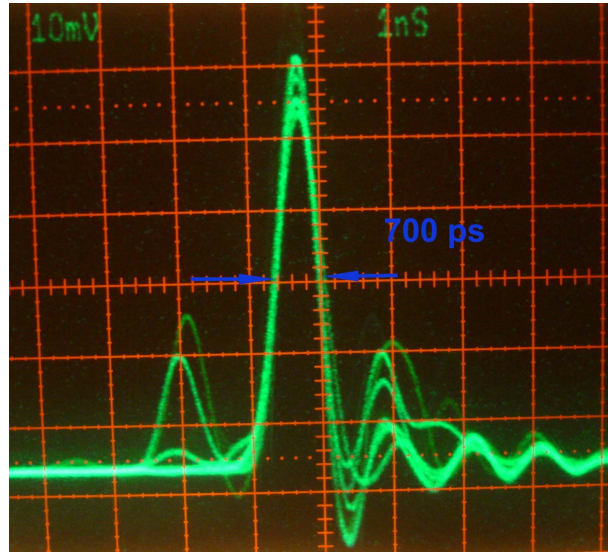
Figure 8.10: Observed Raman pulses of output 1 at a pump power of 0.85 W; deconvolving the intrumental response time of 350 ps from the ∼700 ps, the real pulse duration is ∼600 ps.

1 and 2, respectively. The relatively higher Raman efficiency for output 2 is due to its longer transmission distance, since the SBS pulses are formed in Yb fiber, which is closer to the end of output 1, as has been discussed above. The Raman pulse shapes were recorded by measuring the beams separated by grating, as shown in Figures 8.10 and 8.11. The Raman pulse of output 1 has quite similar pulse shape to that of its original pulse measured without the grating, as shown in Figure 8.8. The major peak has a pulse duration of ∼600 ps. If the conversion efficiency is ∼20%, the corresponding Raman peak power is estimated to be ∼5 kW (20% of 26 kW). For the Raman pulse of output 2, although it still shows several peaks similar to the original pulse shape in Figure 8.9, one major peak was observed to be dominant in the output with a pulse duration of ∼700 ps.
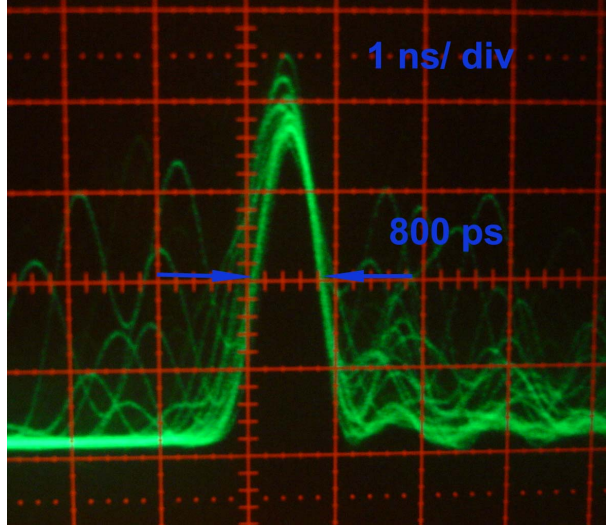
Figure 8.11: Observed Raman pulses of output 2 at a pump power of 0.85 W; deconvolving the intrumental response time of 350 ps from the ∼800 ps, the real pulse duration is ∼700 ps.

8.3 Analysis and discussion

8.3.1 Mechanisms of nonlinear ring mirror

A schematic diagram of the fiber ring mirror is shown in Figure 8.12. The operation can be understood as follows. The dominant radiation frequency ν_0 will be a resonant frequency of the ring and also very close to the center wavelength of the FBG. The radiation circulates in the ring in a clockwise direction. The power at ν_0 inside the ring can be much higher than the input power due to the coherent phase matching provided by the interferometer, which is similar to a Fabry-Perot cavity. Rayleigh backscattering with the same frequency ν_0 will be generated and transmitted in the counterclockwise direction. If the power is high enough, the light at the frequency $\nu_1 = \nu_0 - \Delta\nu_{SBS}$ will be generated by SBS. The SBS also circulates in the counterclockwise direction and its power is again enhanced due to due to resonant accumulation of the pump radiation in the ring. The radiation is extracted partially through the

136
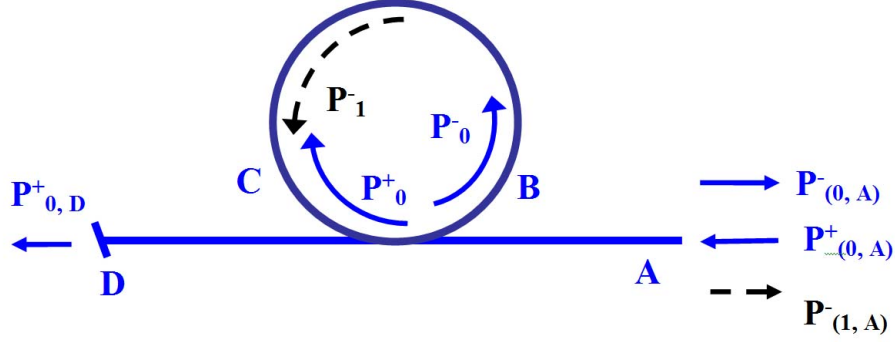
Figure 8.12: Scheme of the Rayleigh Brillouin fiber mirror, which is similar to a Fabry-Perot cavity and can coherently accumulate energy at its resonant frequencies.

coupler and provides reflection from the mirror.

The linear reflection is associated with Rayleigh scattering, while the non-linear reflection is associated with the SBS. The reflection and transmission coefficients are defined by

$$R \equiv (P_{(0,A)}^- + P_{(1,A)}^-)/P_{(0,A)}^+ \tag{8.1}$$

$$Tr \equiv P_{(0,D)}^+/P_{(0,A)}^+ \tag{8.2}$$

where $P_{(0,A)}^+(t) \sim exp(t/T)$, T is a characteristic rise time, $T = \infty$ corresponds to a constant power excitation. Compared with the input power $P_{(0,A)}^+(t)$, the power at ν_0 $P_{(0,C)}^+(t)$ inside the ring is enhanced by factor Q; Q can be expressed as

$$Q(T) = \frac{k_{AC}}{[1 - \sqrt{k_{AD}}exp(-L_R n/2cT)]^2} \tag{8.3}$$

where $k = \kappa_{AD}$ is the coupling ratio of the fiber coupler, L_R is the length of the ring, n is the refractive index, and c is the light speed in vacuum. The reflection and transmission coefficients are obtained by Fotiadi in reference [101] as

$$R = Q^2 \Lambda_R L_R \tag{8.4}$$

$$Tr = (\sqrt{k_{AD}} - \sqrt{(k_{AC})Q})^2 \tag{8.5}$$

137

Where Λ_R is Rayleigh backreflection coefficient. The factors Q and Q^2 can be calculated by equation 8.3 as a functions of T for different coupling ratio κ_{AD}. If $\kappa_{AD} = 90\%$ and $T > 100nL_R/c$, $Q \sim 35$ and $Q^2 \sim 1000$.

In the nonlinear regime, the lasing at ν_1 is generated by the SBS amplification in counterclockwise direction, when the threshold is reached

$$k_{AC}exp(g_{SBS}P_{0,B}^+ L_R/S) \geq 1 \qquad (8.6)$$

where S is the effective area of the fiber. The SBS will deplete the power at ν_0 and affect the reflection and transmission coefficients of the mirror. The dynamical response can be numerically calculated by the one dimensional RS-SBS model. The contrast of the switching can be up to 45 dB [101].

8.3.2 Analysis of the laser dynamics

Based on the theory of nonlinear ring mirror, the laser dynamics in this experiment can be understood as follows. The feedback for radiation at frequency ν_0 is provided by the FBG and Rayleigh back reflection from the ring. The lasing at ν_0 starts when the threshold is reached due to continuous accumulation of population inversion. The power inside the ring is enhanced by a factor of Q due to the resonance of the ring cavity. Q can be calculated by Equation 8.3 and is dependent on the rise time of the radiation. When the power inside the ring reaches the SBS threshold, the Stokes frequency at $\nu_1 = \nu_0 - \Delta\nu_{SBS}$ will be generated in the counterclockwise direction. ν_1 is still within the bandwidth of the FBG and undergoes partial reflection. The radiation at ν_1^+ ($-,+$ indicates a direction away from and toward FBG in the setup, respectively) could build up very quickly and obtain significant gain from Yb doped fiber. Meanwhile, the SBS threshold in the Yb fiber is achieved and cascaded SBS radiations ν_2^-, ν_3^+ $\cdots$ are generated in either direction. Since the peak of ra-

diation at ν_2^- is formed in a position in Yb fiber, it has a shorter optical path and shows ~ 40 ns earlier in the output than that of ν_1^+, as shown in Figure 8.7. Compared with the results in reference [96], in which Er doped fiber is used as gain medium, the radiations at ν_1^+ has a rise time of ~ 45 ns and radiations at ν_1^+ and ν_3^+, are separated by $\sim$120 ns in time. In the present experiment, a Yb fiber is used as gain medium, which has ~ 10 times higher emission cross section than that of Er doped fiber. Therefore the formation of pulses at fundamental frequency and the cascaded SBS progress can take place much faster. No obvious separation has been observed for pulses at ν_1^- and ν_3^-; much shorter pulse durations ($\sim$600 ps compared with $\sim$15 ns) and higher peak power ($\sim$20 kW compared with $\sim$300 W) have been achieved. However, detailed numerical modeling is still required to better understand the laser dynamics.

8.4 Summary

In summary, a self Q-switched ytterbium doped fiber laser has been demonstrated with a Rayleigh-Brillouin ring mirror as a gain switching mechanism. Nanosecond to subnanosecond output has been observed at both ends of the laser cavity with a pulse repetition rate up to 22 kHz. For output port 1, pulses as short as 600 ps have been measured with a peak power of 26 kW and significant Raman scattering has been observed; subnanosecond pulses at Raman frequencies have been obtained at both ends of the fiber laser with peak powers up to a few kW. The pulse repetition rate was observed to jump from one frequency to another; however, very stable pulse repetition rates can be kept observed for a periods of 1$\sim$2 seconds. Further study is required to better understand this phenomena. Such a compact, adjustment free subnanoseocnd

Q-switched fiber laser has potential applications in many fields.

Chapter 9

Summary and future work

9.1 Summary of experiment

In summary, two aspects of Q-switched Yb doped fiber lasers have been investigated. The first is stimulated Brillouin scattering (SBS). SBS is the most significant nonlinear effect in Q-switched fiber lasers and has the lowest threshold for narrow linewidth systems. SBS can significantly affect the laser dynamics in Q-switched fiber lasers. In this thesis, passively Q-switched Yb doped double clad fiber lasers both with and without SBS have been investigated. The second aspect studied is multiwavelength generation in Yb doped fiber lasers.

With single mode small ($6\ \mu m$) and medium ($10\ \mu m$) core Yb doped fibers and Cr^{4+}:YAG saturable absorbers (SA), high power and high repetition rate passively Q-switched fiber lasers have been demonstrated without SBS. Hundred nanosecond pulses have been obtained with pulse energies of tens of μJ and pulse repetition rates of up to 300 kHz. The output has relatively low timing jitter of $< 1 - 2\%$ and broad emission bandwidth of $\sim$3-5 nm.

With large mode area (LMA) ($25\ \mu m$) polarization maintaining Yb doped fiber, high peak power passively Q-switched fiber lasers have been achieved with SBS. Approximately 500ps pulses have been obtained with pulse energies

of $> 200\mu J$, pulse repetition rates of up to $\sim$20 kHz and peak power of $>$ $300kW$. The output has a higher timing jitter of $\sim 5 - 20\%$ and a narrow spectrum consisting of a few peaks separated by the expected Brillouin shift. The generation of SBS is believed to be related to the beating of transverse modes in the LMA fiber, which may produce high intensity regions and line narrowing effects, and trigger the SBS interaction. Damage inside the fiber has been occasionally observed, which may limit the application of this laser.

To obtained a long lasting Q-switched fiber laser with SBS, a self Q-switched Yb fiber laser has been demonstrated with a Rayleigh-Brillouin ring mirror. The ring mirror could coherently accumulate energy at its extremely narrow resonant frequencies and create the conditions for SBS generation at a relatively low threshold. Subnanosecond pulses have been generated with a peak power of up to 26 kW.

As a typical quasi three level gain medium, the gain bandwidth of Yb doped fiber is broad and its emission strongly depend on the excitation level. At a certain cavity configuration and pump level, the Yb doped fiber shows two gain peaks with almost equal magnitudes. A two-wavelength passively Q-switched Yb fiber laser has been demonstrated without using any spectral selection mechanisms. Two wavelengths centered at 1040 nm and 1070 nm are generated directly from the cladding pumped Yb doped fiber laser. The two-wavelength pulses can occur either together or on different oscillation cycles depending on pump conditions. By removing the saturable absorber, a self gain switched two-wavelength Yb doped fiber laser has also been obtained. The two-wavelength outputs are centered at 1044 nm and 1070 nm and show alternative relaxation oscillations.

9.2 Summary of theoretical modeling

Numerical modeling with rate equations is a powerful tool to understand the laser dynamics and optimize the configurations in Q-switched lasers. Traveling wave models have been used to simulate the dynamics of passively Q-switched Yb doped double clad fiber lasers. Since the Cr^{4+}:YAG crystal is relatively thick, the focal spot diameter can vary significantly. The focused beam in the SA has been assumed to have a Gaussian profile and is analyzed using traveling wave rate equations for the first time to the best of our knowledge. This model was able to accurately predict the temporal and spatial saturation of SA, which is critical to calculate the pulse characteristics.

To simulate the laser spectrum, the modeling has included the complete gain curves of the fiber and could illustrate how the radiation builds up from the broadband spontaneous emission spectra. The multi-wavelength model could also qualitatively explain the dynamics of the two-wavelength behavior observed in the experiment.

For Q-switched fiber lasers with SBS, the electrical field of the laser signal is not only related to the gain from the fiber, but also to the gain and loss from other Stokes orders, as well as the relaxation of acoustic waves. The simulation shows the formation of the SBS pulse strongly depends on the inversion profile along the gain fiber. The more non-uniform the inversion population distribution the more likely that the SBS peaks are formed at the end of the fiber with the largest population inversion. For this case, the SBS pulses are separated by the cavity round trip time and the overall pulse shape looks like Q-switched mode locking. With a more uniform distribution of population inversion, the SBS can be formed in any position of the fiber and one Stokes will dominate in the output. The overall pulse shape will look more

143

irregular.

9.3 Future work

The project can be further investigated from the the following aspects.

The first is the all-fiber design, which has the major advantage over free space optics of compactness, robustness and freedom from adjustment. All fiber passive switching has been achieved by splicing Yb double clad fiber to a piece of Sm doped fiber [30]; however, the pulse duration is in the μs range and the peak power is only $\sim$12 W. A Cr^{4+}:YAG crystal fiber laser [104] and amplifier [28] have also been reported, which might be employed as a saturable absorber in all fiber passively Q-switched fiber lasers. The model calculations described in this thesis will also be applicable to simulating such an all-fiber passively Q-switched fiber laser. In addition, fiber combiners for all fiber high power pump are commercially available from a number of commercial suppliers.

One future direction is to improve the passively Q-switched fiber laser with SBS. Although the pulse intensity fluctuation and timing jitter in such lasers are due to the stochastic nature of SBS and can not be eliminated completely, still there is room for improvement. For example, we do observe quite stable output for a short period of $\sim$1-2 s, as has been described in Chapter 8. The generation of SBS might be affected by thermal variations and environmental disturbances such as ambient acoustic noise. One may be able to improve the operation if the fiber is kept at low temperature or the external variations and noise are isolated from the laser system. In addition, in chapter 7, higher timing jitter appeared to be related to larger fluctuations in the output wavelength. Therefore, it might also be helpful if a wavelength

selection and stabilization element is inserted into the cavity. Such an element should have a narrow bandwidth and a center wavelength that is free from thermal fluctuations.

Thirdly, as a quasi-three level medium, the emission and absorption cross sections of Yb doped fiber are temperature dependent, therefore, a more advanced model should consider the temperature variations during the Q-switching progress. Such temperature dependent models have been employed for the simulation of thin disk lasers [105, 106]. For heavily doped fiber lasers, the inversion population along fiber can be very non-uniform, and a major part of the stimulated transitions can happen at one end of the fiber, as can be seen in Figure 6.7. Therefore there might be a transient heating effect during the Q-switching progress, which may lead to a reduction in the gain. As simulated in reference [79], the temperature profile in the fiber core area can change significantly within $\sim$100 ns to 1μs after a transient heating effect, which is comparable to the long tail time scale observed from Q-switched laser pulses observed in this thesis and other papers [13, 14, 17]. In this case, a heat-flow model is required to describe the lateral cooling and the temperature for each position along the fiber.

In summary, in this thesis a greater understanding of Yb based Q-switched fiber lasers has been obtained and has led to the development of a number of operating systems which should be suitable for a wide variety of applications. Further efforts will include realizing more compact and reliable fiber laser systems while preserving the laser performance and building more advanced models to simulate the laser dynamics in Yb doped fiber.

Bibliography

[1] G. P. Agrawal. *Nonlinear Fiber Optics Fourth Edition*. Academic Press, 2006.

[2] T. Li. *Optical Fiber Communications: Fiber Fabrication*. Academic Press, San Diego, 1985.

[3] Bahaa E. A. Saleh and Malvin Carl Teich. *Fundamentals of Photonics*. Wiley-Interscience, 1991.

[4] L. G. Cohen, W. L. Mammel, and S. J. Jang. Low-loss quadruple-clad single-mode lightguides with dispersion below 2 ps/km nm over the 1.28 μm1.65 μm wavelength range. *Electron. Lett.*, 18:1023–1024, 1982.

[5] R. H. Stolen and E. P. Ippen. Raman gain in glass optical waveguides. *Appl. Phys. Lett.*, 22:276–278, 1973.

[6] R. W. Tkach, A. R. Chraplyvy, and R. M. Derosier. Spontaneous Brillouin scattering for single-mode optical fiber characterization. *Electron. Lett.*, 22:1011–1013, 1986.

[7] J. J. Degnan. Theory of the optimally coupled Q-switched laser. *IEEE J. Quantum Electron.*, 25:1890–1901, 1989.

[8] J. Swiderski, A. Zajac, P. Konieczny, and M. Skorczakowski. Numerical model of a Q-switched double-clad fiber laser. *Opt. Express*, 12:3554–3559, 2004.

[9] K. Lu and N. K. Dutta. Spectroscopic properties of Yb-doped silica glass. *J. Appl. Phys.*, 91:576–581, 2002.

[10] R. Paschotta, J. Nilsson, A. C. Tropper, and D. C. Hanna. Ytterbium doped fiber amplifiers. *IEEE J. Quantum Eelectron.*, 33:1049–1056, 1997.

[11] S. Kuck, K. Petermann, U. Pohlmann, and G. Huber. Near-infrared emission of Cr -doped garnets: Lifetimes, quantum efficiencies, and emission cross sections. *Phys. Rev. B*, 51:17323–17331, 1995.

[12] J. A. Alvarez-Chavez, H. L. Offerhaus, J. Nilsson, W. A. Clarkson P. W. Turner, and D. J. Richardson. High-energy, high-power ytterbiumdoped Q-switched fiber laser,. *Opt. Lett.*, 25:37–39, 2000.

[13] C. C. Ranaud, H. L. Offerhaus, J. A. Alvarez-Chavez, C. J. Nilsson, W. A. Clarkson, P. W. Turner, D. J. Richardson, and A. B. Grudinin. Characteristics of Q-switched cladding-pumped ytterbium-doped fiber lasers with different high-energy fiber designs. *IEEE J. Quantum Electron.*, 37:199–206, 2001.

[14] A. Piper, A. Malinowski, K. Furusawa, and D. J. Richardson. High power, high-brightness, mJ Q-switched ytterbium-doped fibre laser. *Electron. Lett.*, 40:928–929, 2004.

[15] M. Laroche, H. Gilles, S. Girard, N. Passilly, and K. At-Ameur. Nanosecond pulse generation in a passively Q-switched Yb-doped fiber laser by Cr^{4+} :YAG saturable absorber. *IEEE Photon. Technol. Lett.*, 18:764–766, 2006.

[16] J. Y. Huang, H. C. Liang, K. W. Su, and Y. F. Chen. High power passively Q-switched ytterbium fiber laser with Cr^{4+} :YAG as a saturable absorber,. *Opt. Express*, 15:473–479, 2007.

[17] J. Y. Huang, H. C. Liang, K. W. Su, and Y. F. Chen. Analytical model for optimizing the parameters of an external passive Q-switched in fiber laser. *Appl. Opt.*, 47:2297–2302, 2008.

[18] R. Chi, K. Lu, and S. Chen. Multi-wavelength Yb-doped fiber ring laser. *Microwave Opt. Technol. Lett.*, 36:170–172, 2003.

[19] W. Guan and J. R. Marciante. Dual-frequency operation in a shortcavity ytterbium-doped fiber laser. *IEEE Photon. Technol. Lett.*, 19:261–263, 2007.

[20] L. R. Chen and X. J. Gu. Dual-wavelength yb-doped fiber laser stabilized through four-wave mixing. *Opt. Express*, 15:5083–5088, 2007.

[21] S. L. Hu, J. Yu, C. Q. Gao, G. H. Wei, and F. Y. L. Dual-wavelength stable nanosecond pulses generation from cladding-pumped fiber laser. *Chin. Opt. Lett.*, 4:655–657, 2006.

[22] V. N. Filippov, A. N. Starodumov, and A. V. Kiryanov. All-fiber passively Q-switched low-threshold erbium laser. *Opt. Lett.*, 26:343–345, 2001.

[23] V. N. Philippov, A. V. Kiryanov, and S. Unger. Advanced configuration of erbium fiber passively Q-switched laser with Co^{2+} :ZnSe crystal as saturable absorber. *IEEE Photon. Technol. Lett.*, 16:57–59, 2004.

[24] M. Laroche, A. M. Chardon, J. Nilsson, D. P. Shepherd, and W. A. Clarkson. Compact diode-pumped passively Q-switched tunable ErYb double-clad fiber laser. *Opt. Lett.*, 27:1080–1082, 2002.

[25] V. N. Philippov, J. Nilsson, W. A. Clarkson, V. E. Kisel A. Abdolvand, V. G. Shcherbitsky, N. V. Kuleshov, and V. I. Konstantinovand V. I. Levchenko. Passively Q-switched ErYb double-clad fiber laser with Cr $^{2+}$:ZnSe and Co^{2+} :MgAlO as a saturable absorber. *Proc. SPIE*, 5335:8–15, 2004.

[26] F. Z. Qamar and T. A. King. Passive Q-switching of the Tm-silica fibre laser near 2 μm by a Cr^{2+} :ZnSe saturable absorber crystal. *Opt. Commun.*, 248:501–508, 2005.

[27] U. Grebner and R. Koch. Passively Q-switched nd:glass fiber-bundle laser. *Electron. Lett.*, 31:205–206, 1995.

[28] C. Y. Lo, K. Y. Huang, J. C. Chen, C. Y. Chuang, C. C. Lai, S. L. Huang, Y. S. Lin, and P. S. Yeh. Double-clad Cr^{4+}:YAG crystal fiber amplifier. *Opt. Lett.*, 30:129–131, 2005.

[29] Y. C. Huang, J. S. Wang, Y. K. Lu, W. K. Liu, K. Y. Huang, S. L. Huang, and W. H. Cheng. Preform fabrication and fiber drawing of 300 nm broadband Cr-doped fibers. *Opt. Express*, 15:14382–14388, 2007.

[30] Y. Gan, X. J. Gu, J. Y. C. Koo, W. G. Liang, and C. Q. Xu. Second harmonic generation using an all-fiber Q-switched Yb-doped fiber laser and MgO:c-PPLN. *Advances in OptoElectronics*, 2008:Article ID 956908, 2008.

[31] C. Ye, P. Yan, L. Huang, Q. Liu, and M. Gong. Stimulated Brillouin scattering phenomena in a nanosecond linearly polarized Yb-doped double-clad fiber amplifier. *Laser Phys. Lett.*, 4:376–381, 2007.

[32] J. Noda, K. Okamoto, and Y. Sasaki. Polarization-maintaining fibers and their applications. *IEEE/OSA J. Lightwave Technol.*, LT-4:1071–1089, 1986.

[33] R. G. Smith. Optical power handling capacity of lowloss optical fibers as determined by stimulated raman and brillouin scattering. *Appl. Opt.*, 11:2489–2493, 1972.

[34] Y. Azuma, N. Shibata, T. Horiguchi, and M. Tateda. Wavelength dependence of brillouin-gain spectra for single-mode optical fibres. *Electron. Lett.*, 24:250–252, 1988.

[35] R. Courant and D. Hilbert. *Methods of Mathematical Physics , Volume 1 chapter 4*. New York: Interscience, 1953.

[36] Y. F. Chen, Y. P. Lan, and H. L. Chang. Analytical model for design criteria of passively Q-switched lasers. *IEEE J. Quantum Electron.*, 37:462–468, 2001.

[37] N. N. Ilichev, E. S. Gulyamova, and P. P. Pashinin. Passive Q-switching of a neodymium laser by a Cr^{4+} :YAG crystal switch. *Quantum Electron.*, 27:972–977, 1997.

[38] I.P. Alcock, A.C. Tropper, A.I. Ferguson, and D.C. Hanna. Q-switched operation of a neodymium-doped monomode fibre laser. *Electron. Lett.*, 22:84–85, 1986.

[39] P. R. Morkel, K. P. Jedrzejewski, and E. R. Taylor. Q-switched neodymium-doped phosphate glass fiber lasers. *IEEE J. Quantum Electron.*, 29:2178–2188, 1993.

[40] P. Myslinski, J. Chrostowski, J.A. Koningstein, and J.R. Simpson. High power Q-switched erbium doped fiber laser. *IEEE J. Quantum Electron.*, 28:371377, 1992.

[41] M. Sejka, C.V. Poulsen, J.H. Povlsen, Y. Shi, and O. Poulsen. High repetition rate Q-switched ring laser in Er doped fiber. *Opt. Fiber Technol.*, 1:167170, 1995.

[42] P. Roy and D. Pagnoux. Analysis and optimization of a Q-switched erbium doped fiber laser working with a short rise time modulator. *Opt. Fiber Technol.*, 2:235–240, 1996.

[43] G.P. Lees and T.P. Newson. Diode-pumped high power simultaneously Q-switched and self mode-locked erbium doped fiber laser. *Electron. Lett.*, 32:332–333, 1996.

[44] G.P. Lees, A. Hartog, A. Leach, and T.P. Newson. 980 nm diode pumped erbium3+ /ytterbium3+ doped Q-switched fibre laser. *Electron. Lett.*, 31:1836–1837, 1995.

[45] C. G. Zhao, Y. Liu, J. wang, and L. J. Wang. Cladding-pumped Er/Yb co-doped Q-switched all fiber laser. *Chin. Opt. Lett.*, 5:S115–S117, 2007.

149

[46] Y. Shi, J.P. Ragey, and O. Poulsen. Dye laser pumped Pr doped fiber lasers: Basic parameter investigation, CW operation, and Q-switched operation. *IEEE J. Quantum Eelectron.*, 29:14021406, 1993.

[47] P. Myslinski, X. Pan, C. Barnard, J. Chrostowski, B.T. Sullivan, and J.F. Bayon. Q-switched thulium-doped fiber laser. *Opt. Eng.*, 32:2025–2030, 1993.

[48] A. F. El-Sherif and T. A. King. High-peak-power operation of a Q-switched Tm-doped silica fiber laser operating near 2 μm. *Opt. Lett.*, 28:22–24, 2003.

[49] Y. Wang and C. Q. Xu. Actively Q-switched fiber lasers: Switching dynamics and nonlinear processes. *Prog. Quantum Electron.*, 31:131–216, 2007.

[50] M. Salhi, A. Hideur, T. Chartier, M. Brunel, G. Martel, and C. Ozkul. Evidence of Brillouin scattering in an ytterbium-doped double-clad fiber laser. *Opt. Lett.*, 27:1294–1296, 2002.

[51] Y. C. Zhao and S. D. Jackson. Passively Q-switched fiber laser that uses saturable Raman gain. *Opt. Lett.*, 31:751–753, 2006.

[52] B. N. Upadhyaya, U. Chakravarty, A. Kuruvilla, K. Thyagarajan, M. R. Shenoy, and S. M. Oak. Mechanisms of generation of multi-peak and mode-locked resembling pulses in Q-switched Yb-doped fiber lasers. *Opt. Express*, 15:1157611588, 2007.

[53] X. Y. Zhang, S. Z. Zhao, Q. P. Wang, Q. D. Zhang, L. K. Sun, and S. J. Zhang. Optimization of Cr-doped saturable-absorber-switched lasers. *IEEE J. Quantum Electron.*, 33:2286–2294, 1997.

[54] S. P. Ng, D. Y. Tang, L. J. Qian, and L. J. Qin. Satellite pulse generation in diode-pumped Q-switched Nd:GdVO$_4$ lasers. *IEEE J. Quantum Electron.*, 42:625–632, 2006.

[55] S. Forget, F. Druon, F. Balembois, P. Georges, N. Landru, J. P. Feve, J. Lin, and Z. Weng. Passively Q-switched diode-pumped Cr^{4+}:YAG/Nd^{3+}:GdVO$_4$ monolithic microchip laser. *Opt. Commun.*, 259:816–819, 2006.

[56] J. Dong, J. Lu, and K. Ueda. Experiments and numerical simulation of a diode-laser-pumped Cr, Nd:YAG self-Q-switched laser. *J. Opt. Soc. Am. B*, 12:2130–2136, 2004.

[57] X. Zhang, A. Brenier, Q. Wang, Z. Wang, J. Chang, S. Zhang P. Li, S. Ding, and S. Li. Passive Q switching characteristics of $Yb^{3+}:Gd_3Ga_5O_{12}$ crystal. *Opt. Express*, 13:7708–7719, 2005.

[58] D. Y. Tang, S. P. Ng, L. J. Qin, and X. L. Meng. Deterministic chaos in a diode-pumped Nd:YAG laser passively Q-switched by a Cr^{4+} :YAG crystal. *Opt. Lett.*, 28:325–327, 2003.

[59] S. Kuck, K. Petermann, and G. Huber. Spectroscopic investigation of the Cr^{4+} center in YAG. *Proc. Advanced Solid State Lasers*, 10:92–94, 1991.

[60] Y. Shimony, Z. Burstein, and Y. Kalisky. Cr:YAG as passive Q- switch and brewster plate in a pulsed Nd:YAG laser. *IEEE J. Quantum Electron.*, 31:17381741, 1995.

[61] G. Xiao, J. H. Lim, S. Yang, E. Van Stryland, M. Bass, and L. Weichman. Z-scan measurement of the ground and excited state absorption cross sections of Cr^{4+} in yttrium aluminum garnet. *IEEE J. Quantum Electron.*, 35:10861091, 1999.

[62] H. Eilers, K. R. Hoffman, W. M. Denis, S. M. Jacobson, and W. M. Yen. Saturation of 1.064 μm absorption in Cr, $Ca:Y_3Al_5O_{12}$ crystals. *Appl. Phys. Lett.*, 61:2958–2960, 1992.

[63] X. Y. Zhang, S. Z. Zhao, Q. P. Wang, S. T. wang, L. K. Sun, S. J. Zhang, G. T. Yao, and Z. Y. Zhang. Measurement of absorption cross section and ground state recovery time of Cr^{4+} doped saturable absorber. *J. of Optoelectronics.laser (In Chinese)*, pages 13–17, 1998 (06).

[64] L. G. Luo and P. L. Chu. Passive Q-switched erbium-doped fiber laser with saturable absorber. *Opt. Commun.*, 161:257–263, 1999.

[65] Y. M. Huo and P. K. Cheo. Modeling of passively Q-switched $Er^{3+}Yb^{3+}$-codoped clad-pumped fiber lasers. *IEEE J. Sel. Topics Quantum Electron.*, 11:658–665, 2005.

[66] Z. G. Li, Z. Xiong, N. Moore, G. C. Lim, W. L. Huang, and D. X. Huang. Amplified-spontaneous-emission effects in a passively Q-switched diode-pumped $Nd:YVO_4$ laser. *J. Opt. Soc. Amer. B*, 21:1479–1485, 2004.

[67] L. Pan, I. Utkin, and R. Fedosejevs. Passively Q-switched ytterbium doped double-clad fiber laser with a Cr^{4+} :YAG saturable absorber. *IEEE Photon. Technol. Lett.*, 19:1979–1981, 2007.

[68] L. Pan, I. Utkin, and R. Fedosejevs. Experiment and numerical modeling of high power passively Q-switched ytterbium doped double-clad fiber lasers. *IEEE J. Quantum Electron.*, 46:68–75, 2010.

[69] J. Li, K. Ueda, J. Dong, M. Musha, and A. Shirakawa. Maximum value of the pulse energy of a passively Q-switched laser as a function of the pump power. *Appl. Opt.*, 45:5377–5384, 2006.

[70] J. Liu, B. Ozygus, S. Yang, J. Erhard, U. Seelig, A. Ding, H. Weber, X. Meng, L. Zhu, L. Qin, C. Du, X. Xu, and Z. Shao. Efficient passive Q-switching operation of a diode-pumped Nd:GdVO$_4$ laser with a Cr^{4+}:YAG saturable absorber. *J. Opt. Soc. Amer. B*, 20:652–661, 2003.

[71] S. V. Voitikov, A. A. Demidovich, L. E. Batay, A. N. Kuzmin, and M. B. Danailov. Sub-nanosecond pulse dynamics of Nd:LSB microchip laser. *Opt. Commun.*, 251:154–164, 2005.

[72] A. Sennaroglu. Continuous wave thermal loading in saturable absorbers: theory and experiment. *Appl. Opt.*, 36:9528–9535, 1997.

[73] Y. Wang and C. Q. Xu. Modeling and optimization of Q-switched double-clad fiber lasers. *Appl. Opt.*, 45:2058–2071, 2006.

[74] H. Ridderbusch and T. Graf. Saturation of 1047 and 1064 nm absorption in Cr^{4+} :YAG crystals,. *IEEE J. Quantum Electron.*, 43:168–173, 2007.

[75] S. Li, S. Zhou, P. Wang, Y. C. Chen, and K. K. Lee. Self-Q-switched diode-end-pumped Cr,Nd:YAG laser with polarized output. *Opt. Lett.*, 18:203–205, 1993.

[76] T. Y. Fan. Effect of finite lower level lifetime on Q-switched lasers. *IEEE J. Quantum Electron.*, 24:2345–2349, 1988.

[77] J. J. Gegnan, D. B. Coyle, and R. B. Kay. Effects of thermalization on Q-switched laser properties. *IEEE J. Quantum Electron.*, 34:887–899, 1998.

[78] H. M. Pask, R. J. Carman, D. C. Hanna, A. C. Tropper, C. J. Mackechnie, P. R. Barber, and J. M. Dawes. Ytterbium doped silica fiber lasers: Versatile sources for the $1-1.2$ μm region. *IEEE J. Sel. Topics Quantum Electron.*, 1:2–13, 1995.

[79] M. K. Davis, M. J. F. Digonnet, and R. H. Pantell. Thermal effects in doped fibers. *J. Lightw. Technol.*, 16:1013–1023, 1998.

[80] X. Feng, Y. Liu, S. Fu, S. Yuan, and X. Dong. Switchable dual-wavelength ytterbium-doped fiber laser based on a few-mode fiber grating. *IEEE Photon. Technol. Lett.*, 16:762–764, 2004.

[81] C. Tu, W. Guo, Y. Li, S. Zhang, , and F. Lu. Stable multiwavelength and passively mode-locked Yb-doped fiber laser based on nonlinear polarization rotation. *Opt. Commun.*, 280:448–452, 2007.

[82] L. Pan, I. Utkin, and R. Fedosejevs. Two-wavelength ytterbium doped fiber laser with sustained relaxation oscillation. *Appl. Opt.*, 48:5484–5489, 2009.

[83] A. Hideur, T. Chartier, C. Ozkul, and F. Sanchez. Dynamics and stabilization of a high power side-pumped Yb-doped double-clad fiber laser. *Opt. Commun.*, 186:311–317, 2000.

[84] J. L. Li, K. I. Ueda, M. Musha, and A. Shirakawa. Residual pump light as a probe of self-pulsing instability in an ytterbium- doped fiber laser. *Opt. Lett.*, 31:1450–1452, 2006.

[85] A. M. Rios, I. T. Gomez, G. A. Sanchez, , and R. S. Aguilar. Selfpulsing in a double-clad ytterbium fiber laser induced by high scattering loss. *Opt. Commun.*, 281:663–667, 2008.

[86] A. V. Kiryanov and Y. O. Barmenkov. Self-Q-switched ytterbium-doped all-fiber laser. *Laser Phys. Lett.*, 3:498–502, 2006.

[87] A. V. Kiryanov, Y. O. Barmenkov, I. L. Martinez, A. S. Kurkov, and E. M. Dianov. Cooperative luminescence and absorption in ytterbium-doped silica fiber and the fiber nonlinear transmission coefficient at λ =980 nm with a regard to the ytterbium ion-pairs effect. *Opt. Express*, 14:39813992, 2006.

[88] J. Kong, D. Y. Tang, J. Lu, and K. Ueda. Random-wavelength solid-state laser. *Opt. Lett.*, 29:65–67, 2004.

[89] D. A. Grukh, A. S. Kurkov, V. M. Paramonov, and E. M. Dianov. Effect of heating on the optical properties of Yb^{3+}-doped fibers and fibre lasers. *Quantum Electron.*, 34:579–582, 2004.

[90] T. C. Newell, P. Peterson, A. Gavrielides, and M. P. Sharma. Temperature effects on the emission properties of Yb-doped optical fibers. *Opt. Commun.*, 273:256–259, 2007.

[91] L. Pan, I. Utkin, and R. Fedosejevs. Two-wavelength passively Q-switched ytterbium doped fiber laser. *Opt. Express*, 16:11858–11870, 2008.

[92] J. J. Zayhowski and C. Dill III. Diode-pumped passively Q-switched picosecond microchip lasers. *Opt. Lett.*, 19:1427–1429, 1994.

[93] M. D. Wei, C. H. Chen, and K. C. Tu. Spatial and temporal instabilities in a passively Q-switched Nd:YAG laser with a Cr^{4+}:YAG saturable absorber. *Opt. Express*, 12:3972–3980, 2004.

[94] Y. X. Fan, F. Y. Lu, S. L. Hu, K. C. Lu, H. J. Wang, G. Y. Zhang, and X. Y. Dong. Narrow-linewidth widely tunable hybrid Q-switched double-clad fiber laser. *Opt. Lett.*, 28:537–539, 2003.

[95] S. V. Chernikov, Y. Zhu, J. R. Taylor, and V. P. Gapontsev. Super-continuum self Q-switched ytterbium fiber laser. *Opt. Lett.*, 22:298–300, 1997.

[96] A. A. Fotiadi, P. Megret, and M. Blondel. Dynamics of a self Q-switched fiber laser with a rayleigh-stimulated brillouin scattering ring mirror. *Opt. Lett.*, 29:1078–1080, 2004.

[97] Z. J. Chen, A. B. Grudinin, J. Porta, and J. D. Minelly. Enhanced Q-switching in double-clad fiber lasers. *Opt. Lett.*, 23:454–456, 1998.

[98] Y.-X. Fan, F.-Y. Lu, S.-L. Hu, K.-C. Lu, H.-J. Wang, J.-L. He X.-Y. Dong, and H.-T.Wang. Tunable high-peak-power, high-energy hybrid Q-switched double-clad fiber laser. *Opt. Lett.*, 29:724–726, 2004.

[99] L. Pan, I. Utkin, R. J. Lan, Y. Godwal, and R. Fedosejevs. High peak power sub-nanosecond passively Q-switched ytterbium doped fiber laser. *Opt. Lett.*, 35:895–897, 2010.

[100] N. Andermahr and C. Fallnich. Modeling of transverse mode interaction in large-mode-area fiber amplifiers. *Opt. Express*, 16:20038–20046, 2008.

[101] A. Fotiadi, G. Ravet, P. Megret, and M. Blondel. Characterization of all-fiber rayleigh-sbs ring mirror. *Proceedings Symposium IEEE/LEOS Benelux Chapter*, pages 189–192, 2003.

[102] A. Fotiadi and P. Megret. Self-q-switched er-brillouin fiber source with extra-cavity generation of a raman supercontinuum in a dispersion-shifted fiber. *Opt. Lett.*, 31:1621–1623, 2006.

[103] Z. Pan, L. Meng, Q. Ye, H. Cai, Z. Fang, and R. Qu. Repetition rate stabilization of the sbs Q-switched fiber laser by external injection. *Opt. Express*, 17:3124–3129, 2009.

[104] C. C. Lai, H. J. Tsai, K. Y. Huang, K.-Y. Hsu, Z.-W. Lin, K. D. Ji, W. J. Zhuo, and S. L. Huang. Cr^{4+}:YAG double-clad crystal fiber laser. *Opt. Lett.*, 33:2919–2921, 2008.

[105] A. K. Jafari and M. Aas. Continuous-wave theory of yb:yag end-pumped thin-disk lasers. *Appl. Opt.*, 48:106113, 2009.

[106] S. Torogh, A. K. Jafari, and A. H. Golpayegani. A model of lasing action in a quasi-four-level thin active media. *IEEE J. Quantum Electron.*, 46:871–876, 2010.

Appendix I:
Matlab codes for simulations

Program 1

This is a multi-wavelength model, which simulates the laser spectrum.

Part I: Provides initial values for the variables in simulation

```
clear all;
lamdas=[1.03E-6%Signal wavelengths
1.032E-6
1.034E-6
1.036E-6
1.038E-6
1.04E-6
1.042E-6
1.044E-6
1.046E-6
1.048E-6
1.05E-6
1.052E-6
1.054E-6
1.056E-6
1.058E-6
1.06E-6
1.062E-6
1.064E-6
1.066E-6
1.068E-6
1.07E-6
1.072E-6
1.074E-6
1.076E-6
1.078E-6
1.08E-6
1.082E-6
```

```
1.084E-6
1.086E-6
1.088E-6
1.09E-6
1.092E-6
1.094E-6
1.096E-6
1.098E-6
1.1E-6];
xegmaas=[6.19E-26%Absorption cross sections
5.49E-26
4.83E-26
4.26E-26
3.78E-26
3.34E-26
2.92E-26
2.5E-26
2.1E-26
1.75E-26
1.45E-26
1.2E-26
9.87E-27
8.82E-27
8.38E-27
7.65E-27
6.69E-27
5.6E-27
4.48E-27
3.43E-27
2.51E-27
1.75E-27
1.16E-27
7.34E-28
4.41E-28
2.51E-28
1.36E-28
6.94E-29
3.35E-29
1.53E-29
6.55E-30
2.64E-30
9.99E-31
3.54E-31
1.17E-31
3.6E-32];
```

```
xegmaes=[6.73E-25 %Emission cross sections
6.66E-25
6.49E-25
6.33E-25
6.14E-25
5.86E-25
5.52E-25
5.17E-25
4.76E-25
4.35E-25
3.95E-25
3.57E-25
3.21E-25
3E-25
2.84E-25
2.78E-25
2.72E-25
2.66E-25
2.59E-25
2.53E-25
2.47E-25
2.4E-25
2.34E-25
2.28E-25
2.21E-25
2.15E-25
2.09E-25
2.02E-25
1.96E-25
1.89E-25
1.83E-25
1.76E-25
1.7E-25
1.63E-25
1.57E-25
1.5E-25];

xegmagsa=4.3e-22*[1.14812 %Ground state absorption cross
section of saturable absorber
1.14944
1.15077
1.14944
1.14812
1.14547
1.14087
```

```
1.14416
1.13662
1.12366
1.10304
1.08444
1.07227
1.06326
1.04992
1.0253
1.00556
1
0.97644
0.94533
0.91832
0.9
0.88
0.86
0.8413
0.82818
0.81314
0.79836
0.7859
0.7716
0.75754
0.74567
0.73204
0.72053
0.71295
0.713];

xegmaesa=8.2e-23*[1.14812%Excited state absorption cross sections
of saturable absorber
1.14944
1.15077
1.14944
1.14812
1.14547
1.14087
1.14416
1.13662
1.12366
1.10304
1.08444
1.07227
1.06326
```

159

```
1.04992
1.0253
1.00556
1
0.97644
0.94533
0.91832
0.9
0.88
0.86
0.8413
0.82818
0.81314
0.79836
0.7859
0.7716
0.75754
0.74567
0.73204
0.72053
0.71295
0.713];

NA=0.15; %Fiber numerical aperture
dcore=5.4e-6;%Fiber core diameter
dclad=125e-6;%Inner cladding diameter
SecNo=50;%Fiber sections divided in simulation
L=3;%Fiber length
alfap=0.005;%Loss of the signal in fiber per meter
alfas=0.005;%Loss of the pump in fiber per meter
nfiber=1.45;%Refractive index of the fiber
n0=9e25;(Doping level of the fiber
nsa=6.22e23;%Doping level of SA
taosa=4e-6;%Excited level life time of SA
lsa=0.0045;%Thickness of SA
dsa=50e-6;(Effective focal diameter in SA)
Asa=pi*dsa$^2$/4;%Effective focal area in SA
c0=3e8;%Light speed in vacuum
h=6.626e-34;%plank constant
vg=c0/nfiber;%Group velocity
SigNo=36; %Wavelength number
deltax=L/SecNo;%Length of each step along fiber
deltat=L/(SecNo*vg);%Length of each step in time
deltalamda=100e-9/(SigNo-1);%Separation of the wavelengths
Aco=pi*(dcore/2)$^2$;%Fiber core diameter
```

```
lamdap=976e-9;%pump wavelength
gamap=dcore$^2$/(dclad$^2$);(overlap factor between the pump and
doped area)
xegmaep=2.44e-24;(Emission cross section at pump wavelength)
xegmaap=2.5e-24;(Absorption cross section at pump wavelength)
tao=850e-6;(Lifetime of Yb fiber)

for q=1:length(lamdas)%Calculate overlap factors
V(q)=2*pi*dcore*NA/(2*lamdas(q));
w(q)=(dcore/2)*(0.65+1.619*V(q)$^{(-1.5)}$+2.876*V(q)$^{(-6)}$);
gamas(q)=1-exp(-(2*dcore$^2$/(4*w(q)$^2$)));
end

gamas=reshape(gamas,SigNo,1);

(Give initial value for each variable)
for s=1:SecNo+1
 n2(s,1)=0;
 ppm(s,1)=0;
  for ch=1:SigNo
   psp(s,1,ch)=0;
   psm(s,1,ch)=0;
  end
end

nsa2(1)=0;
```

Part II: This is a iterative program, which simulates Q-switched progress without SBS.

```
clear inversion;
clear averagepower1;
clear averagepower2;
clear averagepower3;
clear averagepower4;
clear averagepower5;
clear averagepower;
clear SA;

pumppower=10.1;
tt=400;
TimeSec=10.9999*deltat;
ppm(SecNo,1)=pumppower;
for qq=1:tt
```

```
time=0:deltat:TimeSec;
for t=1:length(time)
    for s=1:(SecNo-1)
            n2(s,2)=n2(s,1)+deltat*((gamap*lamdap/(h*c0*Aco))
            *(xegmaap*(n0-n2(s,1))-xegmaep*n2(s,1))*ppm(s,1)+
            sum((gamas.*lamdas/(h*c0*Aco)).*(xegmaas*(n0-n2(s,1))
            -xegmaes*n2(s,1)).*reshape((psp(s,1,:)+psm(s,1,:)),
            SigNo,1))-n2(s,1)/tao);

            ppm(s,2)=ppm(s+1,1)+deltax*(gamap*(xegmaep*n2(s+1,1)
            -xegmaap*(n0-n2(s+1,1)))*ppm(s+1,1)-alfap*ppm(s+1,1));

        for ch=1:SigNo
            psm(s,2,ch)=psm(s+1,1,ch)+deltax*(gamas(ch)*(xegmaes(ch)
            *n2(s+1,1)-xegmaas(ch)*(n0-n2(s+1,1)))*psm(s+1,1,ch)
            +2*gamas(ch)*xegmaes(ch)*n2(s+1,1)*h*c0*c0*deltalamda/
            (lamdas(ch))^3-alfas*psm(s+1,1,ch));

            psp(s+1,2,ch)=psp(s,1,ch)+deltax*(gamas(ch)*(xegmaes(ch)
            *n2(s,1)-xegmaas(ch)*(n0-n2(s,1)))*psp(s,1,ch)+2*gamas(ch)
            *xegmaes(ch)*n2(s,1)*h*c0*c0*deltalamda/(lamdas(ch))^3
            -alfas*psp(s,1,ch));
        end
    end

    n2(SecNo,2)=n2(SecNo,1)+deltat*((gamap*lamdap/(h*c0*Aco))*
    (xegmaap*(n0-n2(SecNo,1))-xegmaep*n2(SecNo,1))*ppm(SecNo,1)+
    sum((gamas.*lamdas/(h*c0*Aco)).*(xegmaas*(n0-n2(SecNo,1))-
    xegmaes*n2(SecNo,1)).*reshape((psp(SecNo,1,:)+psm(SecNo,1,:)),
     SigNo,1))-n2(SecNo,1)/tao);

    nsa2(2)=nsa2(1)+deltat*(sum(reshape((psp(1,2,:)+psm(1,2,:))
    , SigNo,1).*xegmagsa.*lamdas)*(nsa-nsa2(1))/(2*Asa*h*c0)
    -nsa2(1)/taosa);

        ppm(SecNo,2)=pumppower;
        for ch=1:SigNo
          T(ch)=exp(-2*lsa*(xegmagsa(ch)*(nsa-nsa2(2))
          +xegmaesa(ch)*nsa2(2)));
          psm(SecNo,2,ch)=psp(SecNo,1,ch)*0.04;
          psp(1,2,ch)=psm(1,1,ch)*0.85*0.85*T(ch);
        end
        nsa2(1)=nsa2(2);
            for s=1:SecNo
                n2(s,1)=n2(s,2);
```

162

```
                    ppm(s,1)=ppm(s,2);
                    for ch=1:SigNo
                        psm(s,1,ch)=psm(s,2,ch);
                        psp(s,1,ch)=psp(s,2,ch);
                    end
                end
end

inversion(qq)=sum(n2(:,2))/SecNo;
averagepower1(qq)=psp(SecNo,2,1);
averagepower2(qq)=psp(SecNo,2,2);
averagepower3(qq)=psp(SecNo,2,3);
averagepower4(qq)=psp(SecNo,2,4);
averagepower5(qq)=psp(SecNo,2,5);
averagepower(qq)=sum(psp(SecNo,2,:));
```

Program 2

This is a single-wavelength model, in which travel wave model is also employed to saturable absorber.

Part I: Provide initial values for the variables in simulation

```
clear all;
lamdas=1.074E-6;
xegmaas=1.16E-27;
xegmaes=2.34E-25;
xegmagsa=0.87*4.3e-22;
xegmaesa=0.87*1.075e-22;
NA=0.15;
dcore=5.4e-6;% fiber core diameter
dclad=125e-6;
SecNo=200;
SigNo=1;
L=3;
R=0.04;
alfap=0.005;
alfas=0.005;
alfasa=20;
nfiber=1.45;
n0=9e25;
c0=3e8;
V=2*pi*dcore*NA/(2*lamdas);
    w=(dcore/2)*(0.65+1.619*V^(-1.5)+2.879*V^(-6));
    gamas=1-exp(-(2*dcore^2/(4*w^2)));
```

```
wsa0=7.2e-6;% Focused beam waist in SA
nsa=6.22e23;
nSA=1.8;
taosa=1e-6;
lsa=0.0025;
SecNo1=50;
z0=pi*wsa0*wsa0*nSA/(lamdas);
for q=1:SecNo1+1
    z(q)=(lsa/(SecNo1-1))*(q-(2+SecNo1)/2);
    wsa(q)=wsa0*sqrt(1+(z(q)/z0)^2);
    Asa(q)=pi*wsa(q)^2;
end
h=6.626e-34;%plank constant
vg=c0/nfiber;
vg1=c0/nSA;
SigNo=1;
deltax1=lsa/SecNo1;
deltat1=lsa/(SecNo1*vg1);
deltax=L/SecNo;
deltat=L/(SecNo*vg);
deltalamda=3e-6;
Aco=pi*(dcore/2)^2;
lamdap=976e-9;% pump wavelength
gamap=dcore^2/(dclad^2);% overlap factor between the pump
and doped area

xegmaep=2.44e-24;
xegmaap=2.5e-24;
tao=850e-6;

for ss1=1:SecNo1+1
    nsa2(ss1,1)=100;
      pspSA(ss1,1)=0;
      psmSA(ss1,1)=0;
end
for s=1:SecNo+1
    n2(s,1)=100;
%     n1(s,1)=n0-n2(s,1);
    ppm(s,1)=0.0;
      psp(s,1)=0.0;
      psm(s,1)=0.0;
  end


    Part II: Iterative part
```

```
clear averagepower;
clear inversion;
pumppower=10.1;(Pump power in watt)
tt=3000;(Simulation time, can choose any value)
ppm(SecNo,1)=pumppower;

TimeSec=deltat*15;

for qq=1:tt
time=deltat:deltat:TimeSec;

for t=1:length(time)
ppm(SecNo+1,2)=pumppower;


  for s=1:SecNo

  n2(s,2)=n2(s,1)+deltat*((gamap*lamdap/(h*c0*Aco))*(xegmaap*
  (n0-n2(s,1))-xegmaep*n2(s,1))*ppm(s,1)+(gamas*lamdas/(h*c0*Aco))
  *(xegmaas*(n0-n2(s,1))-xegmaes*n2(s,1))*(psp(s,1)+psm(s,1))
  -n2(s,1)/tao);

  ppm(s,2)=ppm(s+1,1)+deltax*(gamap*(xegmaep*n2(s+1,1)-xegmaap*
  (n0-n2(s+1,1)))*ppm(s+1,1)-alfap*ppm(s+1,1));

  psm(s,2)=psm(s+1,1)+deltax*(gamas*(xegmaes*n2(s+1,1)-xegmaas*
  (n0-n2(s+1,1)))*psm(s+1,1)+2*gamas*xegmaes*n2(s+1,1)*h*c0*c0*
  deltalamda/(lamdas)$^3$-alfas*psm(s+1,1));

  psp(s+1,2)=psp(s,1)+deltax*(gamas*(xegmaes*n2(s,1)-xegmaas*
  (n0-n2(s,1)))*psp(s,1)+2*gamas*xegmaes*n2(s,1)*h*c0*c0*
  deltalamda/(lamdas)$^3$-alfas*psp(s,1));

  end


n2(SecNo+1,2)=n2(SecNo+1,1)+deltat*((gamap*lamdap/(h*c0*Aco))
*(xegmaap*(n0-n2(SecNo+1,1))-xegmaep*n2(SecNo+1,1))
*ppm(SecNo+1,1)+(gamas*lamdas/(h*c0*Aco))*(xegmaas*
(n0-n2(SecNo+1,1))-xegmaes*n2(SecNo+1,1))*(psp(SecNo+1,1)
+psm(SecNo+1,1))-n2(SecNo+1,1)/tao);


for s1=1:SecNo1
```

```
nsa2(s1,2)=nsa2(s1,1)+deltat*(((pspSA(s1,1)+psmSA(s1,1))*
xegmagsa*lamdas)*(nsa-nsa2(s1,1))/(Asa(s1)*h*c0)-nsa2(s1,1)/taosa);

psmSA(s1,2)=psmSA(s1+1,1)-deltax1*(xegmaesa*nsa2(s1+1,1)
+xegmagsa*(nsa-nsa2(s1+1,1))-alfasa)*psmSA(s1+1,1);

pspSA(s1+1,2)=pspSA(s1,1)-deltax1*(xegmaesa*nsa2(s1,1)
+xegmagsa*(nsa-nsa2(s1,1))-alfasa)*pspSA(s1,1);

end

nsa2(SecNo1+1,2)=nsa2(SecNo1+1,1)+deltat*(((pspSA(SecNo1+1,1)
+psmSA(SecNo1+1,1))*xegmagsa*lamdas)*(nsa-nsa2(SecNo1+1,1))/
(Asa(SecNo1+1)*h*c0)-nsa2(SecNo1+1,1)/taosa);

psmSA(SecNo1+1,2)=0.85*psm(1,1);
pspSA(1,2)=psmSA(1,1);
psp(1,2)=0.85*pspSA(SecNo1+1,1);
psm(SecNo+1,2)=psp(SecNo+1,1)*0.04*0.85;

    for s1=1:SecNo1+1
      nsa2(s1,1)=nsa2(s1,2);
      psmSA(s1,1)=psmSA(s1,2);
      pspSA(s1,1)=pspSA(s1,2);
    end

      for s=1:SecNo+1
          n2(s,1)=n2(s,2);
          ppm(s,1)=ppm(s,2);
          psm(s,1)=psm(s,2);
          psp(s,1)=psp(s,2);
      end
 end

averagepower(qq)=0.96*psp(SecNo+1,2);
inversion(qq)=sum(n2(:,2))/(SecNo+1);

end
```

Program 3

This program simulates the passively Q-switched Yb doped fiber laser with Stimulated Brillouin scattering (SBS)

Part I: Provides initial values for the variables in simulation

```
clear all;
```

```matlab
SigNo=6;% Up to 5 orders of Stokes are included
for ch=1:SigNo
    lamdas(ch)=1.033e-6;
    xegmaas(ch)=5.15E-26;
    xegmaes(ch)=6.61E-25;
    xegmagsa(ch)=4.92e-22;
    xegmaesa(ch)=4.92e-22/7;
end

lamdas=reshape(lamdas,SigNo,1);
xegmaas=reshape(xegmaas,SigNo,1);
xegmaes=reshape(xegmaes,SigNo,1);
xegmagsa=reshape(xegmagsa,SigNo,1);
xegmaesa=reshape(xegmaesa,SigNo,1);
lamdap=976e-9;
xegmaep=2.44e-24;% emission cross section for the pump light
xegmaap=2.5e-24;% absorption cross section for the pump light
h=6.626e-34;%plank constant
nfiber=1.5;% fiber refractive index
c0=3e8;% light speed in vacuum
vg=c0/nfiber;% light velocity in fiber
dcore=25e-6;% Yb fiber core diameter
Aco=pi*(dcore/2)^2;% fiber core area
dclad=250e-6;% Yb fiber clading diameter
n0=9e25;% fiber Yb ion doping level (/m3)
tao=850e-6;% upper level lifetime of Yb ion
NA=0.07;% fiber numerical aperture
alfap=0.005;% pump light loss along fiber
alfas=0.005;% signal light loss along fiber
L=1;% Yb fiber length
SecNo=250;% how many sections the fiber was cut in the simulation
deltax=L/SecNo;% dL
deltat=L/(SecNo*vg);%dt
deltalamda=3e-12;% ASE emission bandwidth

for q=1:length(lamdas)
    V(q)=2*pi*dcore*NA/(2*lamdas(q));% V number for each wavelength
    w(q)=(dcore/2)*(0.65+1.619*V(q)^(-1.5)+2.876*V(q)^(-6));
    % mode field diameter (MFD)for each wavelength
    gamas(q)=1-exp(-(2*dcore^2/(4*w(q)^2)));% overlap factor
     for each wavelength
end

gamas=reshape(gamas,SigNo,1);
gamap=dcore^2/(dclad^2);% overlap factor between the pump
```

and doped area

```
lsa=0.0045;% saturable absorber thickness
dsa=150e-6;%saturable absorber effective focal diameter
taosa=4e-6;% saturable absorber upper level life time
nsa=6.22e23;% saturable absorber doping level (/m3)
Asa=pi*dsa^2/4;%saturable absorber averaged focal diameter
Aeff=pi*w(1)^2;

%initial values for each section of the fiber
for s=1:SecNo+1
    n2(s,1)=0;%upper level number of Yb ion
    ppm(s,1)=0;%pump light power
    for ch=1:SigNo
      Roum(s,1,ch)=0;
      Roup(s,1,ch)=0;
    end
    Esp(s,1,1)=1e-4;% positive direction signal power
    Esm(s,1,1)=1e-4;
    Psbs=1e-8;
    for ch=2:SigNo
      Esp(s,1,ch)=Psbs*(SigNo-ch);
      % positive direction signal power
      Esm(s,1,ch)=Psbs*(SigNo-ch);
      % negative direction signal power
  end
end

nsa2(1)=0;%initial values for each section of the fiber
gB=5e-11;%SBS gain coefficient
Trou=5e-9;%Relaxation time of acoustic wave
kB=1.38e-23;%Boltzmann constant
TB=300;%Temperature
va=5.96e3;% Sound speed in fiber
Q=sqrt(kB*TB*Aco*vg/(2*gB*va));%Acoustic noise intensity
```

Part II: Iterative program, which simulate Q-switched progress with SBS.

```
%We need clear these variables before we start a new round
clear inversion;
clear averagepower;
clear SA;
clear Rou;
noi=0;
kesai=2*gamas(1)*xegmaes(1)*h*c0*c0*deltalamda/(lamdas(1))^3;
```

```matlab
%For spontaneous emission

pumppower=4;% Pump power in (Watt)
tt=300; % ulse train sampling number
% TimeSec=3.9999*deltat;%time sampling gap 10*deltat=1.8ns
ppm(SecNo+1,1)=pumppower;% Border initivalue
for qq=1:tt

TimeSec=deltat;

    for s=1:SecNo
            n2(s,2)=n2(s,1)+deltat*((gamap*lamdap/(h*c0*Aco))
            *(xegmaap*(n0-n2(s,1))-xegmaep*n2(s,1))*ppm(s,1)
            +sum((gamas.*lamdas/(h*c0*Aco)).*(xegmaas*(n0-n2(s,1))
            -xegmaes*n2(s,1)).*reshape((Esp(s,1,:).^2
            +Esm(s,1,:).^2), SigNo,1))-n2(s,1)/tao);

            ppm(s,2)=ppm(s+1,1)+deltax*(gamap*(xegmaep*n2(s+1,1)
            -xegmaap*(n0-n2(s+1,1)))*ppm(s+1,1)-alfap*ppm(s+1,1));

            for ch=1:SigNo
                if ch==1
                    Esm(s,2,ch)=Esm(s+1,1,1)+deltax*(gamas(1)*
                    (xegmaes(1)*n2(s+1,1)-xegmaas(1)*(n0-n2(s+1,1)))
                    *Esm(s+1,1,1)/2-gB*Esp(s+1,1,2)*Roum(s+1,1,1)
                    /(2*Aeff)+kesai*n2(s+1,1)/abs(Esm(s+1,1,1)));

                    Esp(s+1,2,ch)=Esp(s,1,1)+deltax*(gamas(1)*
                    (xegmaes(1)*n2(s,1)-xegmaas(1)*(n0-n2(s,1)))
                    *Esp(s,1,1)/2-gB*Esm(s,1,2)*Roup(s,1,1)/
                    (2*Aeff)+kesai*n2(s+1,1)/abs(Esm(s+1,1,1)));

                elseif ch==SigNo

                    Esm(s,2,ch)=Esm(s+1,1,SigNo)+deltax*(gamas(SigNo)
                    *(xegmaes(SigNo)*n2(s+1,1)-xegmaas(SigNo)*
                    (n0-n2(s+1,1)))*Esm(s+1,1,SigNo)/2+
                    Esp(s+1,1,SigNo-1)*Roup(s+1,1,SigNo-1)*gB/(2*Aeff));

                    Esp(s+1,2,ch)=Esp(s,1,SigNo)+deltax*(gamas(SigNo)
                    *(xegmaes(SigNo)*n2(s,1)-xegmaas(SigNo)*
                    (n0-n2(s,1)))*Esp(s,1,SigNo)/2+Esm(s,1,SigNo-1)
                    *Roum(s,1,SigNo-1)*gB/(2*Aeff));

                else
```

169

```
          Esm(s,2,ch)=Esm(s+1,1,ch)+deltax*(gamas(ch)*
          (xegmaes(ch)*n2(s+1,1)-xegmaas(ch)*
          (n0-n2(s+1,1)))*Esm(s+1,1,ch)/2+(Esp(s+1,1,ch-1)
          *Roup(s+1,1,ch-1)-Esp(s+1,1,ch+1)*Roum(s+1,1,ch))
          *gB/(2*Aeff));

          Esp(s+1,2,ch)=Esp(s,1,ch)+deltax*(gamas(ch)*
          (xegmaes(ch)*n2(s,1)-xegmaas(ch)*(n0-n2(s,1)))
          *Esp(s,1,ch)/2+(Esm(s,1,ch-1)*Roum(s,1,ch-1)
          -Esm(s,1,ch+1)*Roup(s,1,ch))*gB/(2*Aeff));
        end

    end
  end

n2(SecNo+1,2)=n2(SecNo+1,1)+deltat*((gamap*lamdap/(h*c0*Aco))
*(xegmaap*(n0-n2(SecNo+1,1))-xegmaep*n2(SecNo+1,1))*
ppm(SecNo+1,1)+sum((gamas.*lamdas/(h*c0*Aco)).*(xegmaas*
(n0-n2(SecNo+1,1))-xegmaes*n2(SecNo+1,1)).*
reshape((Esp(SecNo+1,1,:).^2+Esm(SecNo+1,1,:).^2), SigNo,1))
-n2(SecNo+1,1)/tao);

nsa2(2)=nsa2(1)+deltat*(sum(reshape((Esp(1,2,:).^2+
Esm(1,2,:).^2), SigNo,1).*xegmagsa.*lamdas)*(nsa-nsa2(1))
/(2*Asa*h*c0)-nsa2(1)/taosa);

ppm(SecNo+1,2)=pumppower;

    % border values
    for ch=1:SigNo
      T(ch)=exp(-2*lsa*(xegmagsa(ch)*(nsa-nsa2(2))+xegmaesa(ch)
      *nsa2(2)));%Saturable absorber transmisison
      Esm(SecNo+1,2,ch)=Esp(SecNo+1,1,ch)*sqrt(0.04);
      %output coupler
      Esp(1,2,ch)=Esm(1,1,ch)*sqrt(0.85*0.85*T(ch));
      %Saturable absorber
       transmisison and cavity round trip loss
    end
    for s=1:SecNo+1
        for ch=1:SigNo-1
          Roum(s,2,ch)=Roum(s,1,ch)+deltat*(Esm(s,1,1)
          *Esp(s,1,ch+1)-Roum(s,1,ch)+noi)/Trou;

          Roup(s,2,ch)=Roup(s,1,ch)+deltat*(Esp(s,1,ch)
```

```
                 *Esm(s,1,ch+1)-Roup(s,1,ch)+noi)/Trou;

            end
        end
        % all the values from time 2 are transfered to time 1
         used as initial values for next itineracy

        nsa2(1)=nsa2(2);
            for s=1:SecNo+1
                n2(s,1)=n2(s,2);
                ppm(s,1)=ppm(s,2);
                for ch=1:SigNo
                    Esm(s,1,ch)=Esm(s,2,ch);
                    Esp(s,1,ch)=Esp(s,2,ch);
                    Roum(s,1,ch)=Roum(s,2,ch);
                    Roup(s,1,ch)=Roup(s,2,ch);
                end
end

inversion(qq)=sum(n2(:,2))/(SecNo+1);% averged inversion
 number along fiber

  for ch=1:SigNo
  averagepower(qq,ch)=0.96*sum(Esp(SecNo+1,2,ch).^2);
  end

SA(qq)=nsa2(2);% SA upper level number with time
Rou(qq)=Roup(SecNo,2,1);

end

subplot(3,3,1);plot(TimeSec:TimeSec:tt*TimeSec, averagepower(:,1));
xlabel('stoke0');
subplot(3,3,2);plot(TimeSec:TimeSec:tt*TimeSec, averagepower(:,2));
xlabel('stoke1');
subplot(3,3,3);plot(TimeSec:TimeSec:tt*TimeSec, averagepower(:,3));
xlabel('stoke2');
subplot(3,3,4);plot(TimeSec:TimeSec:tt*TimeSec, averagepower(:,4));
xlabel('stoke3');
subplot(3,3,5);plot(TimeSec:TimeSec:tt*TimeSec, averagepower(:,5));
xlabel('stoke4');
subplot(3,3,6);plot(TimeSec:TimeSec:tt*TimeSec, SA);xlabel('SA');
subplot(3,3,7);plot(0:deltax:L, n2(:,2));xlabel('n2 along fiber');
subplot(3,3,8);plot(TimeSec:TimeSec:tt*TimeSec, sum(averagepower,2));
xlabel('overall output');hold on;
```

```
subplot(3,3,9);plot(TimeSec:TimeSec:tt*TimeSec, inversion);
xlabel('inversion number V.S. time');
```

Appendix II:
List of publications

Journal publications

1. **<u>L. Pan</u>**, I. Utkin, R. J. Lan, Y. Godwal and R. Fedosejevs, **"High peak power sub-nanosecond passively Q-switched ytterbium doped fiber laser,"** *Opt. Lett.* 35(7) 895-897, 2010.

2. R. J. Lan, **<u>L. Pan</u>**, I. Utkin, Q. Ren, H. J. Zhang, Z. P. Wang, and R. Fedosejevs, **"Passively Q-switched $Yb^{3+}:NaY(WO_4)_2$ laser with GaAs saturable absorber,"** *Opt. Express,* 18, 4000-4005 (2010).

3. **<u>L. Pan</u>**, I. Utkin, and R. Fedosejevs, **"Experiment and numerical modeling of high power passively Q-switched ytterbium doped double-clad fiber lasers,"** *IEEE J. Quantum Electron.* 46, 68-75, 2010.

4. **<u>L. Pan</u>**, I. Utkin, and R. Fedosejevs, **"Two-wavelength ytterbium doped fiber laser with sustained relaxation oscillation,"** *Appl. Opt.* 48, 5484-5489 (2009).

5. **<u>L. Pan</u>**, I. Utkin, and R. Fedosejevs, **"Two-wavelength passively Q-switched ytterbium doped fiber laser,"** *Opt. Express* 16, 11858-11870 (2008).

6. **<u>L. Pan</u>**, I. Utkin, and R. Fedosejevs, **"Passively Q-switched ytterbium doped double-clad fiber laser with a Cr^{4+}:YAG saturable absorber,"** *IEEE Photon. Technol. Lett.* 19, 1979-1981 (2007).

Conference proceedings

1. W. Shi, I. Utkin, J. Ranasinghesagara, **<u>L. Pan</u>**, Y. Godwal, S. Kerr, R. J. Zemp, and R. Fedosejevs, **"High repetition rate passively Q-switched fiber and microchip lasers for optical resolution photoacoustic imaging,"** *SPIE Proc* 7564, pp.75640X-75640X-5 (2010).

Conference presentations

1. **L. Pan**, I. Utkin, R. J. Lan, Y. Godwal and R. Fedosejevs, "375 kW peak power sub-nanosecond passively Q-switched ytterbium doped fiber laser," CMW1,*CLEO 2010,* May 16-21, 2010, San Jose, California, USA

2. **L. Pan**, I. Utkin,Y. Godwal, Z. J. Chen, and R. Fedosejevs "Sub-nanosecond radiation generated from Q-switched Yb doped fiber lasers with stimulated Brillouin scattering," *SPIE Photonics North, 2010,* June 1-3, 2010 Niagara Falls, Ontario, Canada.

3. **L. Pan**, I. Utkin,and R. Fedosejevs, "Comparative study of Q-switched fiber lasers with and without stimulated Brillouin scattering," *CIPI Annual General Meeting, 2010,* June 3-4, 2010 Niagara Falls, Ontario, Canada.

4. **L. Pan**, I. Utkin,and R. Fedosejevs, "Passively Q-switched ytterbium doped fiber lasers with stimulated Brillouin scattering," ID:431,*CAP 2010, Canadian Association of Physics Congress 2010,* June 7-10, 2010, Toronto, Canada.

5. **L. Pan**, I. Utkin, and R. Fedosejevs "High power two-wavelength passively Q-switched Yb doped fiber laser," FLD-2-2-2, *SPIE Photonics North, 2008*, June 2-4, 2008, Montreal, QC, Canada.

6. **L. Pan**, I. Utkin, and R. Fedosejevs "High-repetition-rate passively Q-switched ytterbium doped fiber laser with Cr^{4+}:YAG saturable absorber," JTuA70, *CLEO, 2007,* May 6-11, 2007, Baltimore, MD, USA.

7. W. Shi, I. Utkin, J. Ranasinghesagara, **L. Pan**, Y. Godwal , R. Zemp, R. Fedosejevs, "High repetition rate passively Q-switched fiber and microchip lasers for optical resolution photoacoustic imaging," 7564-32, *BIOS Photonics West,* Jan. 23-28, 2010, San Francisco, California, USA

8. Z. J. Chen, Y. Godwal, **L. Pan**, I. Utkin, Y. Y. Tsui and R. Fedosejevs, "Sensitive detection of heavy metals in water using microchip laser induced breakdown spectroscopy," *CLEO 2010,* May 16-21, 2010, San Jose, California, USA

9. Z. J. Chen, Y. Godwal, I. Utkin, **L. Pan**, and R. Fedosejevs, "Numerical model of diode pumped self Q-switched microchip lasers with both spatial and time dependence," *SPIE Photonics North, 2010,* June 1-3, 2010 Niagara Falls, Ontario, Canada.